Non-adiabatic reaction dynamics studied by chemoelectronic nanodiodes

Dissertation zur Erlangung des akademischen Grades eines
Doktors der Naturwissenschaften
– Dr. rer. nat. –
vorgelegt von Jan Philipp Meyburg
Fakultät für Chemie der Universität Duisburg–Essen

2017

Gutachter:
Professor Dr. Eckart Hasselbrink
Professor Dr. Christian Mayer

Tag der mündlichen Prüfung: 18. April 2018

I hereby certify that this thesis—including all figures—has been composed by me and is based on my own work, unless stated otherwise.

The author thanks Professor Dr. Eckart Hasselbrink for providing the opportunity to prepare this thesis, Dr. Detlef Diesing for assistance and fruitful discussions, and Professor Dr. Christian Mayer for acting as second examiner.

Essen / Chicago / Berlin

Contents

1 Introduction

Chemical and physical phenomena at the interface of two phases are generally studied in the field of surface science. The focus of surface science has always been on understanding surface processes and surface dynamics at the nanoscale. Especially, heterogeneous catalysis has been the traditional realm of surface chemistry. [1] Heterogeneous catalysis refers to a process in which the basic rate of a chemical reaction increases with the presence of a catalyst which is not of the same phase as the reactants or products. The catalyst influences the flow of the reaction but is not consumed or produced during this reaction. Heterogeneous catalysts facilitate the reaction by providing a substrate for the reactants to encounter each other easier. [1, 2, 3]

Research in the field of heterogeneous catalysis was awarded the Nobel prizes—most prominent for Fritz Haber and Carl Bosch in 1918 for their work on the artificial nitrogen fixation by converting atmospheric nitrogen into ammonia by a surface-catalyzed reaction with hydrogen on potassium promoted iron catalysts under high pressures at high temperatures. [1] Friedrich Wilhelm Ostwald was awarded the Nobel Prize already in 1909 for his contribution to catalysis. He observed that a catalyst speeds up a chemical reaction by providing an alternative reaction path with a lower activation energy. Thereby, the catalyst does not change the properties of the equilibrated state as the equilibrium constant is determined by the Gibbs energy of the initial state relative to the final state. [1] In 1912, Paul Sabatier alongside with François Auguste Victor Grignard was honored with the Nobel prize for investigating the improved hydrogenation of organic species in presence of solid magnesium. In addition, Sabatier established his principle on the qualitative concept of interactions between solid catalysts and adsorbed molecules or atoms. [1] In 1932,

Irving Langmuir was awarded for his discoveries and investigations that established the basis for understanding surface reactivity. His research on thin films and surface adsorption that he conducted together with Katharine Burr Blodgett resulted in the concept of the monolayer. Earlier, he also studied filaments in vacuum and different gas environments and the thermionic emission of charged particles from these filaments by passing currents through them. [1] In 2007, Gerhard Ertl was awarded for his research that led to the understanding of dynamics of surface reactions on a truly molecular level. His studies of chemical processes on solid surfaces included the adsorption of hydrogen on crystalline metal surfaces by means of low-energy electron diffraction and further studies on the interaction of carbon monoxide molecules with platinum surfaces. [4, 1] Certainly, other prolific pioneers in the field of surface chemistry contributed to the understanding of heterogeneous catalysis as well. In addition, developments in instrumentation facilitated the progress in surface science. For instance, the development of the scanning tunneling microscope by Gerd Binnig and Heinrich Rohrer in 1982 enabled the deeper understanding of surface dynamics and the character of surface–adsorbate interactions by routinely imaging surfaces and surface bound species with atomic-scale resolution or manipulating even single atoms on surfaces. [5, 6, 1]

Heterogeneous catalysis is of importance not only for science but also for the chemical and energy industries. Globally, the vast majority of chemicals is produced using heterogeneously catalyzed processes—mostly reaction processes on the solid surface of catalysts. Undoubtedly, catalysis and the design and industrial utilization of suitable catalysts are the most successful implementation of nanotechnology. [1] As catalysts do not change the final equilibrium composition of the system but influence the rate at which that equilibrium is approached, catalyzed reactions operate as accelerators for chemical reactions. At best, not all possible reactions are accelerated but selectively the preferred reactions. [1] Even inhibited metastable reactions can be enabled and industrial processes can be implemented much more efficiently. [2] In heterogeneous catalysis, the gaseous or liquid reactants are typically adsorbed on the surface of the solid catalyst and modified to a form in which they readily undergo reactions. This modification often takes the form of a dissocia-

tion of the reactant molecules. The existence of molecular fragments on the surface as a result of chemisorption is one of the reasons for solids to catalyze reactions. [2] Chemisorbed molecules form chemical bonds to suitable surface sites and tend to maximize their coordination number with the substrate. The activity of a catalyst depends on the strength of the chemisorption: a catalyst–adsorbate interaction that is too weak will not facilitate the adsorption, a catalyst–adsorbate interaction that is too strong will prevent the dissociation and reaction of the reactants—a straightforward concept that is known as the Sabatier principle. [1] The catalytic activity of a surface depends also on its structure. As the surface of a solid differs inherently from the bulk due to its free valences, the surface atoms prefer to react with adatoms in order to satisfy their bonding requirements. [1] It can be stated: the more free valences, the more reactive. For instance, a terrace site often has minimal catalytic activity whereas steps and kinks are more active. Furthermore, the electronic structure of the catalyst is crucial for its activity. Some metals directly react with a variety of atoms or molecules, others positively affect surface reactions and are used as catalysts. On the other hand, noble metals hardly react with adsorbates. The electronic band structure of the metals can explain these observations. The interaction of the molecular orbitals of the adsorbates with the s and d bands of the metal affects the binding energies and activation barriers. [1] In the case of a hydrogen atom approaching a metal surface the interaction of the hydrogen and metal orbitals can be considered as a two-step process. First, the hydrogen 1s orbital interacts with the s band of the metal. For transition metals the s band is extended so that the interaction is of the weak chemisorption type and a bonding level far below the Fermi level results. As the bonding level is filled, the overall interaction is of attractive character. For all transition metals the strength of this interaction is similar. Secondly, the interaction of the bonding level with the d band of the metal results in the formation of two levels: one is shifted to lower energies with respect to the original bonding state, the other is shifted to slightly higher energies than the unperturbed metal d band. The low energy state is bonding, the high energy state is anti-bonding. [1] The coupling of the adsorbate s band hybrid with the metal d band and the extent of the filling of the anti-bonding state determines the character of the adsorbate–metal

interaction. Thereby, the position of the anti-bonding state with respect to the Fermi level influences the filling. This explains differences in the chemisorption bond strength among metals as the coupling strength and the Fermi level are distinct for each metal. For early transition metals the anti-bonding state lies above the Fermi level so that it is not filled. As a result the first step and the second step are bonding and the hydrogen atom adsorbs with a release of energy. [1] For coinage metals the anti-bonding state lies below the Fermi level so that it is filled and the attractive first step is canceled out by an repulsive second step. In addition, the magnitude of the coupling in the second step has an influence on the bonding character because the repulsive orthogonalization energy between the adsorbates and the metal d orbitals increases with the coupling strength. If the d orbitals extend spatially also the orthogonalization energy increases. The 5d orbitals of gold are more extended than the 3d orbitals of copper. Accordingly, gold is less reactive than copper as the orthogonalization between the 1s orbital of hydrogen and the 5d orbitals of gold is too costly. [1]

The surfaces of transition metals of the 10^{th} group (nickel, palladium, and platinum) exhibit d bands at the Fermi level. An emerging anti-bonding state lies slightly above the Fermi level and is not filled in the described second step. The resulting adsorbate–metal interaction is therewith moderately attractive and all three metals serve as catalysts in a variety of chemical reactions. Platinum is commonly used as a catalyst and is known for its catalytic properties since 1823, when Johann Wolfgang Döbereiner observed an ignition when a fine dispersion of platinum (also referred to as platinum sponge or platinum black due to its porous, grayish-black appearance) was exposed to a hydrogen–air mixture at room temperature. [2, 3] Nowadays, catalytic platinum is most prominent in catalytic converters that enable the complete oxidation of remaining quantities of hydrocarbons into carbon dioxide and water in the exhaust of combustion engines. In proton exchange membrane fuel cells platinum catalysts allow for the dissociation of hydrogen and oxygen molecules. Finely dispersed platinum serves as catalyst in various hydrogenation reactions and hot platinum is capable of absorbing remarkable amounts of hydrogen. [2]

Various surface dynamics—typically adsorption, dissociation, or recombi-

nation processes—release chemical energy that dissipates and is transferred from the reactants into the degrees of freedom of the surface as well. Besides collective lattice vibrations in the metal substrate also transitions between potential surfaces of different electronic states might result and electron–hole pairs are induced. These processes that lead to changes in the electronic quantum numbers are referred to as non-Born–Oppenheimer chemistry or non-adiabatic chemistry. [7, 8]

2 Theory

2.1 Non-adiabatic chemistry

In 1927, soon after quantum mechanics were established by Werner Heisenberg and Erwin Schrödinger, Max Born and Robert Oppenheimer suggested an approximation that nuclear and electron dynamics within molecules can be considered separately because of the much smaller masses and therefore higher velocities and adaptability of electrons compared to nuclei. [9, 10, 11, 12] Thereby, Born and Oppenheimer described how a molecule can exist in a stable state.

Mathematically, the wave function ψ of a molecule can be broken down into its nuclear component, that includes vibronic and rotational degrees of freedom, and its electronic component:

$$\psi = \psi_{\mathrm{e}} \psi_{\mathrm{N}} \,. \tag{2.1}$$

The stationary states of a molecule can be described by the general time-independent Schrödinger equation:

$$\hat{H}(r, R)\psi(r, R) = E\psi(r, R) \,. \tag{2.2}$$

Here, R stands for the nuclear coordinates, r for the electronic coordinates. Within the non-relativistic scheme, the quantum-mechanical molecular Hamiltonian $\hat{H}$ is generally written as:

$$\hat{H}(r, R) = T_{\mathrm{N}} + \hat{H}_{\mathrm{e}}(r; R) = \frac{1}{2} \sum_k \frac{\hat{P}_k^2}{M_k} + \hat{H}_{\mathrm{e}}(r; R) \,. \tag{2.3}$$

Here, T_{N} represents the operator for the kinetic energy of the nuclei, $\hat{P}_k$ is the

operator of the conjugate momentum of the k^{th} component of R (R_k) with the mass M_k, and $\hat{H}_{\text{e}}(r;R)$ is the many-body electronic Hamiltonian that is defined as:

$$\hat{H}_{\text{e}}(r;R) = T_{\text{e}} + V_{\text{c}}(r;R) = \frac{1}{2m_{\text{e}}} \sum_j \hat{p}_j^2 + V_{\text{c}}(r;R)\,. \tag{2.4}$$

Here, T_{e} represents the operator for the kinetic energy of the electrons, $\hat{p}_j$ is the operator of the conjugate momentum of the j^{th} component of r (r_j), and m_{e} is the electron mass. $V_{\text{c}}(r;R)$ represents the collective Coulomb interactions among electrons and nuclei. [13, 14]

Due to their much larger masses the nuclei in the molecule move much slower than the electrons. As a result the electrons almost instantaneously follow any nuclei transitions—adjusting their positions according to the nuclei configuration. Consequently, the total wave function $\psi(r,R)$ can be written as the product of the molecular wave function $\chi(R)$, that depends only on the positions of the nuclei, and the electronic wave function $\phi(r;R)$ of the rigid molecule. The nuclear positions are therewith arbitrarily static and R_k is regarded as a fixed parameter whereas the electron coordinates r_j are the variables. [13, 14] Thus, the motions of the nuclei and the electrons are independent and no coupling occurs between them:

$$\psi(r,R) = \chi(R)\;\phi(r;R)\,. \tag{2.5}$$

Although this dynamical separation of the electronic and the nuclear motions, the so-called Born–Oppenheimer fixed nuclear approximation (or more casual referred to as the Born–Oppenheimer approximation), is a drastic simplification, it still serves as an important tool of quantum chemistry and was essential for the development and the applications of a variety of theoretical electronic structure and dynamics methods. [13, 14] Molecular dynamics that are fully explained by the Born–Oppenheimer approximation are also referred to as adiabatic processes because the potential energy surfaces of the inspected molecule do not cross and the entire effect of the electronic subsystem is embedded in one potential energy surface. [13] Typically, a potential energy sur-

face describes the energy of a system (for instance a molecule) in dependence of position parameters (usually the bond lengths and the bond angles of the molecule). [15] If there is only one bond length (in a diatomic molecule) the system is described by a two-dimensional potential energy profile. The Morse potential represents such a potential energy profile with only one geometric parameter (the bond length r) plotted as a two-dimensional graph $E(r)$. [15] For a given triatomic molecule (for instance H_2O) there are two bond lengths. As the water molecule is of C_{2v} symmetry (two planes of symmetry and a two-fold symmetry axis) a four-dimensional plot of the system energy E against three geometric parameters (two $O-H$ bond lengths and the $H-O-H$ bond angle) would be required. Usually the $O-H$ bond lengths are represented simultaneously in one axis while another axis represents the $H-O-H$ bond angle in order to describe the system within a three-dimensional plot. [15]

Molecular processes that involve the crossing of potential energy surfaces are called non-adiabatic (or more consequently: diabatic, as ἀδιάβατος already means impassible). Electronically non-adiabatic processes (also referred to as non-Born–Oppenheimer processes) are defined as dynamical events in which the electronic state changes non-radiatively. This may occur as a result of collisions of electrically excited species, electron transfer processes, heterolytic dissociations, or recombination reactions. [13] In addition, electronic excitation energies are usually higher than the energies of nuclear motions, and the valence properties of the ground-state species differ from the valence properties of the electronically excited species. As a result, the dynamical mechanisms of electronically activated systems and thermally activated systems are incommensurable. [13] Also, many chemical processes combine electronic motions such as internal conversions or charge transfers and nuclear motions such as molecular vibrations and rotations so that the Born–Oppenheimer approximation breaks down.

In the case of exothermic surface-catalyzed reactions chemical energy can be released not only into the nuclear and electronic degrees of freedom of the reaction complex but also into the nuclear and electronic degrees of freedom of the catalyst. In consequence of an exothermic reaction, the thermal equilibrium of the catalyst–adsorbate system needs to be re-established. [16] This relaxation

process usually follows paths on the ground state potential energy surface but might also follow paths that include jumps to non-ground state potential energy surfaces. [16, 17]

Adiabatically the release of chemical energy might induce collective lattice excitations in the catalyst. [17] The energies of these quantized lattice vibrations (also referred to as phonons) are typically in the range of 0.01 eV and therewith 2–3 orders of magnitude smaller than chemical energies. [17] As a consequence, a surface-catalyzed exothermic chemical reaction may cause multiple excitations of phonons in the catalyst due to a cascade of subsequent excitation steps or even as a result of a single excitation step. [17]

A number of non-adiabatic effects can be observed as a result of surface-catalyzed exothermic chemical reactions. In 1905, Joseph John Thomson observed the emission of negative charged particles from freshly prepared alkali metal surfaces that were exposed to small amounts of different gases. [18] In the following years, it could be clarified that this particles are electrons and that their emission is a result of surface-catalyzed exothermic chemical reactions. Further and refined studies of this emission of electrons (then referred to as exoelectron emission) became feasible with the development of techniques such as ultra-high vacuum. Surface-catalyzed reactions of electronegative atoms or molecules (for instance oxygen or halogens) on the surfaces of metals with low work functions are likely candidates for the observation of exoelectron emission. [19]

Also photons might be emitted from solid surfaces due to the release of chemical energy. Here, the emitting surface is not in its thermodynamic equilibrium and the photon emission occurs from an electronically excited state. It is therefore referred to as surface chemiluminescence. [16, 19] Due to the fact that this effect is much weaker than the exoelectron emission it was discovered not before suitable surface science techniques were established. [17]

Collective electronic excitations (also referred to as plasmons) might also result from a surface-catalyzed reaction. But as the deposited chemical energy is typically smaller than the plasmon energy that lies usually well above 5 eV this effect should only be considered in the case of certain adsorbate–catalyst combinations: for instance highly exothermic reactions on alkali metals with

small plasmon energies. [17]

A non-adiabatic transfer of the chemical energy that is released in the course of a surface-catalyzed reaction might also cause the excitation of electron–hole pairs in the catalyst. In metals a high density of low-lying excited electronic states exists as a consequence of the zero-gap e–h pair continuum. [17] An excitation of an e–h pair results in the creation of a hot electron with an energy above the Fermi level and a hot hole with an energy below the Fermi level. A direct detection of the excited hot electrons in the catalyst is difficult due to their relaxation time of 10^{-14} s. Scattering events in the metal catalyst—including electron and phonon channels—cause this relaxation. The average distance a hot carrier can diffuse without being inelastically scattered is called mean free path. In platinum the mean free path for hot electrons is typically below 10 nm (4 nm for an electron with an energy of 1.2 eV). [17, 20] Surface-catalyzed reactions but also recombination reaction or adsorption processes—typically chemisorption—on a metal surface may dissipate a part of the released energy into the excitation of an e–h pair. The excited charge carriers travel from the surface through the metal and can be detected if the metal is thin enough with the use of metal–semiconductor *n*-type Schottky diodes or metal–insulator–metal devices that are also referred to as chemoelectronic nanodiodes. [17, 21, 19]

2.2 Chemoelectronic nanodiodes

Atomic or molecular adsorption processes, dissociative chemisorption, abstraction reactions that remove adsorbates from the surface, and especially surface-catalyzed exothermic reactions may cause elementary excitations in the substrate metal. In this case, the dominant dissipation channels are the adiabatic excitation of phonons and the non-adiabatic excitation of e–h pairs. Excited charge carriers might travel through the metal and can be detected as an electric current by means of chemoelectronic nanodiodes like metal–semiconductor–metal systems (MSM) (or metal–semiconductor *n*-type Schottky diodes), metal–insulator–metal systems (MIM), or metal–oxide–semiconductor systems (MOS). [17, 21, 19]

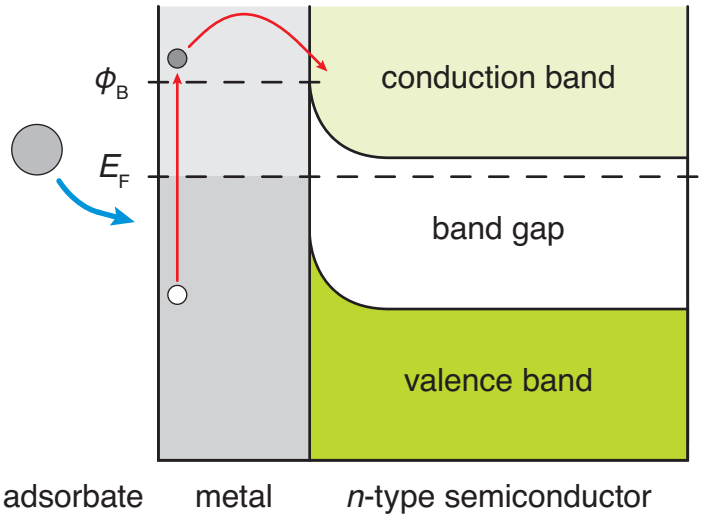

Figure 2.1: Principle of metal–semiconductor–metal detectors: a hot electron from an electron–hole pair induced by surface dynamics ballistically overcomes the Schottky barrier φ_B of the device and reaches the conduction band of the *n*-type semiconductor. The drawn adsorbate interaction (blue arrow) is merely a visualization and should be considered as independent of the energy scaling.

Chemoelectronic nanodiodes are solid state barrier devices that exhibit a catalytically active top metal film that is thinner than the mean free path of the hot carriers that are desired to be detected. This ultra-thin top metal electrode is deposited on top of a related semiconductive substrate in case of MSM devices or on top of an ultra-thin insulator layer (usually a metal oxide), in case of MIM devices. Electron–hole pairs created in the course of a chemical reaction can reach the semi-conductive substrate in MSM systems or tunnel through the oxide layer in MIM or MOS systems or are transferred on conductive pathways through thicker but permeable oxide layers, reach a back metal electrode, and are detected as an electric current (also referred to as chemicurrent I_{chem}). If a bias is applied between the top and the back electrode this transfer can be amplified or restrained. A bias voltage may also serve as a tool to reveal the spectrum of the electronic excitations. [22, 23, 24, 25]

In metals, the electron energy levels are filled up to a certain energy level—the Fermi level E_F. The additional amount of energy that electrons need to leave the metal into the vacuum is referred to as work function W. If chemical

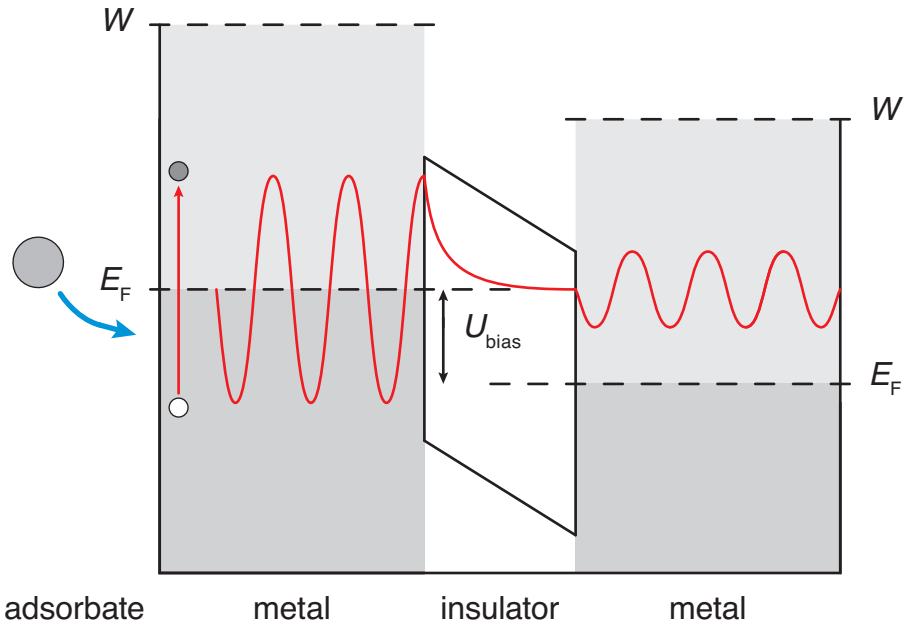

Figure 2.2: Principle of metal–insulator–metal detectors: a hot electron from an electron–hole pair induced by surface dynamics overcomes the potential barrier of the interstitial oxide layer via quantum tunneling—the signal intensity decreases exponentially with the oxide layer thickness but the electron wavelength remains unchanged. The drawn adsorbate interaction (blue arrow) is merely a visualization and should be considered as independent of the energy scaling.

energies are large enough to excite electrons that overcome W the emission of exoelectrons can be observed. The released energy in the course of surface-catalyzed reactions is typically smaller than the work function of late transition metals such as platinum. Hence, excited electrons do not leave the platinum and can not be detected outside of the metal. Electronic excitations in transition metal catalysts caused by surface-catalyzed chemical reactions were not observed until methods for the detection were developed that include composite nanostructures. [17, 26, 21, 19]

After Aviv Amirav and co-workers reported on the excitation of electron–hole pairs at a Ge(100) surface due to scattering processes of ground-state neutral Xe atoms by means of Ge PIN diodes (sandwich structures of *p*-type semiconductor/intrinsic semiconductor/*n*-type semiconductor) in 1986, additional and improved nanostructures were developed in order to study surface dy-

namics. [27] Hermann Nienhaus and co-workers performed experiments on ultra-thin metal films of MSM and MIM chemoelectronic nanodiodes in order to detect hot charge carriers that were induced due to adsorption and recombination of hydrogen and deuterium atoms on Ag and Cu surfaces. [28]

Later, Xiaozhong Ji and co-workers put their focus on surface-catalyzed reactions on thin platinum films. [20] In that research, induced electric currents of up to 40 µA were measured in the course of the steady-state oxidation of carbon monoxide over platinum. MSM platinum *n*-titanium oxide Schottky diodes were used to detect the hot charge carriers. Depending on the conditions of the catalytic oxidation (for instance temperature and partial pressures of the reactants), the thickness of the Pt film, and the properties of the 150 nm thin titanium dioxide current variations were measured. [20]

MSM *n*-type semiconductor Schottky diodes are the most sensitive composite nanostructures suited to detect hot charge carriers caused by non-adiabatic surface dynamics. This is a consequence of the low potential barrier of these nanostructures. The sensitivity of chemoelectronic nanodiodes can be quantified using the quantum yield. This is understood as the number of charge carriers that are detected normalized to the number of molecules of the product that are formed on the surface of the device—or simplified: the generated charge carriers per produced molecule. MSM chemoelectronic nanodiodes enable a quantum yield in the range of 10^{-6}–10^{-2}. Whereas highly exothermic surface reactions such as the chemisorption of oxygen atoms on rough polycrystalline silver generate quantum yields close to the upper limit, the quantum yield for the adsorption of molecular oxygen on the same surface lies close to the lower limit of that range. [21] In the case of the studied CO oxidation on MSM *n*-type semiconductor Schottky diodes even three electrons were collected while four CO_2 molecules were produced. [20]

The downside of this high sensitivity is that also incoming light and fluctuations in temperature might lift electrons over the potential barrier of the device. It is therefore necessary to clarify the source of the induced hot charge carriers. In the case of released chemical energy due to a surface-catalyzed reaction a significant amount of energy is dissipated into the adiabatic excitation of phonons. This heating of the metal film might also result in thermoelectric

effects—especially when temperature gradients across the nanostructure arise. Here, two effects should be considered: the Seebeck effect within the layers of the nanodevice and the thermionic emission (that is discussed in detail within the next section of this chapter) at the interfaces of the device. Both effects might superimpose the hot charge carrier detection.

The Seebeck effect generates a thermopotential U between two points inside a medium that depends on the temperature difference $\Delta T = T_2 - T_1$ between the two points. With the Seebeck coefficient K (also referred to as thermopower or thermoelectric sensitivity) of the medium the thermopotential is:

$$U = \int_{T_1}^{T_2} K \, \mathrm{d}T \,. \; [29,\ 30,\ 31] \tag{2.6}$$

This thermoelectric voltage generates a thermocurrent that additionally contributes to the detected current of excited hot charge carriers. For large temperature differences this contribution easily exceeds the expected quantum yield—especially in the case, that the nanostructure is mounted on a substrate that serves as an effective heat sink (with a huge heat capacity) and parts of the semiconductor layer remain cooler than parts that are heated directly by the dissipated chemical energy released by an exothermic surface-catalyzed reaction. The generation of thermocurrents due to the Seebeck effect is generally expected in semiconductors as the Seebeck coefficients are typically larger in semiconductor materials. Therefore, induced thermoelectric voltages have to be considered using MSM chemoelectronic nanodiodes. The inverted process of the Seebeck effect—that temperature differences are generated by applying a voltage between the two materials—is referred to as the Peltier effect. [30, 31]

In 2012, James Randall Creighton and Michael Elliott Coltrin studied the CO oxidation on platinum again in order to reproduce experiments Xiaozhong Ji and co-workers from Gábor Arpad Somorjai's laboratories at UC Berkeley carried out seven years earlier using Pt–TiO_2 and Pt–GaN MSM Schottky diodes. [32, 20, 33, 34] Besides the fact that similar currents and reaction rates for the CO oxidation over Pt–GaN MSM Schottky diodes were measured the detected currents could be assigned entirely to the generation of thermocur-

rents and no evidence for the generation of chemicurrents was found. In conclusion, the studied Pt–GaN MSM Schottky diodes could simply be described as thermal detectors comparable to thermocouples as these MSM devices are highly sensitive to temperature due to the large Seebeck coefficient of the GaN semiconductor. It could be observed that a lateral temperature difference in the GaN semiconductor with the hot temperature close to the reaction surface and the cool temperature at the other edge of the material was the source of the generated current. [32]

Due to the fact that metal–insulator–metal nanostructures are not composed of semiconductor materials, thermocurrent contributions generated by the Seebeck effect are unlikely and MIM devices are less susceptible to temperature fluctuations. Noble metals exhibit Seebeck coefficients below $10\,\mu V\,K^{-1}$. The Seebeck coefficient of platinum that is used as top electrode in the scope of this work becomes even zero at 200 K and changes sign. In contrast, the Seebeck coefficient of silicon is $\approx 1\,mV\,K^{-1}$ and the Seebeck coefficient of gallium $\approx 300\,\mu V\,K^{-1}$. [35, 36] Furthermore, MIM chemoelectronic nanodiodes are less sensitive to light and temperature fluctuations. The insulating oxide layer between the catalytically active top metal electrode and the metal back electrode is typically 3–5 nm thin and serves as a tunnel barrier for hot charge carriers. Even charge carriers that would not overcome the potential barrier height of the metal–oxide interface (usually in the range of 1–1.5 eV) might reach the back electrode with a certain tunnel probability. [37] Due to the wider band gap in the range of 4–8 eV in metal oxides compared to semiconductors, band-to-band excitations of electron–hole pairs are unlikely. [37] As a consequence of the ultra-thin sandwich layers vertical temperature gradients are less dominant. In addition, the height of the potential barrier can be varied by applying bias voltages between the two metal electrodes. [37, 23] As a result of the applied bias voltage U_{bias} the Fermi levels E_F of the two metals are shifted with respect to each other. The barrier imposed by the band gap in the oxide is therewith distorted and a hot electron transport and a hole-induced electron transport through the barrier are facilitated (see figure 2.3). [36] In the case of a negatively biased platinum top electrode, hot electrons travel easier from the platinum toward the tantalum back electrode whereas hot electrons travel

easier in the opposite direction if the tantalum is biased negatively. However, in the course of this work no hot charge carriers are expected to be generated in the tantalum back electrode. Thus, no hot charge carriers are expected to travel from the tantalum through the oxide barrier toward the platinum. The expected tunnel currents will consist exclusively of hot electrons traveling from the platinum film toward the tantalum film and hole-induced electrons traveling from the tantalum toward the platinum film. The sign of the overall current identifies the predominant fraction. Hot electrons with energies above the Fermi level will dominate these currents as mentioned above. [36]

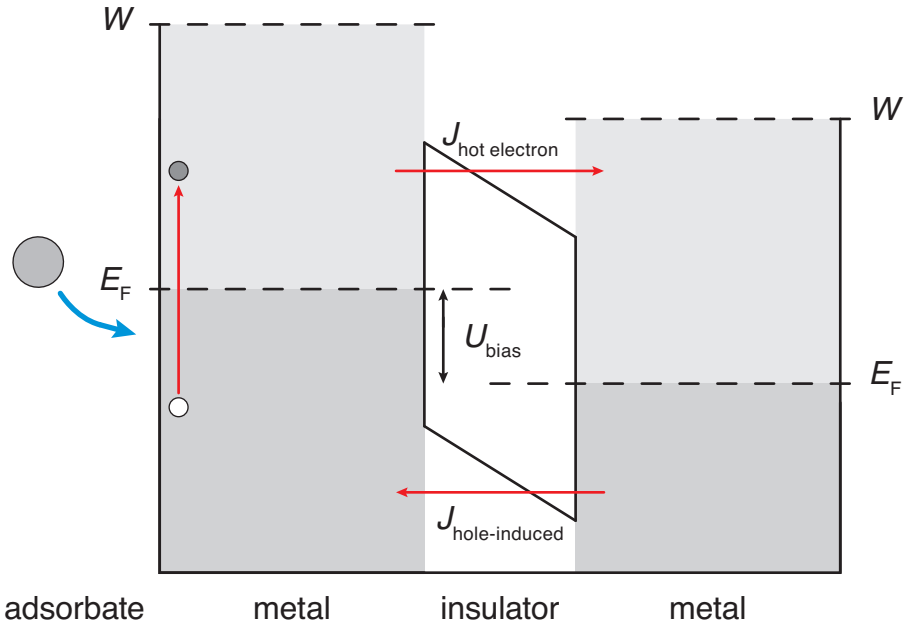

Figure 2.3: Principle of chemicurrent detection using an applied bias voltage U_{bias} in a metal–insulator–metal system in order to shift the Fermi levels E_{F} of the two metals with respect to each other: the transport of electrons (hot or hole-induced electron transport) through the barrier is facilitated. The drawn adsorbate interaction (blue arrow) is merely a visualization and should be considered as independent of the energy scaling.

Due to the susceptibility to thermoelectric effects of MSM chemoelectronic nanodiodes the use of MIM devices is preferred as the wider band gap of the interstitial metal oxide layer effectively suppresses thermoelectric currents even at higher temperatures. Nonetheless, thermionic emission contributes to

the measured device currents also in MIM nanostructures.

2.3 Thermionic emission

Although Edmond Becquerel described the phenomenon of thermionic emission already in 1853, it was rediscovered and further examined by Thomas Alva Edison in the context of his research on incandescent light bulbs and electrical illumination in 1880. [38] Edison observed consistently formed dark residues on the inside surfaces of the glass bulbs that exhibited comparable negative shadows in the plane of the carbon filaments. In vain search for the cause of this lighter areas within the dark residues over a period of three years, Edison finally decided to mount an additional electrode (made of metal plates, wires or foils) adjacent to the filament inside the bulbs. He connected a galvanometer in order to measure the flow of charge between the filament and the additional electrode and applied bias voltages between them. [38] By biasing the electrode positively with respect to the filament a current was measured. This current was not measured in the case that the electrode was set to a negative potential relative to the filament. Edison recognized the reference of his discovery to Becquerel's work and concluded his research by finalizing a patent on thermionic diodes (also referred to as thermionic-valve or vacuum tube). However, the source of the observed current was still unidentified until the existence of electrons was discovered by Joseph John Thomson in 1897 and Owen Willans Richardson initiated his research on thermionic emission. [38] Richardson concluded from his experimental results that the current increases exponentially with the temperature T of the filament and assumed that the thermionic current density J can be expressed as:

$$J = A_{\mathrm{G}} T^2 \, \mathrm{e}^{-\frac{W}{k_{\mathrm{B}} T}} \, . \, [39,\ 31] \tag{2.7}$$

Here, A_{G} is a constant that combines a material-specific correction factor and a universal constant, W is the work function of the filament metal, and k_{B} is the Boltzmann constant. The work function is material specific and typically in the range of 1.9–6 eV for metals and all metals will melt well before the value of

$k_B T$ is comparable to the value of W. Thus, the exponential term of equation 2.7 is a limiting factor for the emission current in any case. A decrease of the work function would result in a current increase. Adsorbed species influence the work function of a material. For instance, a work function decrease of a metal can be achieved by oxidizing the surface of that metal. Also electric fields influence the work function. If the emitter surface is biased negatively relative to its surroundings the work function is reduced by an amount of ΔW that depends on the magnitude F of the employed electric field at the emitter surface:

$$\Delta W = \sqrt{\frac{q^3 F}{4\pi\epsilon_0}} \,. \; [39,\ 31] \tag{2.8}$$

Here, q is the elementary charge and ϵ_0 is the vacuum permittivity. Therewith, equation 2.7 that is also referred to as Richardson–Dushman equation can be corrected to:

$$J = A_G T^2 \, \mathrm{e}^{-\frac{W-\Delta W}{k_B T}} \,. \tag{2.9}$$

For electric field strengths up to $1 \times 10^8 \,\mathrm{V\,m^{-1}}$, this relation of the field enhanced thermionic emission (also referred to as Schottky emission) describes quite accurately the current density emitted by a surface. For higher electric field strengths quantum tunneling of electrons (also referred to as Fowler–Nordheim tunneling or as field electron emission) has to be taken into account. [39, 31]

Up to this point, it should be noted that the emission of electrons from a metal depends on the metal's work function, on the metal's temperature, and on employed electric fields at the metal's surface. In case of thin metal films and thermionic currents within thin film devices the term work function should be corrected to interfacial barrier as electrons do not leave the metal into the vacuum here but reach the back contact on alternate paths. As the barriers for these paths are significantly lower than the work function detectable thermionic currents in thin film devices can be expected at much lower temperatures and even at lower electric field strengths.

In the ideal case of two large plane parallel capacitor plates that are charged and separated by a distance d the absolute value of the field strength is:

$$E = \frac{U}{d}\,. \tag{2.10}$$

This idealization seems adequate for MIM chemoelectronic nanodiodes, because the two capacitor plates areas are huge ($\approx 12\,\mathrm{mm}^2$) compared to their separation ($\approx 4\,\mathrm{nm}$). An applied voltage of 0.2 V between the two metal films would result in an ideal electric field strength of $5 \times 10^7\,\mathrm{V\,m^{-1}}$.

In metal–insulator-metal devices the interfacial barrier is high compared to the barriers of the most sensitive MSM n-type semiconductor Schottky diodes. Thus, hot electrons unlikely overcome the barrier but reach the backside electrode via tunneling through the ultra-thin oxide layer. Typically, there are two distinguishable interfacial barriers from both metal electrodes toward the insulating oxide layer. In the case of $\mathrm{Ta-Ta_2O_5}$ the interfacial barrier has a height of $\varphi_{\mathrm{Ta-Ta_2O_5}} = 1\,\mathrm{eV}$. The interfacial barrier at the $\mathrm{Pt-Ta_2O_5}$ interface has a height of $\varphi_{\mathrm{Pt-Ta_2O_5}} = 1.7\,\mathrm{eV}$. The difference in the barrier height causes an internal potential drop φ_{int} of $0.7\,\mathrm{eV}$ in the oxide layer. [35] Therewith, an electric field is established between the two metal layers even in the case that no bias voltage is applied. Considering equation 2.10, the electric field strength that an electron is exposed to in the MIM device would reach $1.75 \times 10^8\,\mathrm{V\,m^{-1}}$. Presuming a dielectric constant of $\epsilon = \infty$ in the case of neglected image charge effects at the interfaces the potential energy diagram exhibits a trapezoidal barrier shape (see figure 2.4). The corners of this shape are rounded if the used dielectric constant is corrected in order to consider image charge effects. [40, 41]

The shape of the potential barrier has a significant influence on the tunnel currents that are expected to be detected by means of a $\mathrm{Pt-Ta_2O_5-Ta}$ MIM chemoelectronic nanodiode. Despite the fact that a tunnel current decreases exponentially with the barrier distance to overcome as known from the Gamow–Sommerfeld factor, the barrier potential V itself is a function of the position z inside the oxide layer along the thickness d with $z = \{0, \ldots, d\}$. Also an additionally applied voltage U affects the potential. Obviously, the paths through the oxide layer are different for electrons tunneling from the Pt side

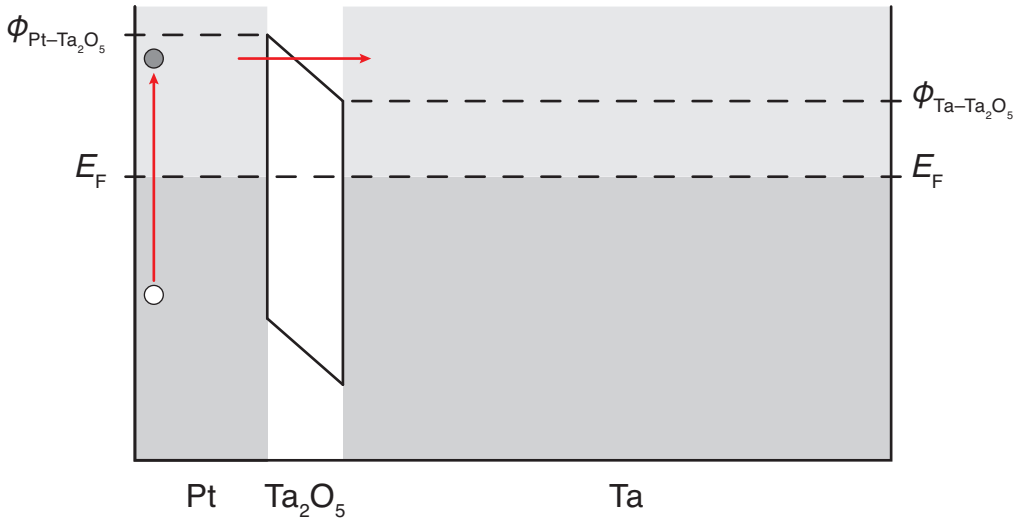

Figure 2.4: MIM $Pt-Ta_2O_5-Ta$ chemoelectronic nanodiode with distorted potential barrier caused by a difference in the barrier heights $\varphi_{Ta-Ta_2O_5}$ and $\varphi_{Pt-Ta_2O_5}$ of the two metals that is present even without an applied bias voltage

compared to electrons tunneling from the Ta side through the interstitial oxide layer. As the oxide was grown from the tantalum side it seems reasonable to start with $z = 0$ at the $Ta-Ta_2O_5$ interface. For a tantalum electron at the Fermi level the barrier potential is therewith:

$$V(z, U) = E_F + \varphi_{Ta-Ta_2O_5} + \frac{z}{d}(U + \varphi_{int})\,. \text{ [24]} \tag{2.11}$$

Furthermore, the barrier potential depends on the incident energy E of the tunneling electron that in turn depends on the angle θ normal to the device interface of the electron wave vector (also referred to as k-vector). Therewith, the barrier potential is expanded to:

$$V(z, \theta, E, U) = \frac{E}{2}(1 + \cos(2\theta)) - V(z, U)\,. \text{ [24]} \tag{2.12}$$

According to the Wentzel–Kramers–Brillouin approximation the transmission probability T through the potential barrier can be expressed by:

$$T(\theta, E, U) = \exp\big(-2\int_0^d \sqrt{\frac{2m_\mathrm{e}}{\hbar^2}V(z,\theta,E,U)}\,\mathrm{d}z\big)\,.\,[24] \tag{2.13}$$

Also the densities of states of the metal electrodes influence the tunneling processes as for certain energy levels more electron states are available to participate. A spectrum of the electrons attempting the tunnel process can be derived using the product of the free electron gas density and the Fermi function. Thus, the occupation probabilities for the electronic states in the two electrodes can be expressed with:

$$p_1(E+U) = \Big[\exp\big(\frac{E - E_{\mathrm{F}_1} + U}{k_\mathrm{B}T}\big) + 1\Big]^{-1}\,.\,[24] \tag{2.14}$$

And:

$$p_2(E) = \Big[\exp\big(\frac{E - E_{\mathrm{F}_2}}{k_\mathrm{B}T}\big) + 1\Big]^{-1}\,.\,[24] \tag{2.15}$$

Therewith, a tunnel current density $\mathrm{d}J(T,E,U)$ is derived as:

$$\mathrm{d}J(T,E,U) = \frac{2\pi m_\mathrm{e}}{h^3}\int_{-\frac{\pi}{2}}^{0}\Big[p_1(E+U) - p_2(E)\Big]\,T(\theta,E,U)\,\mathrm{d}\theta\,.\,[24] \tag{2.16}$$

It should be noted, that this is a partial current density. An integration over the energy includes density of state effects. Now, the total current density can be expressed as:

$$J(T,U) = \int_0^\infty \mathrm{d}J(E,U,T)\,\mathrm{d}E\,.\,[24] \tag{2.17}$$

As the Fermi function determines the probability that an energy state is occupied by an electron if the electrons material is under equilibrium conditions this approach is again an approximation—and as already discussed: equilibrium conditions are not necessarily met in the case of hot electron tunneling. However, during slowly performed heating and cooling processes it can be

assumed that there is always enough time to establish an equilibrium state in the electronic system—and measured currents can be considered as a function of the applied voltage between the two metal electrodes of the device and its temperature if hot electron tunneling can be excluded.

2.4 Surface dynamics on Pt

Surface-catalyzed reactions and heterogeneous catalysis on solid surfaces follow characteristic mechanisms. In general, the adsorption of one or several reactants is a prerequisite. A distinction between two kinds of adsorption is made: physisorption and chemisorption. Although there is a more-or-less continuous spectrum of interaction strengths from one to the other, these two categories serve as useful distinction in most cases. [1]

Physisorption is a physical interaction in which the adsorbate is bound to the surface due to polarization in the form of permanent dipole–dipole interactions (also referred to as Keesom forces), permanent and corresponding induced dipole–dipole interactions (also referred to as Debye forces), or between instantaneously induced dipole–dipole interactions (also referred to as London dispersion forces). Despite their long range these van der Waals forces are weak with adsorption enthalpies of below 0.3 eV. Thus, no chemical bonds can be cleaved during physisorption and adsorbed molecules remain undissociated on the surface. As physisorbed species are not fixed to certain adsorption sites due to the rather weak interaction with the surface the adsorbate diffuse almost barrier-free over the surface even at low temperatures. Often, the interactions between the physisorbed species are stronger than the interactions with the surface. [1, 42]

Chemisorption in turn is highly directional and chemisorbed species stick to specific sites on the surface accordingly. The adsorbate–surface interactions are highly influenced by the exact position and orientation of the adsorbate with respect to the substrate. Adsorption sites of the highest coordination are preferably occupied by chemisorbed atoms. On the Pt(111) surface atomic oxygen tends to sit on the face-centered cubic (fcc) three-fold hollow sites, forming a bond strength of ≈ 3.7 eV. Hydrogen atoms tend to bind on high-

coordination sites as well. [1, 42, 43] In order to optimize the adsorption site adsorbed species diffuse on the substrate. A diffusing adsorbate hops from one site to the next by overcoming potential barriers. On the Pt(111) surface, a single adsorbate diffuses via hexagonal close-packed (hcp) sites as intermediate states toward the adjacent fcc sites. Diffusion pathways to unoccupied sites differ depending on the nearest neighbor constellations as well. If one of the hcp intermediate states is blocked but the final fcc site is unoccupied the adsorbate can still diffuse via an on-top site toward the final position. In case of diffusion via on-top sites the potential barrier is higher, because such a diffusion process is energetically unfavorable. [42, 43] In case of a uniform potential, the diffusion rate can be expressed by an Arrhenius equation:

$$D = D_0 \, \mathrm{e}^{-\frac{E_\mathrm{a}}{k_\mathrm{B}T}} \, . \tag{2.18}$$

Here, D_0 is the diffusion coefficient at infinite temperature and E_a represents the activation barrier for diffusion. For very low temperatures diffusion processes become unlikely as the adsorbate motions are somewhat frozen. However, light adsorbates like atomic hydrogen or deuterium might still diffuse on quantum tunneling paths. [1] For high temperatures and $k_\mathrm{B}T \gg E_\mathrm{a}$ adsorbates move freely across the surface as they are still bound in the z direction to the surface but not in x and y directions anymore. This state is also referred to as two-dimensional gas. [44]

For moderate temperatures the diffusivity of an adsorbate can be described using the mean squared displacement $\langle \Delta x^2 \rangle$ along two coordinates on a two-dimensional surface ($d = 2$):

$$\langle \Delta x^2 \rangle = 2dD\Delta t \, . \, [44] \tag{2.19}$$

Thereby, the diffusivity D is related to a hopping frequency ν and the distance between two sites λ:

$$D = \frac{1}{4}\lambda^2 \nu \tag{2.20}$$

and respectively

$$D_0 = \frac{1}{4}\lambda^2 \nu_0 \,. \text{ [44]} \tag{2.21}$$

Thus, it can be expressed:

$$\nu = \nu_0 \, \mathrm{e}^{-\frac{E_\mathrm{a}}{k_\mathrm{B} T}} \,. \tag{2.22}$$

Here, the hopping frequency ν_0 can be interpreted as the number of diffusion attempts per unit of time—or more figurative: how often the adsorbate tries to hop from the initial site to the adjacent site per second. A microscopic understanding of this factor is often motivated by comparing this attempt frequency with a vibration frequency at the surface or a frustrated translational mode. [44, 42] However, the diffusion barrier is not uniform but is influenced by the surface conditions and adsorbate–adsorbate interactions. Therefore, adsorbates agglomerate and form islands of typical shapes as a result of diffusion processes. [1, 42, 43] The described Arrhenius approach is suitable to analyze and even simulate diffusion processes, epitaxial growth, agglomeration, and Ostwald ripening on defined crystalline surfaces. [44, 45]

Molecular hydrogen dissociates on a platinum surface as a result of adsorption. Each molecular orbital of the approaching hydrogen molecule interacts with the electronic states of the platinum surface and electrons are transferred. Bonding and anti-bonding orbitals are generated by each combination of hydrogen molecular and platinum surface orbitals. Depending on the distance and the quality of the interaction between the hydrogen molecule and the platinum surface the position and the width of these generated hybrid orbitals change. The σ and the σ^* molecular orbitals of hydrogen change their position and shape while the molecule is approaching the platinum surface. Thereby, the σ^* orbital drops in energy and broadens. Platinum electrons are transferred into and populate the σ^* orbital, as soon as it drops below the Fermi level of platinum. As a result, the H−H bond is extended and weakened while simultaneously the H−Pt bond is formed. If enough electron density is transferred the hydrogen molecule dissociates and two hydrogen atoms stick at the platinum surface. [1, 46] The dissociation of H_2 on platinum surfaces depends on geometric components as well. The orientation of the molecule with respect

to the surface is of importance for the dissociation, because molecular orbitals need to overlap for an effective charge transfer. Furthermore, the nature of the surface affects the dissociation as well as some surface sites are more favorable for dissociation than others. [1]

At temperatures below 150 K, oxygen chemisorbs on Pt(111) surfaces molecularly on bridge sites and on-top of Pt substrate atoms with a saturation coverage of $\theta = 0.44$ ML. A monolayer represents 1.49×10^{15} O_2 molecules/cm^2 here. The on-top site O_2 molecules exhibit an O–O bond that is parallel to the surface. Whereas the on-top site O_2 is comparable to superoxide species ($O_2{}^-$) with a bond order of ≈ 1.5 and a bond length of 1.28 Å, the bridge site O_2 is described as a peroxide species ($O_2{}^{2-}$) with a bond order of ≈ 1 and a bond length of 1.49 Å. [47, 48, 2] At temperatures of ≈ 150 K oxygen dissociates accompanied by the desorption of molecular oxygen. The remaining atomic oxygen diffuses to fcc three-fold hollow sites and does not desorb until the surface is heated up to ≈ 600 K. [47] In the temperature range of 170–700 K oxygen adsorbs dissociatively with a sticking probability of 0.06 at 300 K but a decreased sticking probability of 0.025 at 600 K. [49] Two possible adsorption processes were observed experimentally: a concerted dissociation and adsorption process resulting in two oxygen atoms on the Pt surface, and an indirect process involving the adsorption of molecular oxygen that has to overcome an activation barrier for dissociation. [50, 49] No direct dissociation events of O_2 on Pt(111) were observed by using ab initio molecular dynamics simulations. [51] Due to the shape of the potential energy surface, adsorbing oxygen molecules do not directly propagate along the dissociation channel. First the oxygen molecules become trapped in an adsorption well and accommodate on the Pt(111) surface by moving laterally on the surface. Dissociation is initiated subsequently by thermal fluctuations. [51] Comparable to the H_2 dissociation on Pt surfaces, electron density from the platinum is transferred into the antibonding molecular orbital of O_2—in this case the π^* molecular orbital. This electron transfer from the substrate into the adsorbate causes a positive change of the Pt work function. [50]

On clean platinum surfaces, water chemisorbs molecularly and forms ice overlayers at temperatures ≤ 100 K. Up to its desorption temperature of 160 K

water does not dissociate here. [52, 53] Below 160 K the mobility of the chemisorbed water molecules is high enough to allow for surface diffusion and island growth with intermolecular hydrogen bonding at submonolayer coverages. The water molecules form clusters on the Pt surface that exhibit oxygen lone-pair bonding and hydrogen bonding to the Pt surface. Once a monolayer is established, the oxygen lone-pair bondings disappear in expense of hydrogen bondings. [54] In multilayer coverages the water molecules form more and more bulk crystalline ice I_h or ice I_c (the two natural forms of ice) but still exhibit free OH groups that are caused by the misfit of the Pt lattice and the ice structure. [54, 53]

In presence of atomic oxygen coverages ≤ 0.25 ML adsorbed water can be partially dissociated on the Pt(111) surface through the reverse disproportionation reaction at $T = 150$ K:

$$H_2O_{(a)} + O_{(a)} \longrightarrow 2\,OH_{(a)}\,. \text{ [55]} \tag{2.23}$$

Formed OH species adsorbed on platinum surfaces are considered as important reaction intermediates in hydrogen formation, water formation and fuel cell electrocatalysis. At higher coverages these species tend to occupy on-top sites and are stabilized by surrounding water. If not enough water is present 2 OH decompose back to water and atomic oxygen that stay adsorbed on the surface. [56, 57] Established OH + H_2O mixtures stay adsorbed on the Pt surface and form a hydrogen-bonded network comparable to pure chemisorbed water. These mixtures seem to stick more stable on the Pt surface as the hydrogen bonding between OH and H_2O is stronger than in the pure water network. [55] The most stable ratio of H_2O to OH molecules within the formed network on platinum turned out to be $2:1$. [55] At coverages of $\theta \leq 0.1$ ML the pre-adsorbed atomic oxygen is completely consumed by the disproportionation reaction. At coverages in the range of 0.1–0.25 ML parts of atomic oxygen remain unreacted on the Pt surface. [55] If all adsorbed OH species are incorporated into the hydrogen bonding, all hydrogen groups participate in the hydrogen bonding network. The OH groups always bind to the Pt surface with the oxygen atom down. All hydrogen bonds are orientated parallel to the

surface. One third of the shared protons are delocalized between two oxygen atoms. [58] As H_2O is needed to stabilize the formed OH species, the hydrogenation is reversed if the water molecules are removed from the surface. [58] The partial dissociation of water molecules is more facile than the complete dissociation of water on surfaces that can be carried out photochemically using electromagnetic radiation—for instance $h\nu = 6.4\,\mathrm{eV}$ on Pd(111). [59, 60, 55]

Atomic oxygen chemisorbed on Pt(111) surfaces might also be hydrogenated with the addition of atomic hydrogen:

$$\mathrm{H_{(a)} + O_{(a)} \longrightarrow OH_{(a)}}\,. \text{ [61]} \tag{2.24}$$

Whereas reaction 2.23 is restricted to temperatures above 130 K, reaction 2.24 might already occur at much lower temperatures even in presence of adsorbed water. Furthermore, the hydrogenation of atomic oxygen on the Pt(111) surface can be initiated at low temperatures according to reaction 2.24 and proceeds at temperatures around the desorption temperature of water according to reaction 2.23 where all water molecules that are not hydrogen-bonded to OH will desorb. Therewith, the addition of each hydrogen atom at lower temperatures causes a vacancy in the hydrogen bonding network on the Pt surface that is formed by the hydrogenation at the higher temperature. It can be stated: the number of low temperature H addition steps limits the amount of formed OH at elevated temperatures. [61]

On reconstructed Pt(110)-(1×2) surfaces water molecules adsorb intact and OH species remain adsorbed even at temperatures around 205 K when water is already desorbed as they are not incorporated into the hydrogen bonding network. [58] Scanning tunneling microscopy studies revealed that water molecules adsorb preferentially on the upper side of steps on Pt(111) surfaces and are stable as quasi-one-dimensional chains up to 160 K. In contrast, two-dimensional water islands on terrace sites desorb already at 145 K. [62]

Molecular hydrogen dissociates at temperatures above 10 K on platinum surfaces. As hydrogen has the ability to lose or accept an electron and is stable as a proton or as well as a negative ion with the stable configuration of He. Both states can be present on the surface and also in the bulk of vari-

ous metals. [63] The hydrogen incorporation into the surface material might change the electric charge distribution on the surface and therewith, influence the work function of the metal. The electric charge distribution on the surface depends on the surface topography as well. For instance, adsorption events or chemical reactions that modify the surface structure can affect the electron density at the surface. In the case of thin metal films, such sources of stress might also influence the metal's adhesion to the support. Defects or cracks in the previously flat surface might result in changes of the electric charge distribution or the polarization of the system. [63]

The course of reactions at surfaces depends on various characteristics. For instance the transport of reactants toward, on, and away from the surface. [1] Three surface-catalyzed reaction mechanisms can be distinguished:

the Langmuir–Hinshelwood mechanism,

the Eley–Rideal mechanism,

and the precursor mechanism.

Any surface reaction can be described by one of these mechanisms or as a combination of these mechanisms and all of the mechanisms can occur in reverse. [1]

The Langmuir–Hinshelwood mechanism is the most common surface reaction mechanism. Here, both reactants A and B are adsorbed on the surface where they diffuse toward each other, collide, and form the product AB that desorbs afterward. Therefore, adsorption, surface diffusion, and desorption are essentially in Langmuir–Hinshelwood surface reactions. Kinetically, it is challenging to determine the rate law of the overall reaction mechanism as it can not be properly interpreted if the complete reaction mechanism is unclear and not all reaction steps are known. Usually one reaction step is the bottleneck and determines the overall rate—also referred to as the rate determining step. [1] In case of the oxidation of CO and H_2 on platinum to CO_2 and H_2O respectively, chemical energy is dissipated from the reactants to the surface and into the desorbing products as both Langmuir–Hinshelwood surface reactions are highly exothermic. Whereas formed H_2O desorbs with an

energy that is comparable to the surface temperature, CO_2 leaves the surface containing high levels of rotational, vibrational, and translational energy. As H_2O is formed on the surface it accommodates on the surface before it desorbs thermally. Therefore, it can be assumed that the formed H_2O is similar in structure to that of adsorbed water. In contrast, a substantial fraction of the released chemical energy of the CO oxidation reaction is carried away in case of desorbing CO_2. Within the reaction, CO diffuses toward an adsorbed oxygen atom in order to form CO_2 in a bent configuration. Physisorbed CO_2 is much weaker bound to the Pt surface if it has a linear configuration. The bent CO_2 formed in the oxidation reaction is unable to accommodate into this linear configuration and desorbs instead without equilibration. [1] Therewith, it can be argued that the formation, the molecular orientation, and the desorption dynamics of the product determine the energy dissipation pathways in case of surface-catalyzed reactions.

The Eley–Rideal mechanism involves only one adsorbed reactant A on the surface. The other reactant B collides and directly reacts with the already adsorbed reactant A out of the surrounding gas or liquid phase to form the product AB—or B adsorbs close to B on the surface and diffuses with excess energy toward A to react. In any case, only A is already in chemical equilibrium with the surface and the reaction rate depends on the impinging rate of B and the surface coverage with A. Subsequently, the formed product desorbs from the surface. [64] The coverage of the adsorbed reactant A on the surface and the partial pressure of reactant B determine the reaction rate here. In contrast to the Langmuir–Hinshelwood mechanism, the formed products within the Eley–Rideal scheme are highly energetic and exhibit a memory of the initial conditions of the incident reactant B that is not accommodated with the surface. Therefore, smaller amounts of chemical energy are dissipating into the substrate. [1] As the probability for the precise collision between A and B is rather small, surface-catalyzed reactions rarely follow the Eley–Rideal reaction mechanism.

The precursor mechanism involves also only one adsorbed reactant A on the surface. The other reactant B collides with the surface, forming a mobile precursor state (also referred to as hot atom or hot molecule) that is not

fully accommodated to the surface. This hot reactant B and the adsorbed reactant A diffuse and collide with each other and form the product AB that desorbs afterward. The dynamics of this mechanism are kinetically complex and highly sensitive to interaction potentials. Hot oxygen atoms might participate in the CO oxidation over Pt(111) surfaces. In case of co-adsorbed O_2 and CO on the Pt(111) surface at 100 K, the molecular oxygen dissociates when heating the system up to 150 K and some of the liberated O atoms react as hot precursors with CO before they accommodate with the surface. [1] Hot hydrogen atoms incident on Pt surfaces that exhibit pre-adsorbed atomic hydrogen and participate in the barrierless and highly exothermic formation of H_2. Hot hydrogen atoms inefficiently dissipate energy to the substrate. Consequently, inelastic scattering with adsorbed hydrogen atoms is much more efficient in order to accommodate with the surface. Alternatively, the hot hydrogen atom can react with an already accommodated hydrogen atom to form H_2 and desorb from the surface carrying away the excess energy. Also, displacement reactions might occur among accommodated hydrogen atoms to form H_2 that equilibrates with the surface as a result of the impact of hot hydrogen atoms. Anyhow, hydrogen atoms are particularly well suited to participate in hot atom reactions due to their reactivity and their long lifetime in the hot precursor state as a result of the inefficient energy exchange with the surface. [1]

Desorption of reactants or formed products might occur thermally or photochemically induced. Thermal desorption is a thermally activated process that can be described by an Arrhenius behavior of the desorption rate. The thermal programmed desorption procedure (TPD) is based on this behavior and has become the most widespread tool in order to study adsorbate–surface interaction. [65, 66, 67, 68] The reliable TPD technique allows to gain insight in both, the thermodynamic and the kinetic parameters of desorption processes or decomposition reactions on surfaces. In addition, the method may reveal information on the composition of an adlayer. For this purpose, typically a clean and defined crystal surface is cooled under ultra-high vacuum conditions below the adsorption temperature of a chosen gas by means of a suitable liquid coolant or cryogenic pumps. Exposures with the chosen gas up to a predetermined pressure p for a measured period of time Δt result in a certain

coverage of the adsorbed gas on the cold sample surface. An adsorption rate r_{ads} depends on the mass flux of approaching molecules or atoms j, an initial sticking coefficient s_0, and the relative coverage θ of the surface:

$$r_{\mathrm{ads}} = \frac{\mathrm{d}\theta}{\mathrm{d}t} = j s_0 (1 - \theta)\,. \; [23] \tag{2.25}$$

Depending on the dosage $D = p\Delta t$ (with the pressure of the dosing gas or vapor p and the duration of exposure Δt) submonolayer, monolayer or multilayer adsorb on the surface. Dosages are usually given in units of Langmuir (L). For a sticking coefficient of $s = 1$, $D = 1.33 \times 10^{-6}\,\mathrm{mbar\,s}$ correspond to 1 L. In other words: a dosage of 1 L corresponds to the formation of an adsorbate monolayer if the sticking coefficient is $s = 1$. Subsequent to the exposure, the inflow is terminated and the non-adsorbed gas is pumped out of the chamber. Then, the sample is turned toward a quadrupole mass analyzer. The use of a quadrupole mass analyzer enables a mass-selective measurement of the pressure change due to desorption processes. Therefore, a distinction between different desorption species is possible if they differ in mass. As soon as the initial pressure has been reached again, a temperature ramp—usually linear in time—is applied to the sample according to:

$$T = T_0 + \beta t\,. \; [67,\ 1,\ 69] \tag{2.26}$$

Here, T is the actual sample temperature, T_0 is the initial temperature, and β is the heating rate in $\mathrm{K\,s^{-1}}$. For temperatures below the desorption temperatures of the adsorbed species, a base pressure p_{b} results due to pump limitations and possible leaks in the apparatus. The pump limitation results from the increasing improbability of a particle transport with decreasing pressure. Recording the actual pressure p, a change of pressure Δp can be derived by:

$$\Delta p = p - p_{\mathrm{b}}\,. \; [1,\ 69] \tag{2.27}$$

As a change in pressure is attributed to desorption processes if the pump rate is large enough, Δp is directly proportional to the rate of desorption r_{des}. This desorption rate—the rate of coverage change as a function of time—is

described by the Polanyi–Wigner equation:

$$r_{\mathrm{des}} = -\frac{\mathrm{d}\theta}{\mathrm{d}t} = \nu(\theta, T)\theta^n \exp\big(-\frac{E_{\mathrm{des}}(\theta, T)}{k_{\mathrm{B}}T}\big)\ .\ [1,\ 69] \tag{2.28}$$

Here, ν is the pre-exponential factor of the chemical process of order n. This oscillation frequency factor can be understood as the number of desorption attempts per second of an adsorbed molecule on the surface. E_{des} is the desorption activation energy, k_{B} is the Boltzmann constant, T the surface temperature, and θ the relative coverage of the surface. At low temperatures the desorption activation energy is not reached by the thermal energy input $k_{\mathrm{B}}T$ and desorption is negligible. For high temperatures the amount of desorption events increases exponentially. Simultaneously, the coverage decreases and for a certain high temperature all molecules are desorbed—and a peak profile results. After insertion of the linear temperature ramp into equation 2.28 and assuming that the pre-exponential factor and the desorption activation energy are independent of coverage, a maximum of the desorption rate exists at a certain peak temperature T_{peak}:

$$\frac{\mathrm{d}r_{\mathrm{des}}}{\mathrm{d}t} = 0 \Rightarrow \frac{E_{\mathrm{des}}}{k_{\mathrm{B}}T_{\mathrm{peak}}^2} = \frac{n\nu}{\beta}\ \theta_{\mathrm{peak}}^{n-1} \exp\big(-\frac{E_{\mathrm{des}}}{k_{\mathrm{B}}T_{\mathrm{peak}}}\big)\ .\ [1,\ 69] \tag{2.29}$$

A variation of the desorption activation energy E_{des}, of the heating rate β, the pre-exponential factor ν, or the coverage θ affect the peak temperature. A variation of ν, β and the desorption order n affect the peak shape. The rate at the peak—and consequently the amount of desorbing molecules—is affected by the initial coverage θ. [1, 69]

For zero-order desorption kinetics ($n = 0$) the Polanyi–Wigner equation (2.28) turns into:

$$r_{\mathrm{des}} = \nu \exp\big(-\frac{E_{\mathrm{des}}}{k_{\mathrm{B}}T}\big)\ .\ [1] \tag{2.30}$$

This implies that in the case of zero-order desorption, the rate does not depend on the coverage and increases exponentially with temperature. For different initial coverages, desorption curves result that exhibit identical leading edges and drop instantly when all molecules are desorbed. For higher initial cover-

ages the curve drops at higher temperatures. Zero-order desorption processes are typically observed for multilayer coverages. Also strong attractive interactions between adsorbates (desorption from islands) may cause a pseudo-zero-order desorption. [1, 69]

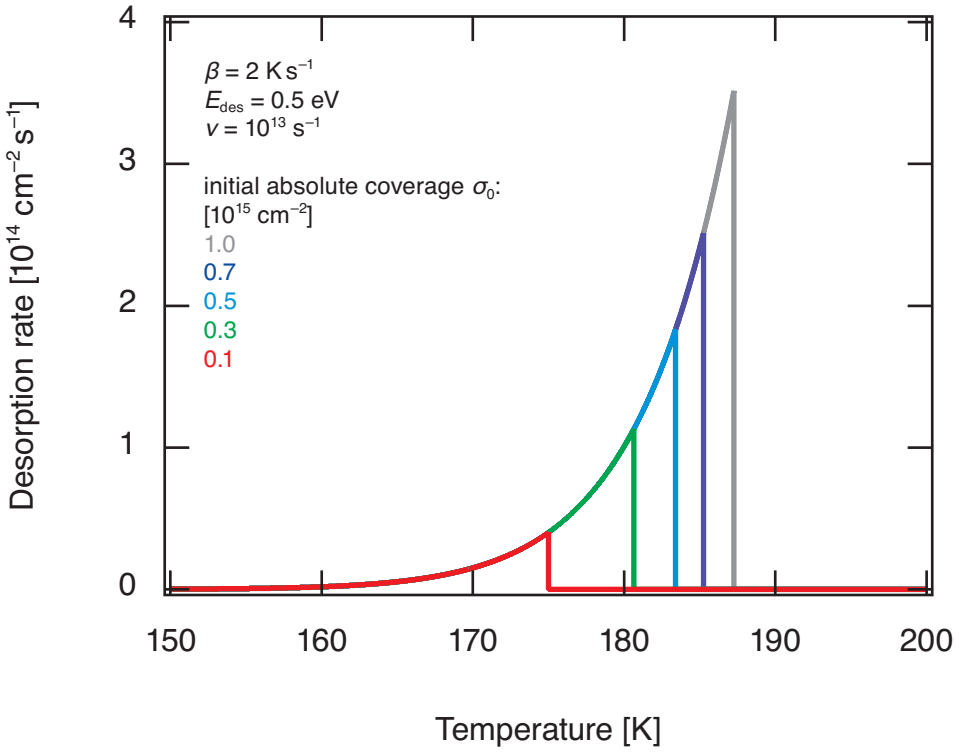

Figure 2.5: Model TPD curves for a zero-order desorption process

For first-order desorption kinetics ($n = 1$) the Polanyi–Wigner equation (2.28) turns into:

$$r_{\text{des}} = \nu\theta \exp\left(-\frac{E_{\text{des}}}{k_{\text{B}}T}\right). \text{ [1, 69]} \tag{2.31}$$

In this case, the desorption rate is proportional to the instantaneous coverage. The exponential energy component $E_{\text{des}}/k_{\text{B}}T$ and the coverage component $\nu\theta$ balance each other. First-order desorption is typical for the reversal of non-dissociative molecular or atomic adsorption processes. For first-order desorption, equation 2.29 turns into:

$$\Rightarrow \frac{E_{\mathrm{des}}}{k_{\mathrm{B}} T_{\mathrm{peak}}^2} = \frac{\nu}{\beta} \exp\left(-\frac{E_{\mathrm{des}}}{k_{\mathrm{B}} T_{\mathrm{peak}}}\right). \; [1,\ 69] \tag{2.32}$$

This indicates that the peak temperature T_{peak} is independent of the initial coverage. This leads to constant peak temperatures at different dosages. First-order desorption processes cause desorption peaks of asymmetric shapes. [1, 69]

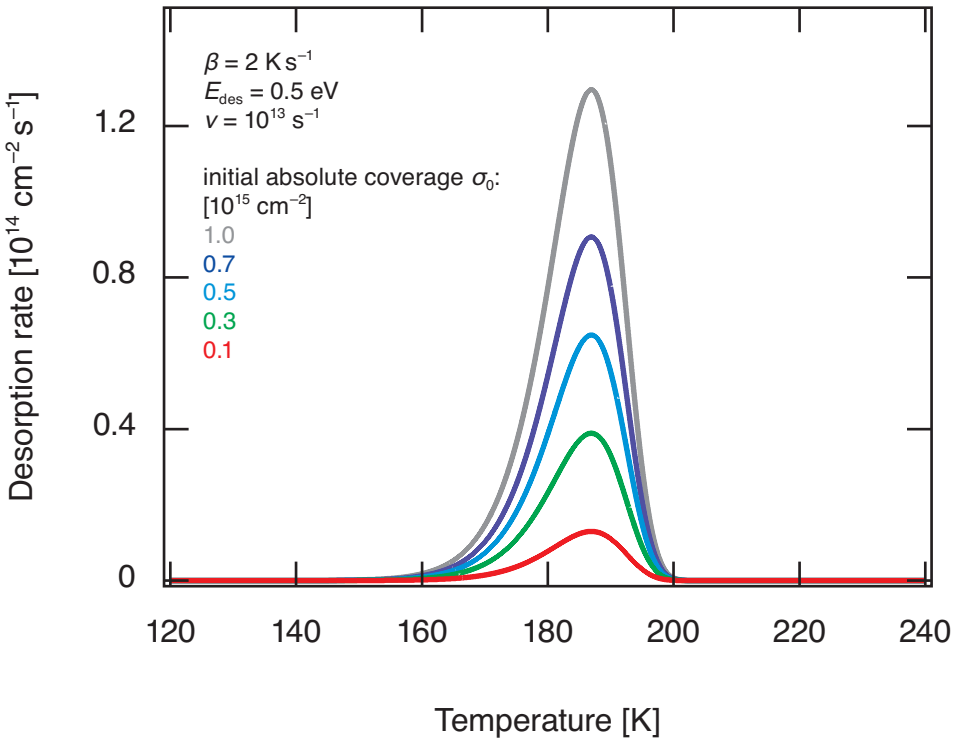

Figure 2.6: Model TPD curves for a first-order desorption process

For second-order desorption kinetics ($n = 2$) the Polanyi–Wigner equation (2.28) turns into:

$$r_{\mathrm{des}} = \nu \theta^2 \exp\left(-\frac{E_{\mathrm{des}}}{k_{\mathrm{B}} T}\right). \; [1,\ 69] \tag{2.33}$$

In this case, the desorption rate is proportional to the square of the instantaneous coverage. A second-order desorption is typical for recombinative desorption processes. Here, two adsorbate species have to combine on a sample

surface by diffusion processes in order to form the desorbing species. Evidently, a higher coverage offers more opportunities or shorter diffusion pathways for the combination step. Therefore, the peak temperature shifts to lower temperatures as the initial coverage increases. For a second-order desorption, equation 2.29 turns into:

$$\Rightarrow \frac{E_{\mathrm{des}}}{k_{\mathrm{B}} T_{\mathrm{peak}}^2} = \frac{2\nu^2}{\beta}\theta_p \ \exp\left(-\frac{E_{\mathrm{des}}}{k_{\mathrm{B}} T_{\mathrm{peak}}}\right). \ [1,\ 69] \tag{2.34}$$

Characteristically, second-order desorption curves exhibit a symmetric peak shape. For strong repulsive interadsorbate interactions also a pseudo-second-order desorption may be observed. In this case the desorption temperatures decrease with an increase in coverage as the repulsive interactions dominate for higher coverages. [1, 69]

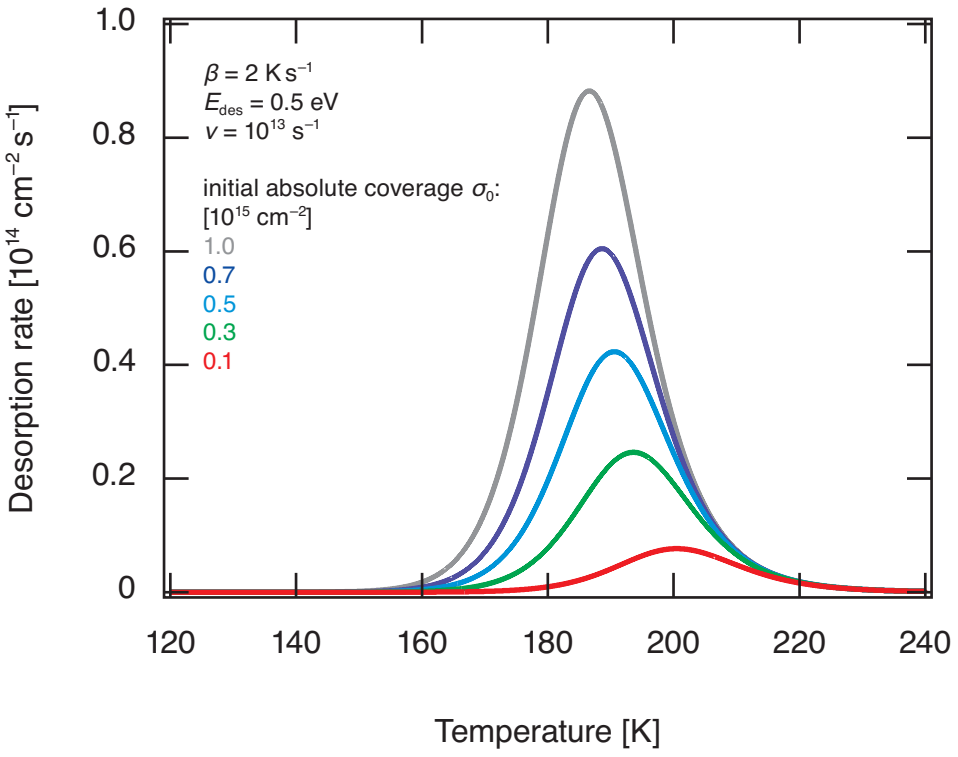

Figure 2.7: Model TPD curves for a second-order desorption process

Certain qualitative conclusions can be drawn from TPD spectra. Peaks at

lower temperatures refer to lower desorption activation energies—therefore weaker bound adsorbates. Accordingly, physisorbed adsorbates desorb earlier (at lower temperatures) than chemisorbed adsorbates. In addition, chemisorption is limited to a monolayer. Therefore, a certain TPD peak for a chemisorbed species saturates for coverages above $\theta = 1$. On the other hand, TPD peaks for physisorbed species do not saturate for multilayer coverages but scale with the initial coverage. Also different adsorption sites on a sample surface are distinguishable as the binding energy (and therefore the desorption activation energy) varies for steps, terraces, or plateaux on the surface. As polycrystalline surfaces exhibit a combination of different crystalline formations, the desorption spectrum is less defined but roughly comparable to TPD results from single crystals. [1, 69] Furthermore, the effect of boundaries between different crystallographic grains on polycrystalline surfaces might be of importance in surface reactivity. [70]

The parameter that is monitored in TPD experiments is the total desorption rate and therefore the total flux of all desorbing species in a unit of time from a unit area. An integration over all directions, velocities and internal energies is automatically performed, even if often strongly biased by the quadrupole mass analyzer. [68]

TPD spectra of water desorbing from Pt(111) crystalline surfaces show two desorption peaks: one associated with monolayer desorption at $\approx 170\,\mathrm{K}$ that follows zero-order desorption kinetics and a second peak at $\approx 150\,\mathrm{K}$ that is associated with multilayer desorption. In the presence of step sites, the water monolayer that is attributed to the co-existence of a condensed phase and a two-dimensional water-gas in submonolayer condition is stabilized. [71, 72, 73, 58] On step sites water tends to be more stable bound: for Pt(100) step sites an additional desorption peak at $\approx 188\,\mathrm{K}$ and for Pt(110) step sites an additional desorption peak at $\approx 197\,\mathrm{K}$ are observed. [58, 74] In TPD spectra of water desorbing from Pt(553) surfaces three desorption peaks are identified at $\approx 146\,\mathrm{K}$, $\approx 171\,\mathrm{K}$, and $\approx 197\,\mathrm{K}$, respectively. For low coverages below $0.28\,\mathrm{ML}$ only the desorption peak at $197\,\mathrm{K}$ is observed that develops a tail at the low temperature side with increasing coverage even before the peak saturates. This tail forms the desorption peak at $171\,\mathrm{K}$ between coverages of

0.42–0.91 ML. Both peaks show the characteristics of first-order desorption kinetics as they do not shift in temperature with increasing coverages. The third desorption peak at 146 K shows zero-order desorption kinetics and is associated with multilayer desorption. [58] If oxygen is co- or pre-adsorbed on the platinum surface such that atomic oxygen species are present, the TPD spectra for desorbing water changes. For coverages below 0.1 ML a two peak structure is observed at ≈ 200 K and ≈ 230 K, respectively, that shifts toward higher temperatures with increasing coverages. Both desorption peaks develop simultaneously and exhibit a comparable integral that saturates after a monolayer is established. With increasing coverages up to ≈ 0.54 ML a brought shoulder at lower temperatures grows that develops into three additional desorption peaks at ≈ 160 K, ≈ 170 K, and ≈ 185 K, respectively. At coverages above ≈ 0.86 ML another desorption peak grows in, that is assigned to multilayer desorption and shifts from initially ≈ 150 K toward higher temperatures with increasing coverages. [58]

As already discussed, the co-adsorption of O and H_2O on Pt(111) surfaces causes the formation of OH species that are stabilized in a hydrogen bonding network. Therefore, various stable conformations that depend on the O : H_2O ratio are established. [75, 76, 57, 56, 58] During TPD experiments, H_2O desorbs—or in other words: H_2O is titrated off the surface. As a result, the O : H_2O ratio changes. Therewith, the hydrogen bonding network rearranges and the stability of the H_2O molecules changes as well. It can be assumed, that the desorption peaks at higher temperatures represent a combination of H_2O desorption and recombinative desorption of $2\,OH_{(a)} + H_2O$ from hydrogen bonding networks of variable stability. [58] Whereas pre-adsorbed oxygen atoms on the Pt surface cause increased stabilities of adsorbed water, pre-adsorbed atomic hydrogen or deuterium species weaken the H_2O-Pt bonding. [77, 74, 78] Consequently, H_2O desorbs at lower temperatures in the presence of $H_{(a)}$ or $D_{(a)}$.

From Pt(111) surfaces physisorbed methanol desorbs at 145 K, chemisorbed mono- and submonolayer methanol desorbs at 194 K. The high desorption temperature tends to shift to 183 K with increasing coverage due to lateral repulsive interactions between methanol molecules on the Pt surface. [79] Sim-

ilar thermal desorption results are obtained for ethanol desorbing from Pt(111) surfaces except that the desorption temperatures are slightly higher than in the case of methanol. For lower coverages desorption of chemisorbed ethanol occurs at $\approx 215\,\mathrm{K}$. This temperature shifts to $\approx 200\,\mathrm{K}$ for saturation coverages. Desorption from ethanol multilayers occurs already at $\approx 155\,\mathrm{K}$. [79, 80] Alcohols are known to decompose over platinum and palladium surfaces already at $\approx 250\,\mathrm{K}$. [81]

Ammonia desorbs thermally from Pt(111) surfaces over a wide temperature range of 100–500 K with decreasing peak temperatures for increasing coverages due to repulsive interaction of the adsorbed NH_3 molecules. Three main peaks are observed at $\approx 350\,\mathrm{K}$, $\approx 160\,\mathrm{K}$, and $\approx 120\,\mathrm{K}$. Whereas the high temperature peak is attributed to strongly chemisorbed NH_3, the feature at $\approx 160\,\mathrm{K}$ represents weakly chemisorbed NH_3, and the lowest desorption temperature is attributed to physisorbed ammonia. It can be assumed that adsorbed NH_3 stays intact and does not decompose on Pt surfaces up to 450 K. [82]

TPD experiments from reconstructed Pt(110)-(1×2) surfaces reveal that multilayer coverages of formic acid desorb at 177 K whereas mono- and submonolayer coverages desorb at 208 K. [83] On clean Pt(111) surfaces low coverages of formic acid are adsorbed molecularly as monomers or discrete dimer pairs $(HCOOH)_2$ up to 100 K. For increasing exposures up to $D \approx 0.2\,\mathrm{L}$ hydrogen-bonded chains of β-polymorph solid-phase configuration are formed (see figure 2.8). For exposures above 0.6 L the β-polymorph chains rearrange into the more dense α-polymorph configuration (see figure 2.9). [84] At temperatures above 100 K formic acid deprotonates and bridging bidentate formate $HCOO_{BB(a)}$ is formed via a monodentate formate $HCOO_{M(a)}$ intermediate state (see figures 2.10 and 2.11):

$$HCOOH_{(a)} \longrightarrow HCOO_{M(a)} + H_{(a)} \tag{2.35}$$

$$HCOO_{M(a)} \longrightarrow HCOO_{BB(a)}\,. \text{ [84]} \tag{2.36}$$

At $\approx 150\,\mathrm{K}$ the β-polymorph chains reverse to discrete dimer pairs (see figure 2.12) and completely convert to bridging bidentate formate with increasing

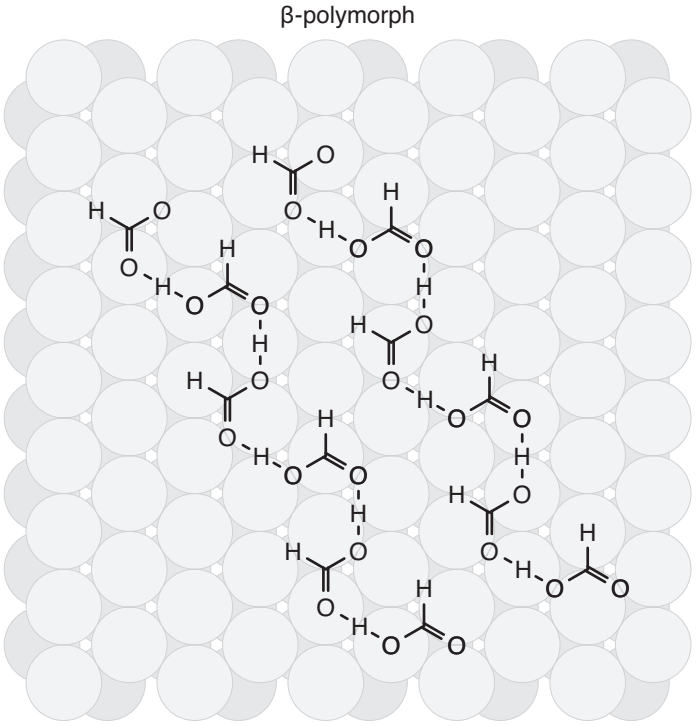

Figure 2.8: Model of β-polymorph overlayer structures of HCOOH on Pt(111): oxygen atoms occupy bridge sites or on-top sites, the bond angles are not distorted.

temperature up to 170 K. [84] At $\approx$ 200 K small amounts of adsorbed formate recombine with $H_{(a)}$ and desorb molecularly as:

$$HCOO_{(a)} + H_{(a)} \longrightarrow HCOOH_{(g)} \,. \text{ [84]} \tag{2.37}$$

At $\approx$ 260 K the majority of the adsorbed formate decomposes as:

$$HCOO_{(a)} \longrightarrow H_{(a)} + CO_{2(g)} \,. \text{ [84]} \tag{2.38}$$

Also non-decomposed and recombined formic acid desorbs already at 200 K as monomers. At $\approx$ 130 K α-polymorph chains transform to β-polymorph chains and desorption results from the depopulation of multilayers or from the rupture of monolayer chains. Subsequently, the desorption of dimers occurs and fractions of remaining monomers immediately deprotonate according to equations 2.35 and 2.36 to rearrange in bridging bidentate configurations. [84] Pre-

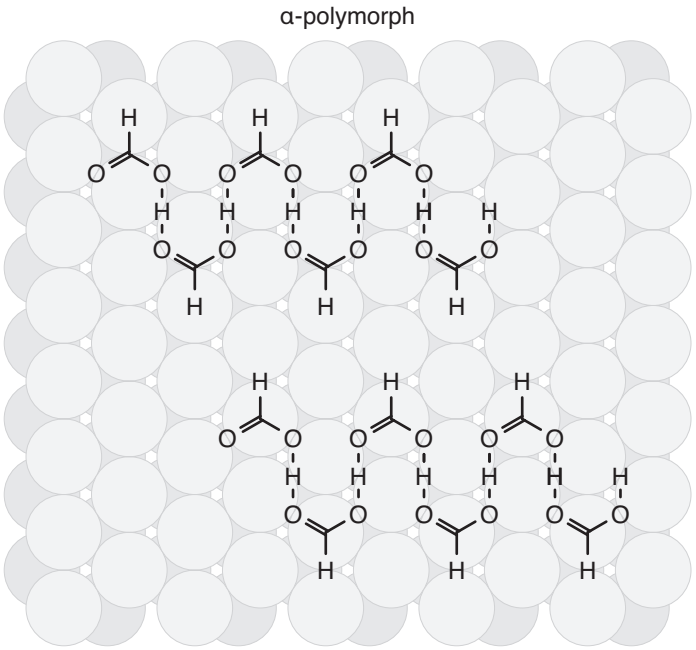

Figure 2.9: Model of α-polymorph overlayer structures of HCOOH on Pt(111): oxygen atoms occupy bridge sites, the bond angles are not distorted.

adsorbed oxygen facilitates the decomposition of formic acid on the Pt(111) surface and enables alternative reaction channels other than the unimolecular dehydrogenation. [85, 86, 87] At temperatures between 80–100 K formate molecules in the monodentate and the thermodynamically more stable bridging bidentate configurations are produced according to:

$$\mathrm{HCOOH_{(a)} + O_{(a)} \longrightarrow HCOO_{M(a)} + OH_{(a)}} \tag{2.39}$$

$$\mathrm{HCOOH_{M(a)} + OH_{(a)} \longrightarrow HCOO_{BB(a)} + H_2O_{(a)}}\,. \text{ [85, 86, 87]} \tag{2.40}$$

In contrast to larger amounts of water molecules that form hydrogen-bonded bilayers, the H_2O molecules formed in the course of the formic acid dehydrogenation remain isolated monomers that interact with the adsorbed formate molecules or pre-adsorbed oxygen atoms. [88, 86] With increasing temperature

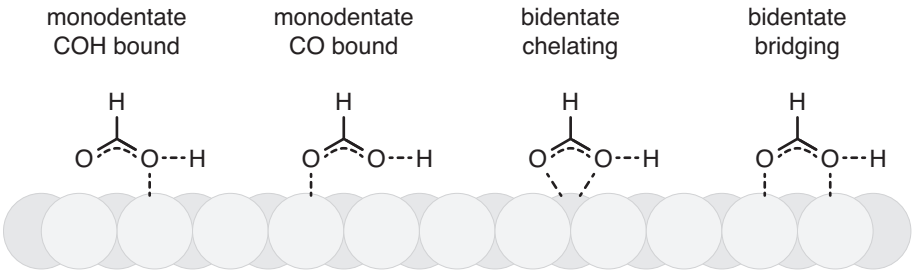

Figure 2.10: Adsorption configurations of formic acid

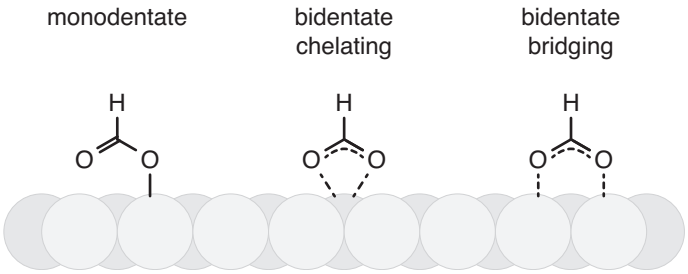

Figure 2.11: Adsorption configurations of formate

the adsorbed water reacts with adsorbed oxygen atoms according to equation 2.23. At temperatures above 210 K stabilizing water molecules desorb and above 250 K formate decomposes as:

$$2\,\mathrm{HCOO_{(a)}} + \mathrm{O_{(a)}} \longrightarrow \mathrm{H_2O_{(g)}} + 2\,\mathrm{CO_{2(g)}}\,. \text{ [86]} \tag{2.41}$$

The presence of oxygen atoms increases the formate stability relative to bare platinum surfaces and the maximum CO_2 desorption rate is reached at $\approx$ 280–315 K. [86] For formic acid exposures above 0.6 L carbon dioxide is also produced at much lower temperatures of $\approx$ 165–185 K according to:

$$\mathrm{HCOO_{(a)}} + \mathrm{OH_{(a)}} \longrightarrow \mathrm{H_2O_{(g)}} + \mathrm{CO_{2(g)}}\,. \text{ [86]} \tag{2.42}$$

Above 0.8 L carbon dioxide might also be produced without participating O, OH, or H_2O species at $\approx$ 165–185 K by the decomposition of two formate species according to:

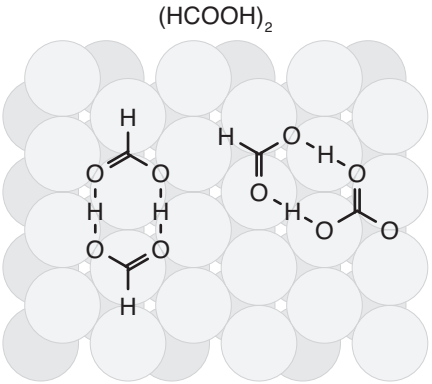

Figure 2.12: Model of dimer overlayer structures of HCOOH on Pt(111): oxygen atoms occupy bridge sites or on-top sites, the bond angles are not distorted.

$$2\,\mathrm{HCOO_{(a)}} \longrightarrow \mathrm{HCOOH_{(a)}} + \mathrm{CO_{2(g)}}\,.\ [86] \tag{2.43}$$

Here, the produced formic acid remains adsorbed on the surface in a non-deprotonated configuration up to 200 K—then it desorbs. [86] At higher temperatures above 250 K also water has already desorbed and OH has been deprotonated so that only formate and atomic oxygen have remained on the Pt(111) surface and react in the temperature range of 280–315 K as:

$$2\,\mathrm{HCOO_{(a)}} + \mathrm{O_{(a)}} \longrightarrow 2\,\mathrm{CO_{2(g)}} + \mathrm{H_2O_{(g)}}\,.\ [86] \tag{2.44}$$

At 250–315 K and in absence of atomic oxygen, formate might also react according to:

$$\mathrm{HCOO_{(a)}} \longrightarrow \mathrm{H_{(a)}} + \mathrm{CO_{2(g)}} \tag{2.45}$$

$$\mathrm{HCOO_{(a)}} + \mathrm{H_{(a)}} \longrightarrow \mathrm{HCOOH_{(g)}}\,.\ [86] \tag{2.46}$$

It is assumed that monodentate formate is the key intermediate in the direct oxidation pathway to carbon dioxide and bridging bidentate formate (or possibly chelating bidentate formate as well) acts as dead end in the net reaction. [87] As the activation barrier for the conversion of bidentate formate to monoden-

tate formate closely equals the overall formic acid decomposition barrier for reaction 2.38, the rate limiting reaction step here is the breaking of one Pt–O bond of the adsorbed bidentate formate to form monodentate formate. Therewith, the surface-catalyzed decomposition of formic acid can be described as a reaction sequence of:

the oxidation of adsorbed formic acid according to reaction 2.35,

the predominant conversion of monodentate formate to bidentate formate according to reaction 2.36 up to a remaining minor equilibrium concentration of monodentate formate,

the exothermic decomposition of monodentate formate to carbon dioxide according to reaction 2.38 with an enthalpy of $-80\,\mathrm{kJ\,mol^{-1}}$,

the bidentate–monodentate conversion in order to establish the concentration equilibrium again,

and the alternate repetition of the previous two steps until all formate is consumed. [87]

Thermal desorption spectra of formic acid desorbing from clean Pt(111) surfaces reveal that HCOOH desorbs at $\approx 160\,\mathrm{K}$ in dimers or oligomers from multilayers and molecularly at $\approx 200\,\mathrm{K}$. Small amounts of molecular desorption are also observed in the temperature range of ≈ 200–$250\,\mathrm{K}$ and are attributed to the recombination of adsorbed formate and hydrogen species. Decomposed formic acid is observed as CO_2 desorption features at $\approx 200\,\mathrm{K}$ and $\approx 250\,\mathrm{K}$. [84] Thermal desorption spectra of formic acid desorbing from Pt(111) surfaces precovered with oxygen exhibit two desorption features at $\approx 200\,\mathrm{K}$ and $\approx 280\,\mathrm{K}$ that are attributed to molecular HCOOH desorption and three desorption features that are attributed to multilayer desorption of dimers and oligomers at $\approx 200\,\mathrm{K}$, $\approx 155\,\mathrm{K}$, and $\approx 145\,\mathrm{K}$. [86]

3 Experiments

In order to perform temperature programmed desorption experiments from the surfaces of MIM chemoelectronic nanodiodes, methods of sample heating were studied already prior to the experiments presented here. Those earlier experiments and sample designs revealed that backside heating with deposited metal nanofilms is feasible and comparable to the direct heating of a top metal film. [69] Subsequently, it was observed that backside and frontside heating by using similar transition metal films (in this case platinum) with similar heating currents lead to comparable heating rates. Here, platinum films (20 mm $\times$ 4 mm) of 8 nm thickness were deposited on the front- and on the backside of a commercial 10 mm $\times$ 20 mm cover slip (Menzel-Gläser #3, thickness: $\approx$ 0.2–0.3 mm). The resistance–temperature relation of the Pt films was used to measure the temperature after calibrating (see section 3.3.1). In this case, the frontside Pt film was used to measure the temperature of the sample while the backside Pt film was used to heat the sample and vice versa (see figure 3.1). The temperatures that were recorded using the frontside and the backside heating method deviated between 5 K and 12 K with higher temperature values measured while heating from the backside. Besides the fact that this deviation lies close to the accuracy limit of this method of temperature measurement, this could also be attributed to a higher heat dissipation due to radiation from the frontside Pt film into the vacuum. Additionally, the temperature close to the sample on the sample holder was measured using a Pt1000 resistance–temperature sensor. It could be shown that both films (the frontside and the backside film) heat predominantly the glass substrate—the sample holder remains cold.

In order to heat the samples from the backside reproducibly over a wide

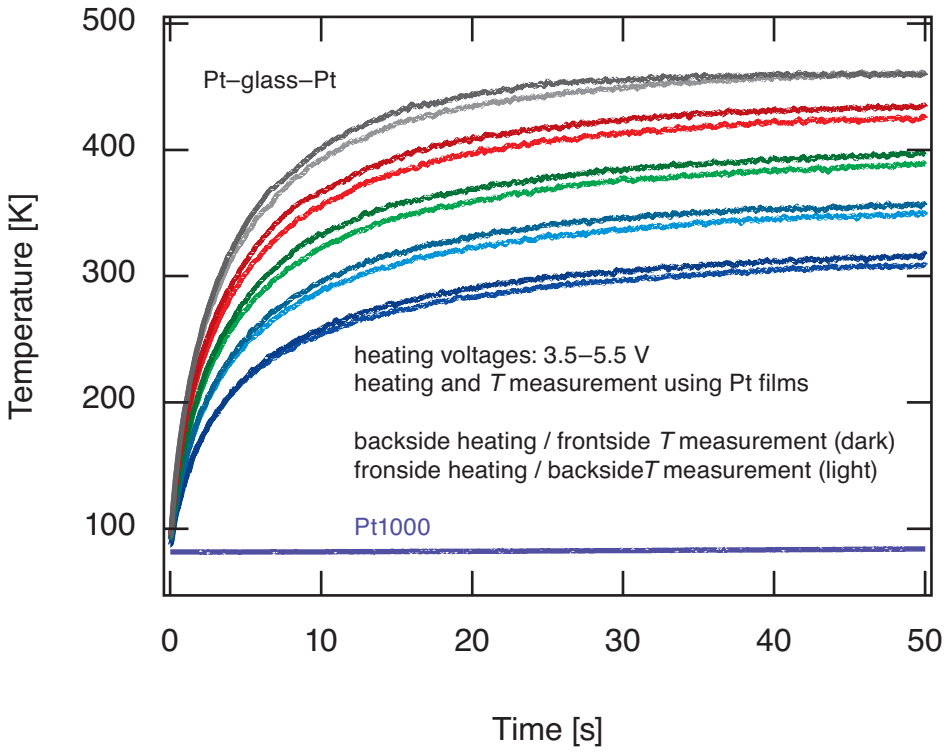

Figure 3.1: Heating and temperature measurement on a glass sample by using a backside and a frontside Pt film: backside heating and frontside temperature measurement or frontside heating and backside temperature measurement led to similar results, a Pt1000 resistance–temperature sensor (mounted close to the sample) did not detect a significant heating at the sample holder due the heating cycles.

temperature range of 60–600 K by applying voltages in a range of 1–20 V, commercial indium tin oxide (ITO) films deposited on 1.1 mm thick glass substrates were tested (see figure 3.2). ITO films with sheet resistances of $R_{\square} = 20\,\Omega$ allowed to heat the glass substrate from 100 K up to 600 K by applying voltages of 6–9 V. Meanwhile, the temperature of the sample was measured using a Pt1000 resistance–temperature sensor that was glued on top of the glass substrate with conducting carbon cement (Leit-C nach Göcke). These first ITO tests revealed that thicker glass substrates were less fragile during mounting, connecting, and heating. Thus, also thicker glass substrates were used henceforth. In previous experiments also Ag and Ti films deposited on the backside of the sample were used in order to heat the sample. Due to the fact that

ultra-thin Ag films had to be used because of the exceptionally good conductivity of silver, the prepared films were susceptible to oxidation and therefore ephemeral. The further use of Ti films was avoided due to the similar thermal desorption temperatures of various adsorbates from Ti compared to the desorption from Pt. No clear TPD spectra would be observable by using Ti and Pt films simultaneously but a mixture of desorption events from both metal surfaces.

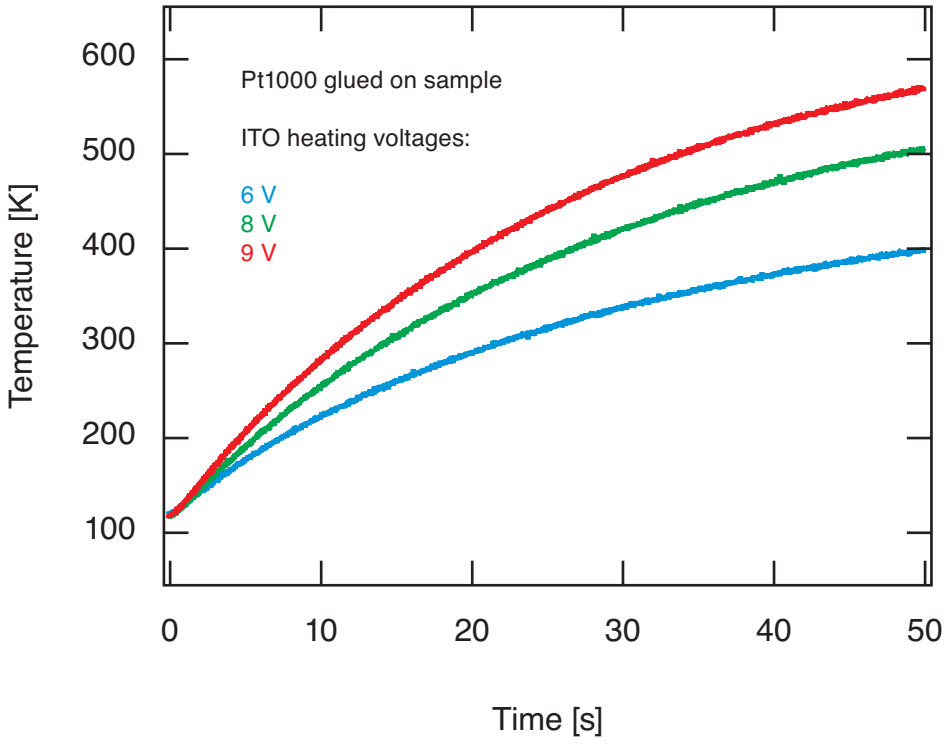

Figure 3.2: Heating of a glass sample by using commercial indium tin oxide films of $R_{\square} = 20\,\Omega$ deposited on the backside of the glass

All the insights revealed by these preliminary tests and some improvements in cleaning and handling the samples during the preparation steps were considered to draw up a new sample design that exhibits a backside indium tin oxide film in order to heat the sample, a 0.5–0.6 mm thick glass substrate, and a chemoelectronic nanodiode sandwich structure (Pt–Ta_2O_5–Ta) deposited on the frontside (see figure 3.3).

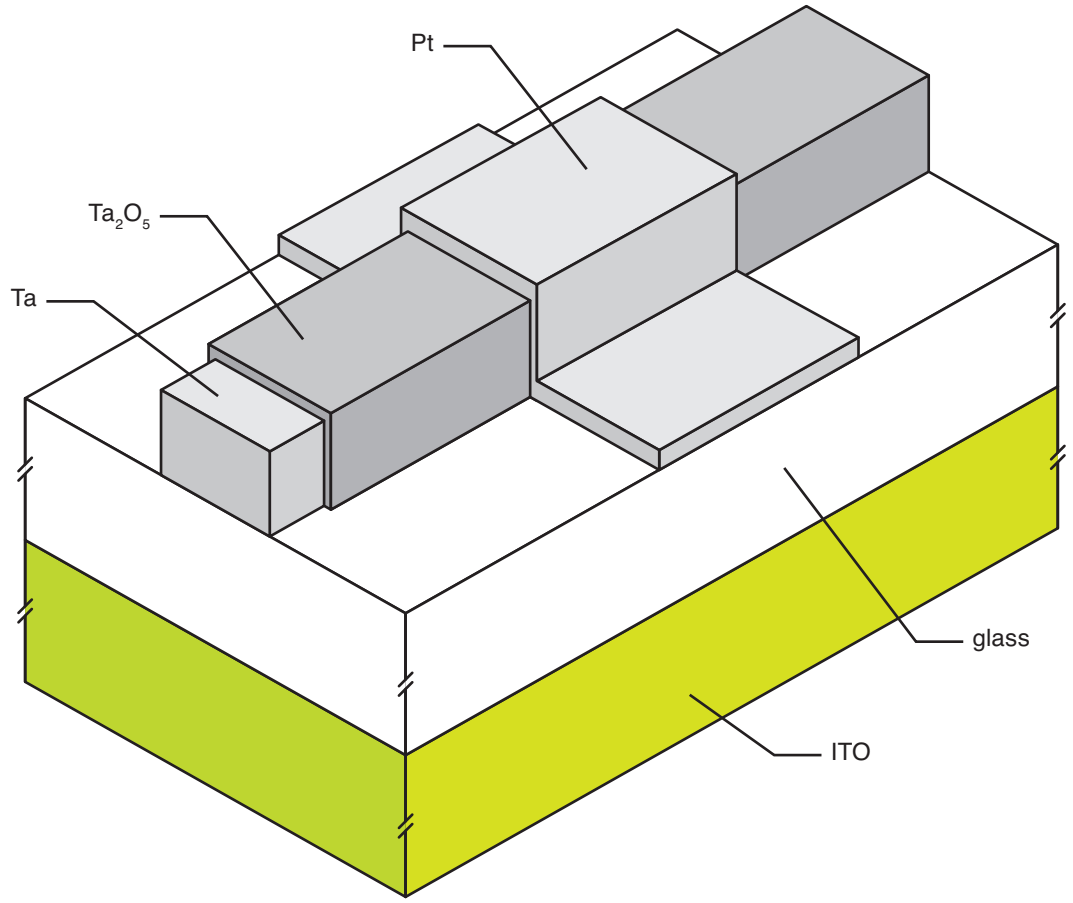

Figure 3.3: Sample design

3.1 Sample preparation

Glass substrates of 9 mm × 20 mm were cut manually from commercial cover slips (Menzel-Gläser #5, thickness: ≈ 0.5–0.6 mm). The substrates were rinsed with acetone and wiped of with lint-free paper towels (KIMTECH Science, precision wipes). Subsequently, all glass substrates were positioned in a polytetrafluoroethylene (PTFE) sample holder and cleaned stepwise in various solvents and solvent mixtures using a heatable sonic bath as listed in table 3.1. All organic solvents (acetone, ethanol, and isopropyl alcohol) were of AR (analytical reagent) grade quality. Ultra-pure water with a resistivity of 18.2 MΩ cm at 25 °C (purified by a Merck Millipore Simplicity water purification system)

was used in order to prepare the aqueous solutions. Fuming hydrochloric acid (37 %, AR grade), aqueous ammonia solution (33 %, AR grade), and aqueous hydrogen peroxide solution (30 %, AR grade) were used for the alkaline solvent (step 4) and respectively the acidic solvent (step 5). Following the last cleaning step in ethanol the samples were wiped of with lint-free paper towels and stored in argon atmosphere between PTFE sheets for transport.

Step	Solvent (mixture)	T [°C]	t [min]
1	$(CH_3)_2CO$	40	30
2	CH_3CH_2OH	60	30
3	$(CH_3)_2CHOH$	60	30
4	5 H_2O + $H_2O_{2(aq)}$ + $NH_{3(aq)}$	70	30
5	6 H_2O + $H_2O_{2(aq)}$ + HCl	70	30
6	H_2O	70	30
7	H_2O + $(CH_3)_2CHOH$	60	30
8	$(CH_3)_2CHOH$	60	30
9	CH_3CH_2OH	60	30

Table 3.1: Cleaning procedure within the sample preparation

In order to avoid short circuits to the frontside metal films the indium tin oxide was deposited exclusively on an area that does not include the edges of the glass substrate by using a shutter mask made of polyimide tape (DuPont Kapton HN general-purpose film) that was glued on the cleaned glass substrates prior to the ITO deposition step. For a better handling seven glass samples were placed together on a 76 mm × 26 mm glass support that was covered with polyimide tape in advance. The samples were fixed with additional strips of polyimide tape. Collectively these strips added up to form the shutter mask (see figure 3.4). Thus, the mounting of the samples for ITO sputter deposition was considerably simplified and less susceptible to contamination as all cleaned samples were collectively mounted on only two glass supports into the vacuum system.

The indium tin oxide films were deposited at the technical physics laboratories of the faculty of physics in Duisburg using physical vapor sputter

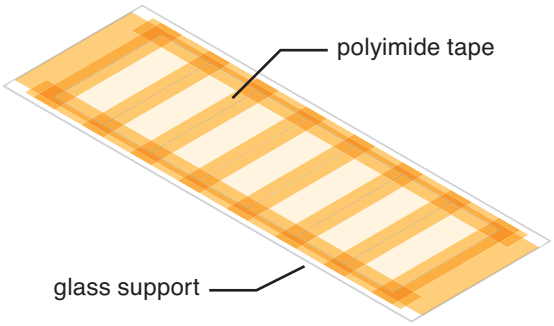

Figure 3.4: Shutter mask made of polyimide tape strips

deposition. The samples were mounted in a Perkin Elmer 2400 sputtering system that was pumped down to base pressure of $p_b = 1.7 \times 10^{-5}$ mbar. Argon gas (25 $cm^3\,min^{-1}$ at a standard temperature and pressure) was fed into the sputtering system. Consequently, the pressure inside the system increased to a working pressure of $p_w = 6.1 \times 10^{-3}$ mbar. An argon plasma was generated in the region in front of the target using a magnetron arrangement behind the indium tin oxide target. Ionized, positive charged, Ar ions were accelerated in an electric field generated by applying a bias voltage of $U_{bias} = 1.2$ kV toward the negative charged indium tin oxide target. After 15 min pre-sputtering in order to clean the surface of the ITO target, the samples were moved close to the target and fragments of the Sn-doped In_2O_3 were deposited on the glass substrates. During sputtering the temperature of the sample plates increased up to a maximum of 413 K. After 30 min of sputtering the system was shut down and the samples were removed. Measurements of the deposited ITO films showed a sheet resistance of $R_\square \approx 30\,\Omega$.

Subsequently, the polyimide tape mask was removed and the samples were mounted on the PTFE sample holder in order to be cleaned again using the heatable sonic bath as discussed above. But this time the acidic step was skipped, because it would have damaged and removed the deposited ITO films. The dry and clean samples were stored in argon atmosphere between PTFE sheets in a container that was opened again in a clean-room environment at Forschungszentrum Jülich for depositing 30 nm of tantalum on the top side of the glass substrate by means of e-beam physical vapor deposition. The

samples were mounted under a shutter mask that covered the entire sample area except a narrow strip of 2–3 mm width along the length of each sample. Using a modified Balzers PLS 500 UHV system tantalum was deposited at a working pressure of $p_w = 9 \times 10^{-7}$ mbar. An electron accelerating bias voltage of $U_{bias} = 10\,kV$ was applied between an electron emitting filament and the Ta target (chunks of tantalum in a crucible). Electrons left the filament according to a set emission current of $I_{em} = 0.1$–$0.3\,A$ and were directed onto the Ta target by means of a magnetic field. After deposition, the samples were put back in a container between PTFE sheets in argon atmosphere, were transported back to Essen, and were stored there until continuing with the electrochemical anodic oxidation of the tantalum. The prepared Ta films were of amorphous character with sheet resistances of $R_\square \approx 1\,k\Omega$. [89]

For this purpose, the samples—one after another—were mounted on an acryl glass sample holder (see figure 3.5) with a separating sheet of Parafilm M in order to protect the backside ITO films from scratches. The samples were fixed with a Au clip on top of the Ta film close to the edge of the samples. The fixed tantalum films were then electrochemically oxidized by means of an electrolytic droplet cell in a three electrode setup mounted into a steel Faraday cage (see figure 3.5). [90, 91, 92] Before usage, the glass equipment was rinsed with boiling ultra-pure water. The electrolyte solution was prepared by solving 73.8 g of freshly opened anhydrous sodium acetate (99 %, AR grade) in 1 l of ultra-pure water. In such highly concentrated $0.9\,mol\,l^{-1}$ sodium acetate solution the resistivity of the droplet cell is below $10\,\Omega$ and the potential drops in the solution are therewith negligible. The sodium salt of acetic acid was used, because the organic anion CH_3COO^- has a low tendency for incorporation into the tantalum during the oxide growth. In addition, the electrolyte buffers the solution and minimizes parallel corrosion processes such as dissolving oxide species. [90]

A droplet of the electrolyte solution was set gently on top of the tantalum film while an initial potential of $E_0 = -1.1\,V$ was applied between counter and working electrode. All potentials were referred to a saturated calomel electrode (SCE). The electrochemical potential difference that was applied between the tantalum film used as working electrode and the counter electrode (the

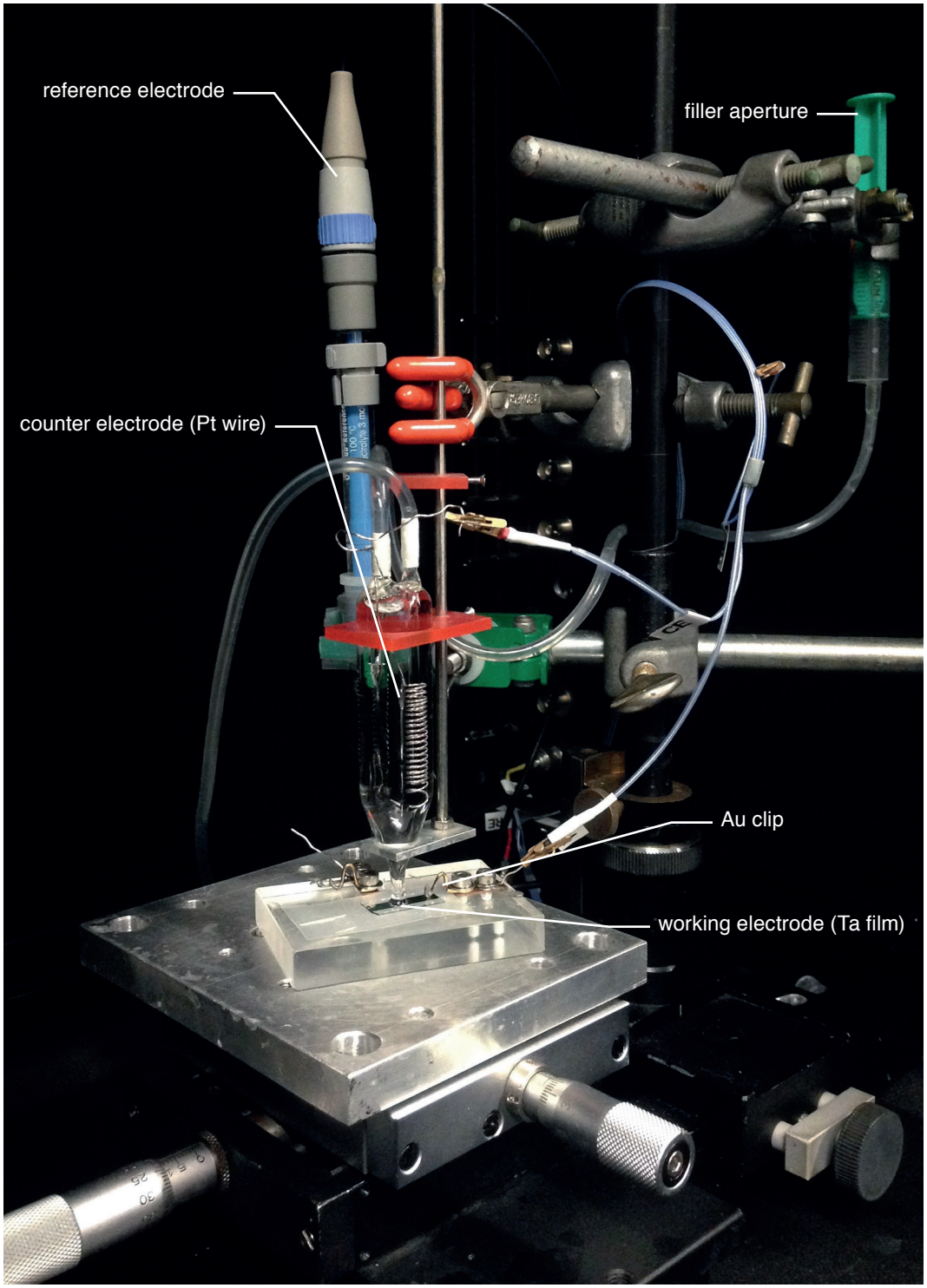

Figure 3.5: Setup of the electrochemical anodic oxidation of a Ta film

platinum wire) dropped only at the metal–electrolyte interface and therefore resulted in the oxidation of the top tantalum layer. Afterward, potential ramps were performed up to 2.4 V using a scan rate of $0.1\,\mathrm{V\,s^{-1}}$ (see figure 3.6). The oxide formation caused a passivation of the surface so that no oxidation currents flowed anymore for voltages below the previously applied voltages. As soon as this passivation was achieved the droplet was moved from the tantalum, the samples were rinsed carefully in ultra-pure water, and dried again in a stream of N_2 gas. This procedure of spot oxidation was repeated on all areas of the tantalum film except the contact area where the Au clip was placed. Subsequently, a set droplet was moved carefully over the tantalum surface while keeping the reverse potential constant at $E_{\mathrm{rev}} = 2.4\,\mathrm{V}$ in order to check that the surface was passivated completely.

The potentiostatic oxidation reduced the thickness of the evaporated amorphous Ta film and formed a Ta_2O_5 layer on top. According to [90] a tantalum consumption factor $r_{\mathrm{cons}} = 1.1\,\mathrm{nm\,V^{-1}}$ and an oxide formation factor $r_{\mathrm{form}} = 1.7\,\mathrm{nm\,V^{-1}}$ were assumed. Due to the applied reverse potential of $E_{\mathrm{rev}} = 2.4\,\mathrm{V}$ a Ta consumption of $\approx 1.7\,\mathrm{nm}$ and an oxide formation of $\approx 4\,\mathrm{nm}$ resulted. Thus, the prepared 30 nm thin Ta layer was reduced to a thickness of 27.4 nm and 4 nm of Ta_2O_5 were formed on top.

Finally, 7 nm of platinum were deposited on top of the oxidized Ta under UHV conditions (base pressure: $p_{\mathrm{b}} = 1 \times 10^{-9}\,\mathrm{mbar}$, working pressure: $p_{\mathrm{w}} = 1 \times 10^{-7}\,\mathrm{mbar}$) by means of electron beam physical vapor deposition in order to add the top metal electrode of the MIM chemoelectronic nanodiode. Here, a bias voltage of $U_{\mathrm{bias}} = 1.5\,\mathrm{kV}$ was applied between a hot filament and the Pt target (a Pt wire wrapped around a molybdenum rod). The filament was made of tungsten wire (diameter $d = 0.3\,\mathrm{mm}$, $R \approx 1.5\,\Omega$) and was heated by passing a current of $I_{\mathrm{fil}} = 6$–$7\,\mathrm{A}$ through it. When an emission current of $I_{\mathrm{em}} = 55\,\mathrm{mA}$ was reached the shutter was opened in order to start with the Pt deposition. Again, the sample substrate was kept at room temperature and the thickness of the Pt film was monitored during the deposition process using a quartz crystal microbalance. With each PVD run two samples were prepared. $4\,\mathrm{mm} \times 9\,\mathrm{mm}$ strips of platinum were deposited on top of each oxidized tantalum film by using a shutter mask that was made of copper tape. Simultaneously, the copper

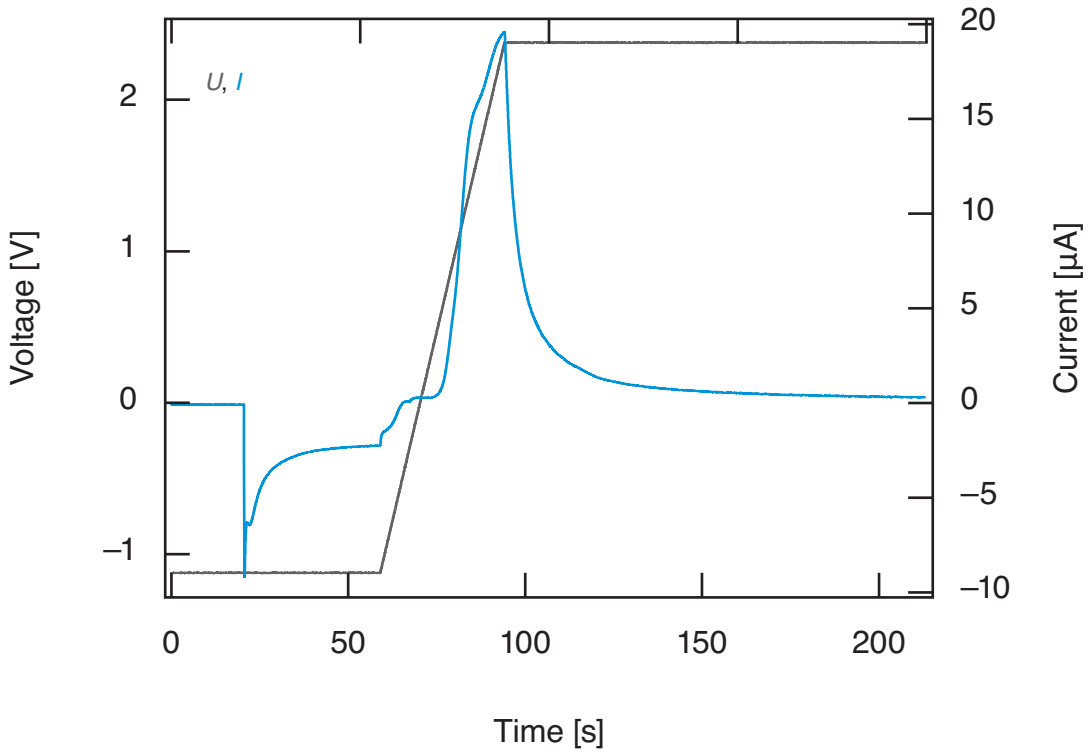

Figure 3.6: Oxidation and passivation of a Ta film by means of the presented electrochemical approach: at 20 s the droplet was set onto the Ta film and native tantalum oxide was reduced (current decrease), the film was oxidized again while the voltage was increased up to 2.4 V, at a constant voltage no further oxidation occurred and the current decreases due to passivation.

tape fixed the samples to the sample holder. A sheet of Parafilm M was placed between the copper tape and the sample in order to protect the Ta_2O_5. After deposition the samples were electrically contacted (see figure 3.7) with thin copper wires (diameter of 0.1 mm) using conducting carbon cement. The bare copper wires were shielded using polyimide tape and textile casings.

3.2 Experimental setup

All measurements were carried out in a stainless steel UHV system pumped to a base pressure of $p_b \approx 2 \times 10^{-10}$ mbar by means of mechanical, turbo molecular, and getter pumps. Two separable stainless steel vessels (a big one as

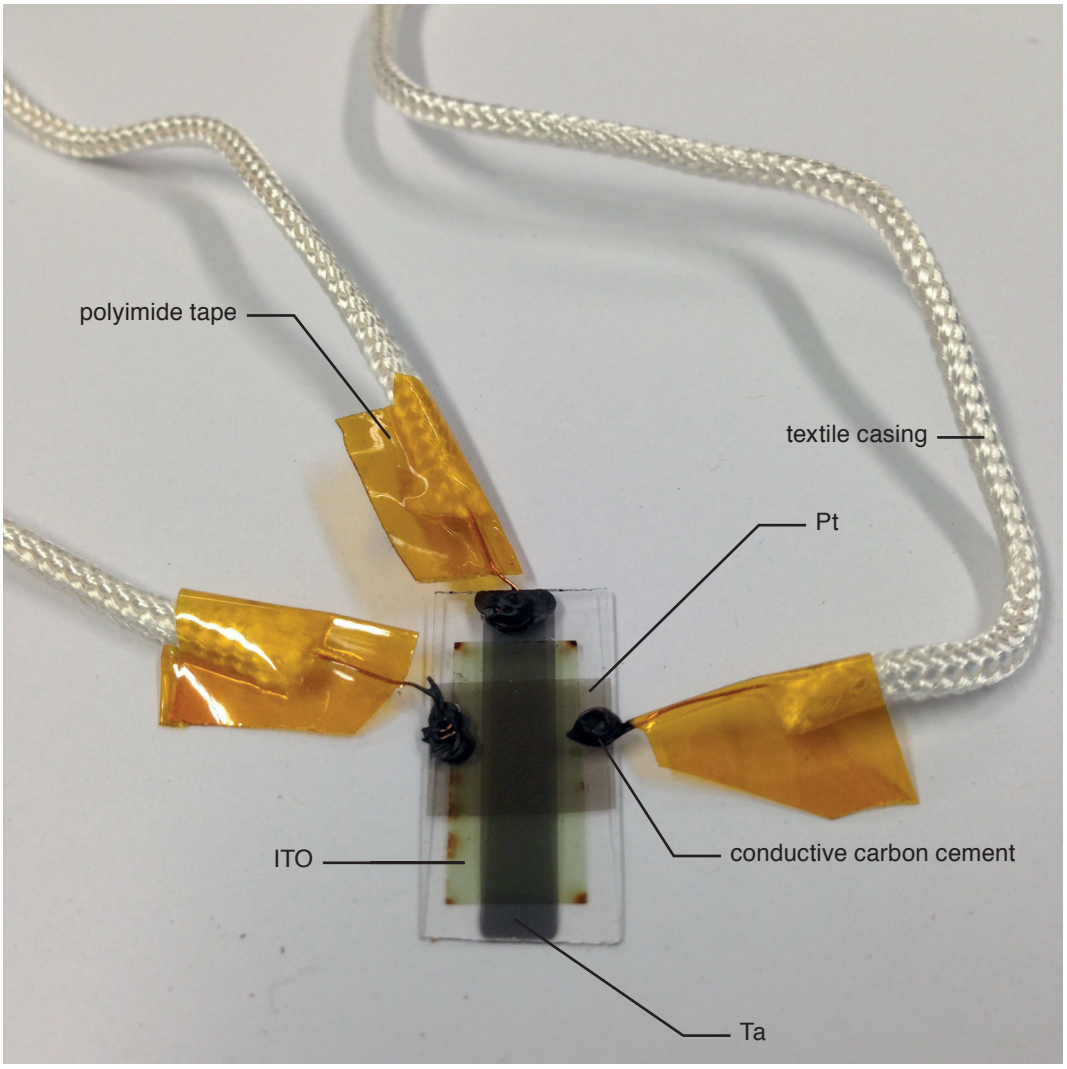

Figure 3.7: Electrical contacts glued onto the sample using carbon cement

the actual experiment volume and a smaller one as a reservoir for gas mixtures) were each pumped using a pre-vacuum line pumped by Pfeiffer ONF 25L rotary vane pumps down to 1×10^{-3} mbar. The main experiment vessel was pumped by two turbo molecular pumps, a Leybold 85541 turbo molecular pump (turbo molecular pump #1 in figure 3.8) directly attached behind a titanium sublimation pump close to the main chamber and a Leybold TW 70H turbo molecular pump (turbo molecular pump #2 in figure 3.8) connected

within a by-pass line at the side of the vessel.

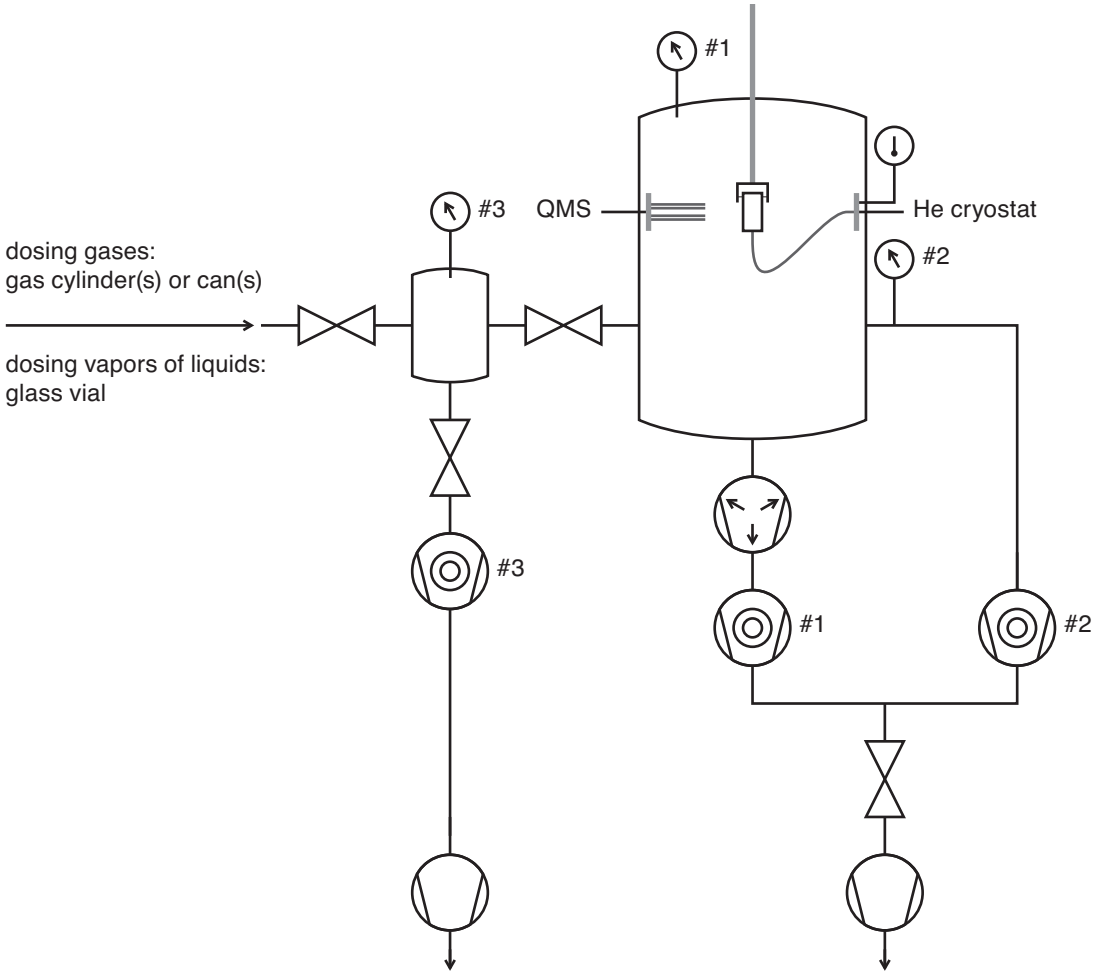

Figure 3.8: Experimental setup

A Ti sublimation getter pump, was used at pressures below 1×10^{-8} mbar to further decrease the pressure. A Ti getter layer was sublimated periodically (once per hour for a duration of 30 s) from solid Ti electrodes that were heated by passing a current of 40 A through them. Liquid nitrogen was used to cool the sublimation surface and increase the efficiency of the sublimation pump [1, 93, 94, 95]. The use of a cryogenic helium pump—primarily used as a cryostat to cool the sample below 70 K—had an additional influence on evacuating the system as gas was freezing out and condensed on the cool parts of the Leybold–

Heraeus RW2 cryostat system. Considering the temperature persistency of the MIM devices several mild baking procedures were carried out to improve the vacuum inside the chamber. Baking the chamber while cooling the sample simultaneously using the He cryostat enabled more intense heating currents (resulting in temperatures above 400 K at the walls of the chamber) while the samples stayed cool ($\approx 150\,\mathrm{K}$). The sensitive parts of the cryostat system were shielded with aluminum foil and could be held to temperatures below 315 K. The temperature was measured with a thermocouple mounted close to the cool head of the cryostat.

An MKS Spectra Satellite LM61 quadrupole mass analyzer was used to detect desorbing species or fragments of those species. While the ionization voltage was kept at $\approx 65\,\mathrm{V}$ during all experiments the detected mass, the sensitivity range, the accuracy, and the bias voltage of the photomultiplier were modified regarding the specific experimental focus.

The pressure inside the main chamber was measured using two pressure gauges: a nude AML Bayard-Alpert ionization gauge close to the sample holder (pressure gauge #1 in figure 3.8) operated using an AML PGC2D ionization gauge process controller and a Leybold Vacuum IONIVAC ITR 90 combination gauge (pressure gauge #2 in figure 3.8) at the transition area to the by-pass line operated using a Leybold Vacuum COMBIVAC IT23 process controller. The by-pass line was pumped by an additional turbo molecular pump (turbo molecular pump #2 in figure 3.8). The Leybold combination gauge (a combination of a Bayard Alpert hot cathode ionization measurement system for pressures above $2 \times 10^{-2}\,\mathrm{mbar}$, a Pirani system for pressures below $5.5 \times 10^{-3}\,\mathrm{mbar}$, and combined measurements for pressures in between) was separated from the main chamber by a copper shield to prevent radiation of the hot filament interfering with the measurements. For the same reason the nude AML Bayard-Alpert ion gauge close to the sample holder was switched off during adsorption and desorption experiments and for the temperature measurement calibrations.

A stainless steel gas inlet system was used to prepare mixtures of gases and vapors of liquids that were dosed into the main chamber precisely through a needle valve. The pressure inside the gas inlet system was measured using two

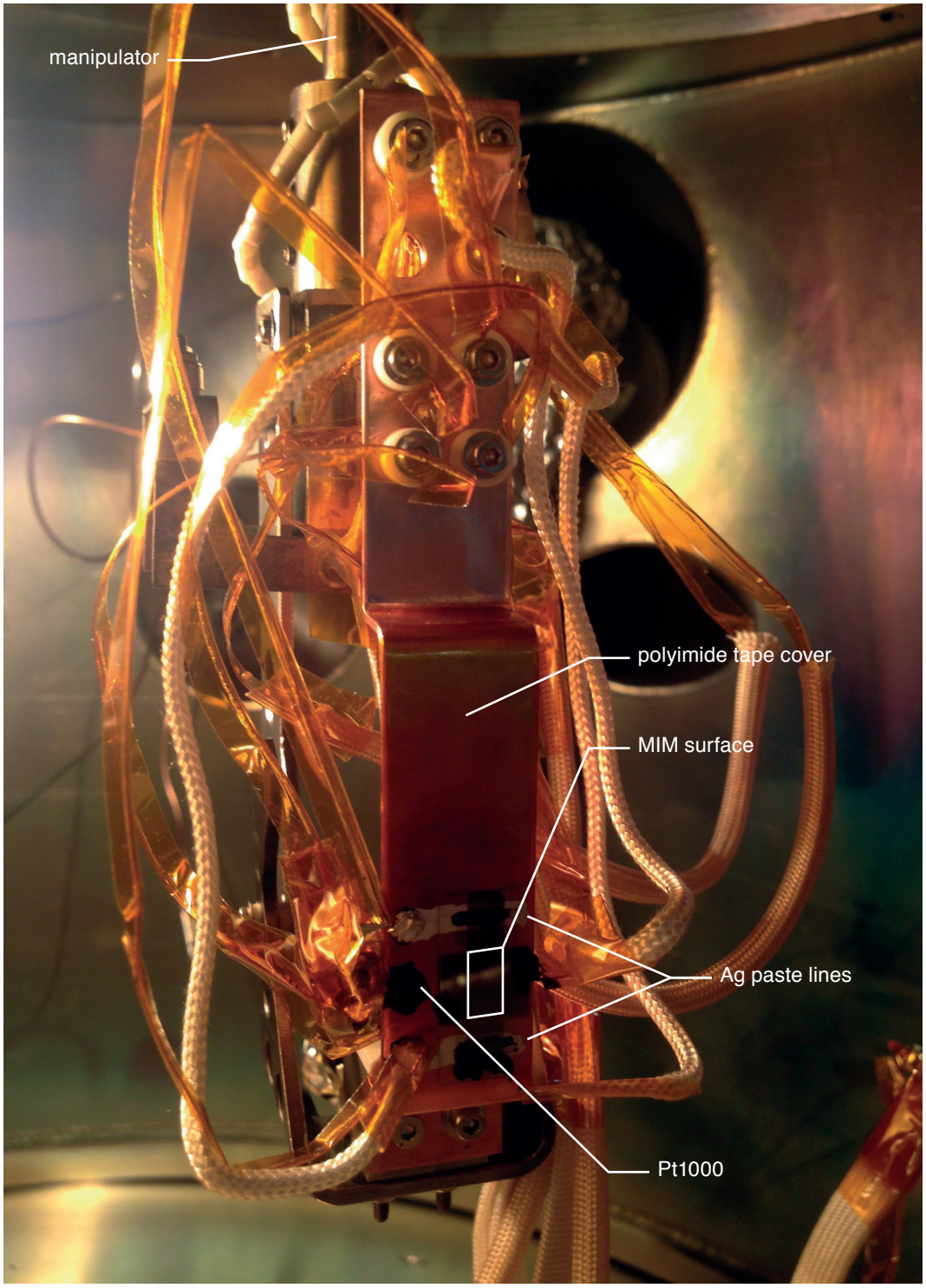

Figure 3.9: Sample holder, sample arrangement, and electrical contacts

capacitive pressure gauges (combined as pressure gauge #3 in figure 3.8): an MKS Baratron for pressures in the range of 0.1–1000 mbar and an Edwars Barocel for pressures in the range of 0.001–1 mbar, read out collectively using an MKS PDR-C-2C/SP control unit. Either a glass vial filled with liquids or steel gas cylinders or gas cans or both combined were used to feed the stainless steel vessel reservoir via three possible connections. The reservoir was pumped via a separate vacuum line using a water cooled Pfeiffer TMU 261 turbo molecular pump (turbo molecular pump #3 in figure 3.8).

The sample holder was cut and bent out of a 2 mm thick copper sheet. Two holes were drilled in order to screw the sample holder on a copper block at the end of the copper wire attached to the He cryostat. The copper block itself was mounted to the central manipulator through separating Macor glass-ceramic plates in order to reduce thermal conduction from the manipulator to the cryostat system. Additional holes were drilled in order to mount interface connections for the electric contacts using insulating Al_2O_3 sockets. The area where the sample was intended to be placed was electrically insulated using polyimide tape. Two lines of conductive silver paste were drawn on the polyimide tape surface and electrically contacted to two thin copper wires using conductive carbon cement. The copper wires were contacted each to one interface screw mounted at the sample holder.

It turned out that mounting the sample was best performed as follows:

1. The sample was glued onto the conductive silver paste lines with the ITO covered backside facing the sample holder using two spots of conductive carbon cement. The sample was carefully pressed onto the sample holder using the weight of tweezers and left under that condition for a duration of 2–3 h allowing the carbon cement to dry. Thereby, the ITO film was contacted to the silver paste lines and the sample was durably fixed to the sample holder.

2. A Pt1000 resistance–temperature sensor was glued with conductive carbon cement onto the polyimide tape area close to the sample. Again the carbon cement was left to dry for 2–3 h while the sensor was pressed onto the sample holder using a pair of fixing tweezers.

3. All electrical contact wires were fixed to the interface connections at the sample holder: two contacts of the ITO film, two contacts of the Pt1000 resistance–temperature sensor, and three contacts of the samples electrodes (one contact that was fixed at the end of the Ta strip, two contacts that were fixed at the ends of the Pt strip).

4. The sample holder was mounted with two screws to the copper block at the end of the copper wire attached to the He cryostat. Care was taken that no thermal or electrical connection to the manipulator was created and that the plane and polished part of the sample holder was firmly fixed to the copper block.

5. The electrical contact wires of the ITO film were connected to two interface lines at the manipulator that were controllable from outside of the chamber. The other 5 electrical contacts were connected to 5 interface lines at an interface flange leading outside of the chamber.

3.2.1 Measurement setup

All measured device current signals were collected and processed using a Heka PG 510 potentiostat (see figure 3.10) that allowed for the chemicurrent/thermocurrent detection. In this case, one platinum film contact was normally open (NO) and in a non-conductive state as the other was connected to a bridge or short circuit (as depicted in figure 3.10) between the reference electrode (RE) and the counter electrode (CE). The tantalum film contact was connected as working electrode (WE). With this setup, electrons collected at the tantalum film (WE) were read out as a positive current while electrons collected at the platinum film (CE) were read out as negative current. The potential between the electrodes was tunable, flowing currents and the voltage between the electrode were recorded. Alternatively, two platinum film contacts were connected: one to the bridge between RE and CE and the other as WE. By applying a constant voltage across and reading out the flowing current through the platinum film, the resistance of the film was measurable for resistance–temperature calibrations (see section 3.3.1). The tantalum contact was not connected and nor-

mally open (NO) during these measurements.

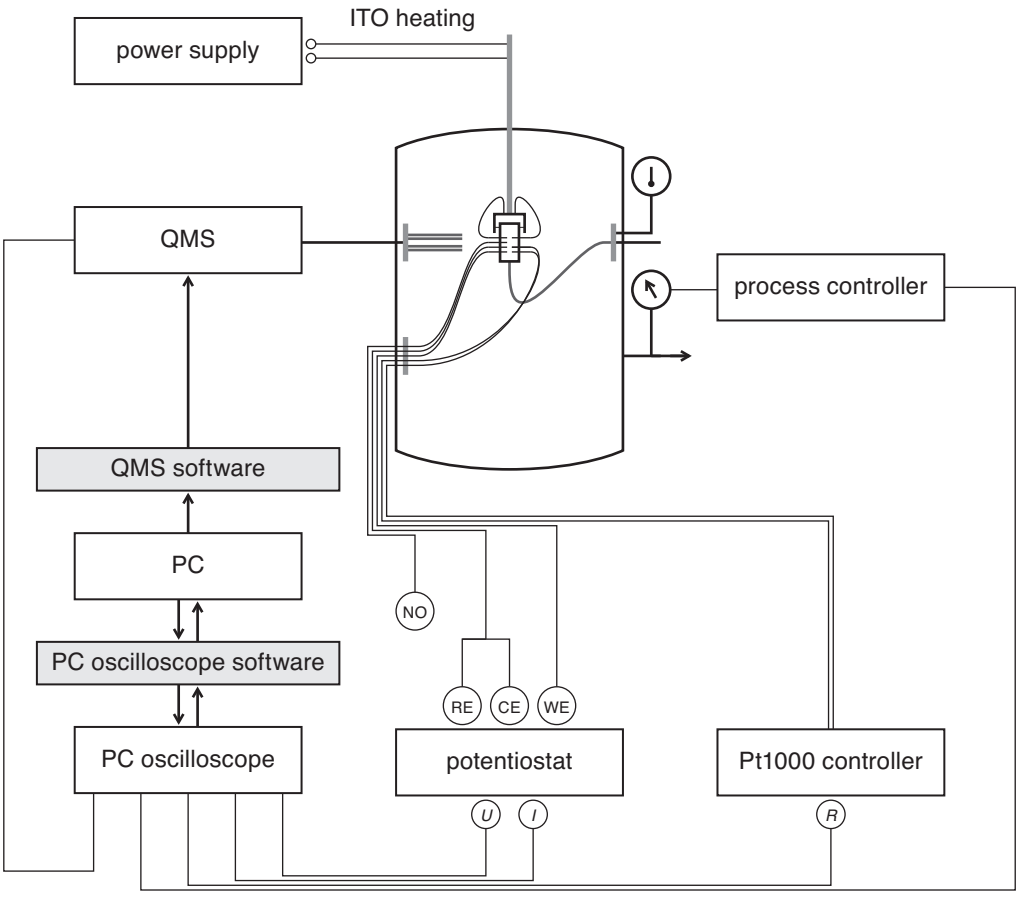

Figure 3.10: Measurement setup

The Satellite LM61 quadrupole mass analyzer was operated using an MKS Residual Gas Analyzer 4 software. The QMS signal was read out directly using a Bayonet Neill–Concelman (BNC) connector. This signal was electronically amplified with a gain of 10^{10} using a non-commercial amplifier powered by two 9 V batteries. The Pt1000 resistance–temperature sensor was operated by a modified non-commercial Pt1000 interface controller using a measurement current of 1 mA in order to prevent heating the sample area with the resistance–temperature sensor at temperatures below 70 K. The pressure measured with the Leybold Vacuum IONIVAC ITR 90 combination gauge that was controlled by the Leybold Vacuum COMBIVAC IT23 process controller was read out as a

voltage signal. All measurement signals were routed over BNC cables and were collected and recorded using a PicoScope 3425 PC oscilloscope and its software (PicoScope 6) using a personal computer operated by Microsoft Windows XP.

The indium tin oxide film was heated by passing currents of below 0.1 A through the film while applying voltages in the range of 4–10 V using a Delta Elektronika SM 120-25 D power supply.

3.3 Temperature measurement

Usually, thermal desorption experiments are carried out by means of external heaters—for instance tungsten filaments attached to the sample holder. Unfortunately, such macroscopic heating methods cause multiple desorption processes from the chemoelectronic device and from the sample holder as well. The re-cooling to adsorption temperatures proceeds slowly as well. In any case, a macroscopic heater heats more parts of the experimental setup than necessary. [69] Thus, a tailored heating method that provides activation energies for desorption processes selectively for surface reactions and surface dynamics on the top metal electrode of chemoelectronic devices was developed: the method of backside heating by passing currents through thin metal or semiconductive films deposited on the backside of the nanodevice substrate. [96, 69] Heating the sample and not the sample holder leads to perceptible temperature gradients. Furthermore, cooling and heating the samples at the same time is expected to result in lateral temperature gradients on the sample holder and on the sample as well. Also vertical temperature gradient should be considered. Therefore, accurate and non-interfering temperature measurements are required that are suitable for such nanodevices.

3.3.1 Pt resistance–temperature measurement

Resistance thermometers such as the used Pt1000 resistance–temperature sensors allow for an accurate temperature measurement of a metal by measuring its resistance. The principle of the measurement is based on the temperature dependence of the resistance of a given metal. With increasing temperature

in the metal the amplitudes of the thermodynamic vibrations of its atomic nuclei increase. Simultaneously, the probability of collisions between its free electrons and bound ions undergo corresponding increases. As a result of these interruptions of the free motion of the electrons due to electron–atom collisions the resistance of the metal increases. Pure metals are typically used because they guarantee perfect reproducibility and easy standardization. Platinum is most commonly used because it is highly stable, corrosion resistant, and applicable at temperatures between 13.80 K and 1234.93 K in neutral atmospheres. [97, 98, 69, 99]

The resistance of a given metal can be monitored for instance while an applied voltage U across the metal is held constant and the current I that flows through is measured as Ohm's law states:

$$R = \frac{U}{I} \tag{3.1}$$

In turn, a constant current can also be passed through the metal while the voltage drop at the metal is measured. Despite the fact, that the resistance of platinum increases almost linearly with temperature over a wide range, curve fitting is required in order to convert the measured resistance accurately to temperature. The temperature of a Pt1000 resistance–temperature sensor is calculated with the use of the Callendar–van Dusen equation which expresses the non-linearity of the temperature dependence of the resistance for platinum resistance thermometers. [100, 98, 99]:

$$R(T) = R_0\left(1 + AT + BT^2 + C(T - 100)T^3\right). \tag{3.2}$$

A Pt1000 resistance–temperature sensor has a resistance of $R_0 = 1000\,\Omega$ at $0\,^\circ\mathrm{C}$. A, B, and C are the Callendar–van Dusen coefficients and according to the International Temperature Scale ITS-90:

$$\begin{aligned} A &= 3.9848 \times 10^{-3}\,^\circ\mathrm{C}^{-1} \\ B &= -5.87 \times 10^{-7}\,^\circ\mathrm{C}^{-2} \\ C &= -4 \times 10^{-12}\,^\circ\mathrm{C}^{-4}. \end{aligned}$$

For temperatures above 0 °C the coefficient C equals 0 and the Callendar–van Dusen equation is reduced to a quadratic equation. For temperatures below 0 °C all three coefficients are taken into account. Although the Callendar–van Dusen equation was refined and replaced by interpolating formulas including higher order polynomials it is accurate enough for the purpose of this work and therefore used here. [101, 99]

Despite the accuracy of Pt1000 resistance–temperature sensors, their heat capacity is huge compared to the electrodes of the chemoelectronic nanodiodes due to their macroscopic volume. Thus, a mounted Pt1000 resistance–temperature sensor would act as dominant heat sink while the thin film structure is heated by passing a current through it. Also the electrical contacts of the nanodiode are heat sinks and during heating a temperature profile establishes that typically looks like the profile depicted in figure 3.11. [69]

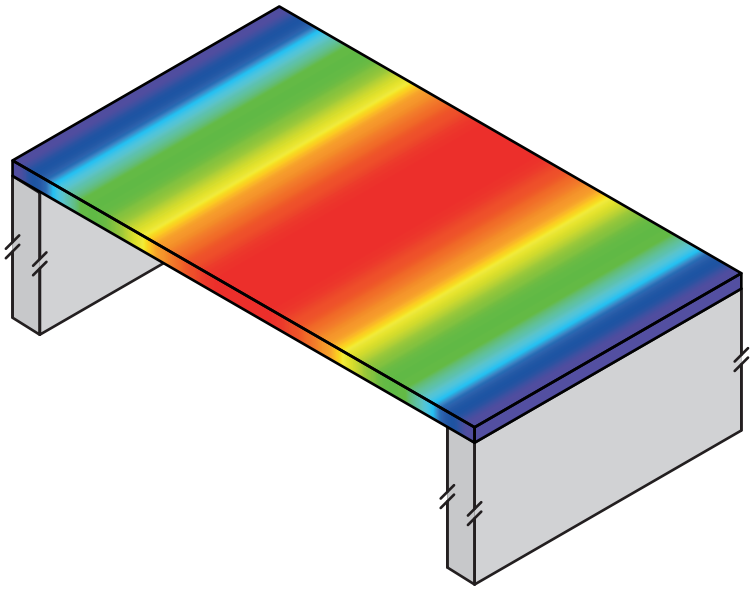

Figure 3.11: Assumed visualization of the temperature profile in a nanofilm that is electrically connected with macroscopic contacts (gray) and heated by passing a current through it

In order to avoid a direct contact of a Pt1000 resistance–temperature sensor with the heated nanostructure a direct temperature measurement of the heated top platinum electrode is feasible by measuring its resistance. [102, 69]

For this purpose, the two electrical contacts at the edges of the platinum film were connected to the Heka PG 510 potentiostat. One contact was connected to the bridge between the counter electrode and the reference electrode and the other was connected as working electrode. An applied potential U was held constant while a current I was passed through the Pt film and monitored. The resistance of the Pt film was calculated using equation 3.1. In order to assign a temperature to the measured resistance, a calibration was carried out by measuring the resistance of the platinum film while the temperature of the sample holder was measured for several minutes after a constant temperature level was established in the range of 70–320 K. For this calibration the Pt1000 resistance–temperature sensor glued onto the sample holder like the sample itself was used to monitor the temperature. No temperature gradients on the sample holder were expected here as the system was given sufficient time to establish a homogeneously constant temperature while slow macroscopic cooling by means of the He cryostat and heating with halogen lamps inside the vacuum chamber were carried out. A plot of the monitored resistance of the platinum film against the temperature monitored with the Pt1000 resistance–temperature sensor showed an approximately linear dependence over the entire temperature range and a linear regression was performed as:

$$R(T) = a + bT\,. \tag{3.3}$$

The temperature in turn was therewith calculated as:

$$T = \frac{(R(T) - a)}{b}\,. \tag{3.4}$$

For established constant temperatures this method is accurate. However, in the case of rapid heating events non-uniform lateral temperature gradients result. The assigned temperature is a mean temperature over the length between the two electrical contacts, because the mean resistance of the Pt film over that length is measured here. Due to the heat transfer into the electrical contacts the measured temperature is significantly lower than the temperature at the center of the Pt film where the actual nanodiode is located. Especially this tempera-

ture at the center is of interest as the temperature dependence of chemicurrents or thermocurrents is desired to be clarified.

While the potential between the top platinum electrode and the bottom tantalum electrode of the chemoelectronic nanodiode was varied, it was observed that temperature changes of the nanostructure resulted in changes of the monitored current. This temperature dependence was utilized to develop a new method of temperature measurement of the nanodiode that is described within the following subsection.

3.3.2 MIM current–voltage temperature measurement

In order to check the insulating character of the Ta_2O_5 interstitial barrier of the prepared chemoelectronic nanodiodes, current–voltage characteristics (tunneling curves) were recorded at normal temperature (see figures 3.12 and 3.13). As already discussed, the MIM structure can be interpreted as a parallel-plate capacitor. The capacitance C of this capacitor can be determined from the capacitive charging current I_C at $U = 0\,\mathrm{V}$ in the current–voltage characteristics. In the case of a scan rate of $r_{scan} = {}^{dU}/_{dt} = 20\,\mathrm{mV\,s^{-1}}$ the capacitive charging current observed for MIM sample JPM 3.02 was $I_C = 17.01\,\mathrm{nA}$ in the positive branch and $I_C = -16.96\,\mathrm{nA}$ in the negative branch. The capacitance was therewith:

$$C = \frac{{}^{dQ}/_{dt}}{{}^{dU}/_{dt}} \approx 0.85\,\mu\mathrm{F}\,. \tag{3.5}$$

The slow scan signals (see figure 3.12) were processed using a bandwidth of 30 Hz, a current range of 1 µA, and a current filter of 10 Hz. Therewith, a current signal of 1 µA was transposed and read out as 10 V. An increase of the scan rate to $r_{scan} = 2\,\mathrm{V\,s^{-1}}$ resulted in an increase of the absolute value of the capacitive charging current to $I_C = 1.257\,\mu\mathrm{A}$ in the positive branch and $I_C = -1.298\,\mu\mathrm{A}$ in the negative branch. With these, the capacitance was calculated as:

$$C = \frac{{}^{dQ}/_{dt}}{{}^{dU}/_{dt}} \approx 0.64\,\mu\mathrm{F}\,. \tag{3.6}$$

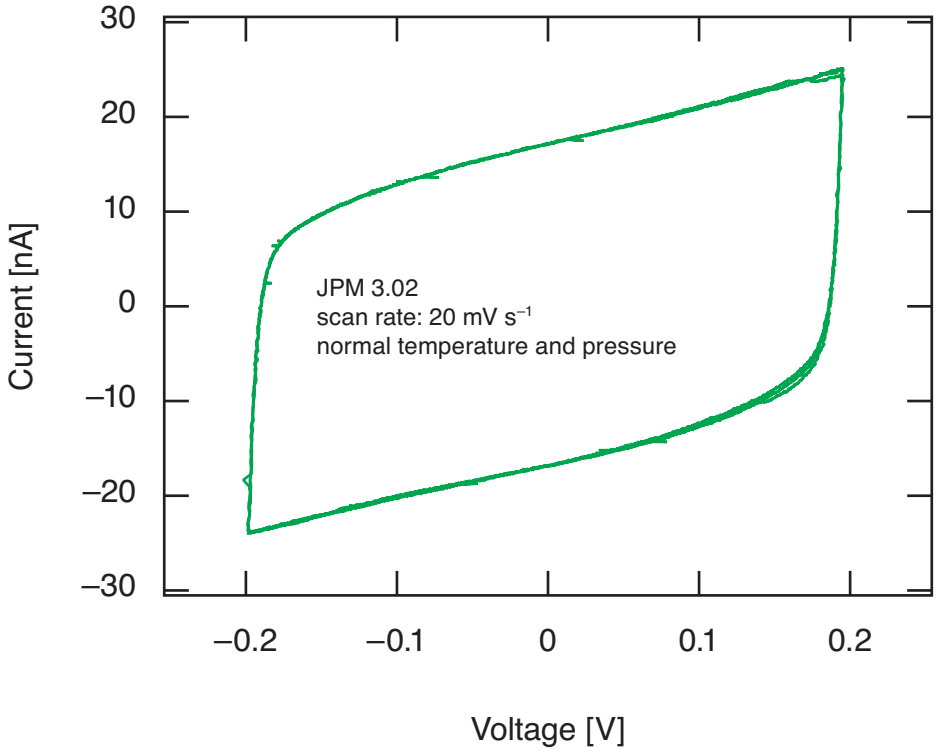

Figure 3.12: Current–voltage characteristics of MIM sample JPM 3.02 at normal temperature and pressure ($T \approx 293\,\mathrm{K}$, $p \approx 1013\,\mathrm{mbar}$)

The fast scan signals (see figure 3.13) were processed using a bandwidth of 100 Hz, a current range of 10 µA, and a current filter of 100 Hz. Both current–voltage characteristics were measured at normal temperature and pressure on the same day without any parameter changes except the potentiostat settings. The reason for this reproducible difference in capacitance was most probably a result of signal processing. Obviously, one should be aware of the parameter and measurement settings for the determination of the device capacitance. Furthermore, the recorded scan rate differed slightly from the set scan rate as well. However, for all following experiments the fast scan rate was used in order to achieve a quick response to changes in temperature or encircling gas.

In the course of experimental temperature variations it was observed that the current–voltage characteristics changed with temperature. For increasing sample temperatures the current shifted to higher absolute current values

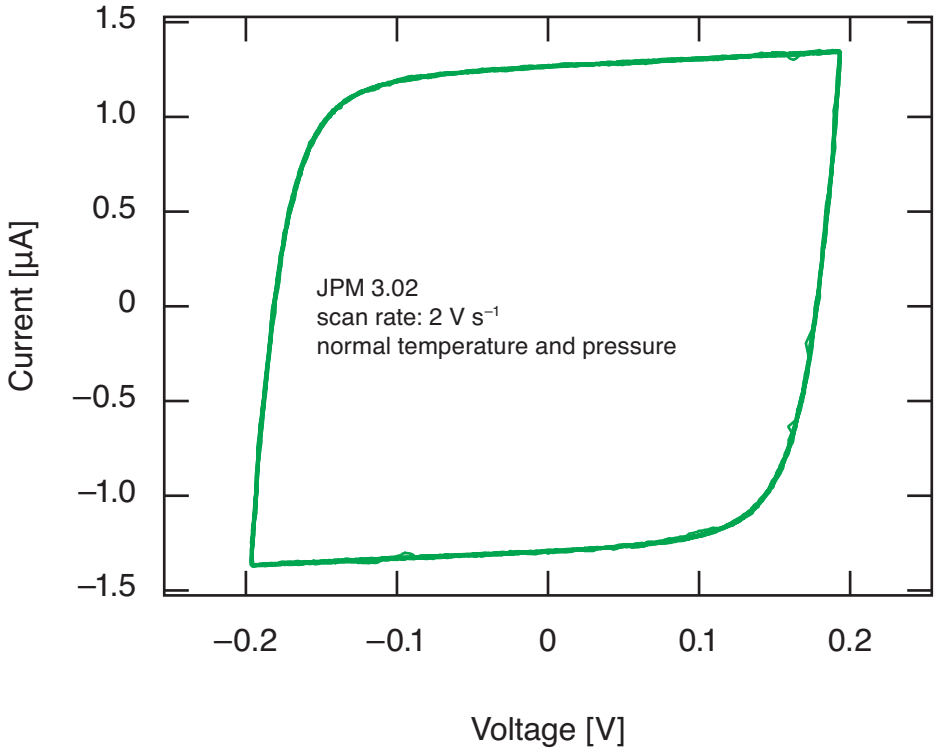

Figure 3.13: Current–voltage characteristics of MIM sample JPM 3.02 at normal temperature and pressure ($T \approx 293\,\mathrm{K}$, $p \approx 1013\,\mathrm{mbar}$)

while varying the voltage between $-0.2\,\mathrm{V}$ and $0.2\,\mathrm{V}$. Furthermore, it was observed that the rectangular shape of the current–voltage characteristics shifted to a parallelogram-like shape (see figures 3.15 and 3.16). A procedure was written to read out the current values at voltages in the range of 0.15–0.19 V in order to study the current–temperature dependence. For different constant temperatures current–voltage characteristics were recorded and the current values were read out. The constant temperatures were established by using the He cryostat and the heating wires around (and outside of) the stainless steel vessel (normally used in order to bake the chamber) for cooling and heating simultaneously. All light sources (halogen lamps and filaments) inside the chamber were switched off in order to prevent the increase of the device current signal due to photocurrents. The system was given sufficient time to reach the constant temperatures and temperature gradients were no longer expected, neither

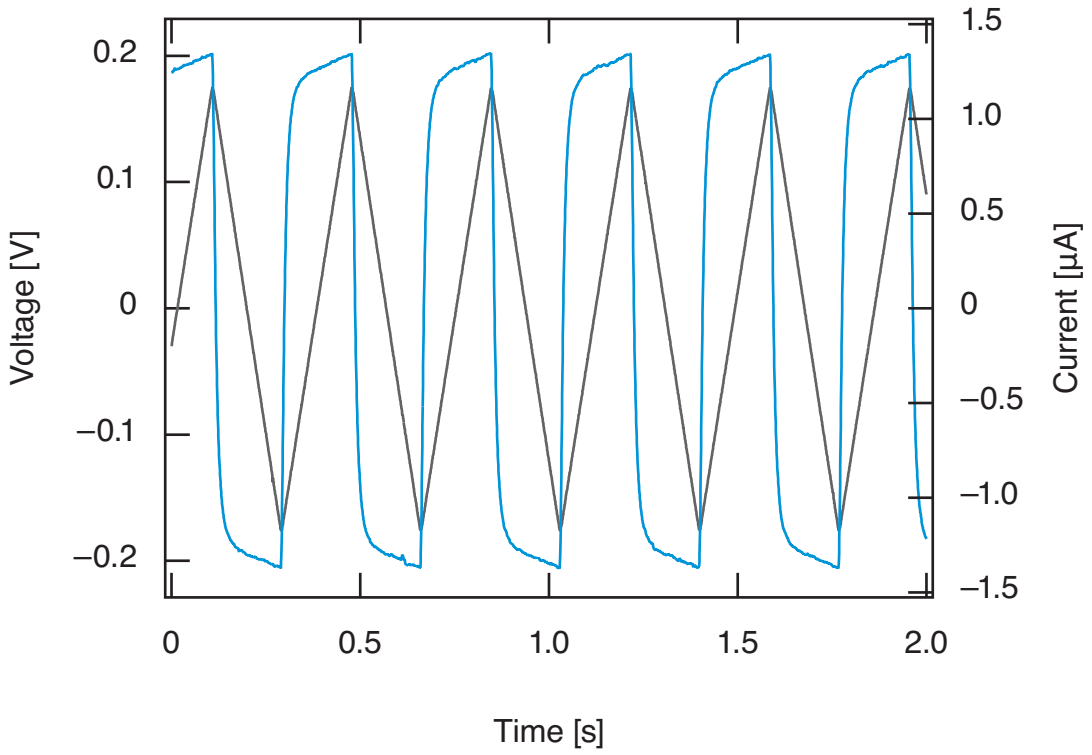

Figure 3.14: Applied triangular voltage variation (gray) and the current answer (blue) of MIM sample JPM 3.02 using a scan rate of $r_{\text{scan}} = 2\,\text{V}\,\text{s}^{-1}$ at normal temperature and pressure ($T \approx 293\,\text{K}$, $p \approx 1013\,\text{mbar}$)

on the sample holder nor on the sample itself. Thus, these equilibrium temperatures were measured accurately with the Pt1000 resistance–temperature sensor glued on the sample holder adjacent to the sample. The mean values of the extracted current values were plotted against the established equilibrium temperatures and an exponential increase with temperature was observed (see figure 3.17).

This exponential dependence can be rationalized as the already discussed thermionic emission current density J that increases exponentially with temperature as well. The thermionic emission current density is not only a function of temperature but also a function of the applied voltage U between the two electrodes (or plane capacitor plates). The observed current increase is describable as a voltage assisted thermionic emission and the current density can

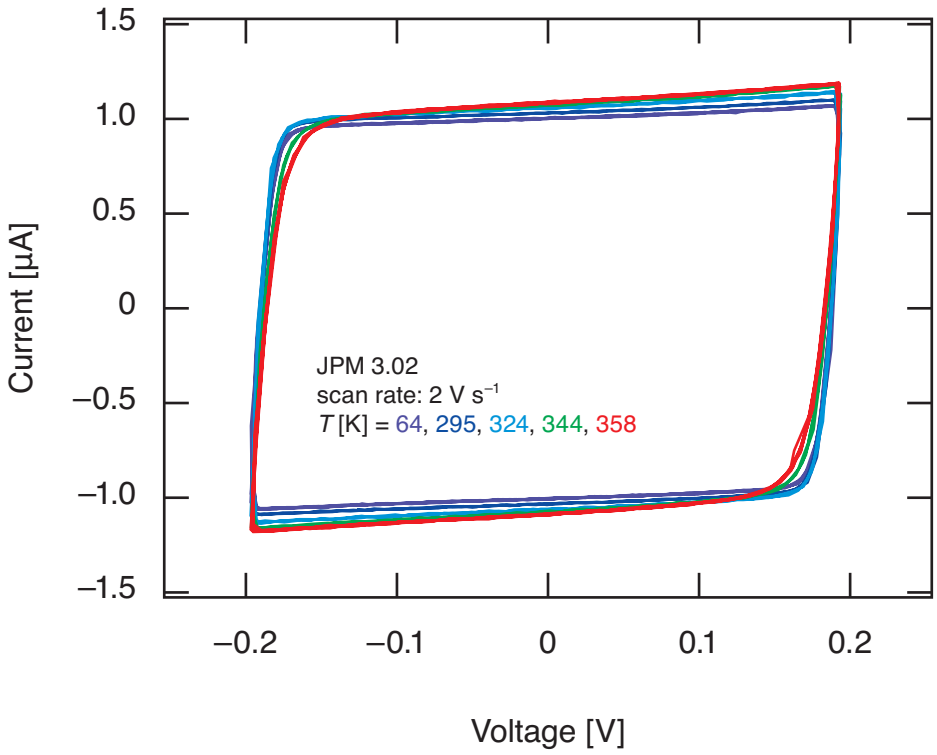

Figure 3.15: Current–voltage characteristics of MIM sample JPM 3.02 using a scan rate of $r_{\text{scan}} = 2\,\text{V}\,\text{s}^{-1}$ at different equilibrium temperatures under UHV condition ($p \approx 1 \times 10^{-10}\,\text{mbar}$)

be described as $J(T, U)$. As the mean current values are read out periodically for applied voltages between 0.15 V and 0.19 V, also the voltage can be seen as constant and $J(T, U)$ becomes $J(T; U)$. A power function in order to fit the observed I–T relation was drawn up as:

$$I = 1.0575 + 3 \times 10^{-10} T^{3.33}\,. \tag{3.7}$$

Using this power function, recorded current signals could be attributed to a certain temperature. Scanning the voltage again between $-0.2\,\text{V}$ and $0.2\,\text{V}$ also heating experiments were carried out. This time, temperature gradients on the sample holder and on the sample were expected, because the highly localized ITO backside heating was carried out (by applying for instance 8.5 V across the ITO film) while the sample holder was cooled simultaneously by

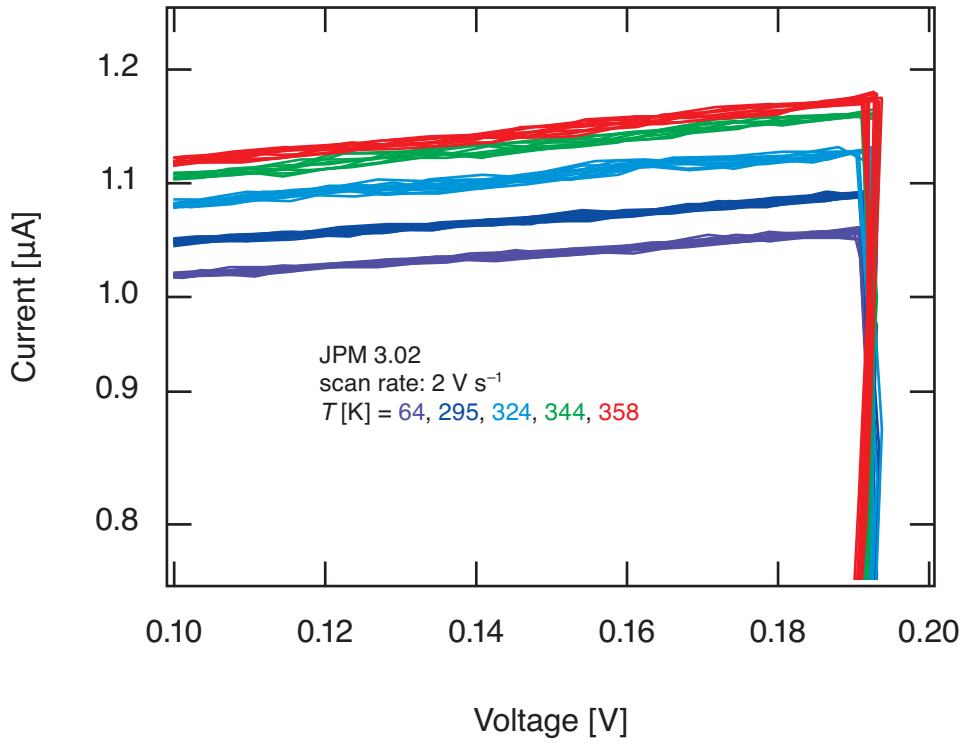

Figure 3.16: Enlarged section from figure 3.15

means of the He cryostat (see figure 3.18). The current values for applied voltages between 0.15 V and 0.19 V were extracted (see figure 3.19) and a double negative-exponential fit function of the current values was used. With the found I–T relation given by equation 3.7 this current increase was assigned to a temperature as:

$$T = \left(3 \times 10^{10}(I - 1.0575)\right)^{1/3.33}. \tag{3.8}$$

For an ITO backside heating of the sample with 8.5 V across the ITO film a rapid temperature increase was measured starting from the minimum temperature $T_{\text{min}} = 66\,\text{K}$ (see figure 3.20). Compared to the recorded temperature increase during a similar heating experiment (8.5 V across the ITO film, $T_{\text{min}} = 66\,\text{K}$) measured by the resistance–temperature measurement using the platinum film, the temperature measured using the device current increased much faster and reached a higher temperature after $t = 50\,\text{s}$. This can be ex-

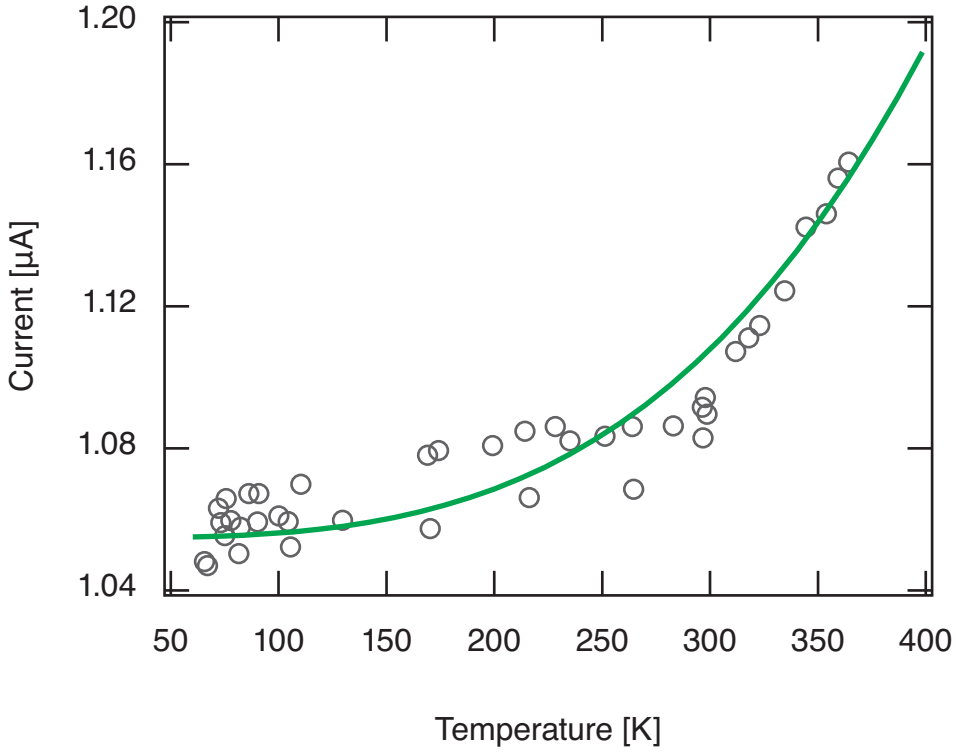

Figure 3.17: Mean current values in the voltage range of 0.15–0.19 V plotted against the equilibrium temperature

plained by the fact that the sample center reached a higher temperature compared to the surrounding areas as a result of the expected temperature profile (see figure 3.11). The mounted Pt1000 resistance–temperature sensor directly attached to the sample on the sample holder detected nearly no temperature increase at all. This underlines the exclusively local character of the developed backside heating method.

In any case, the developed method of temperature measurement enables the measurement of the actual temperature of the MIM chemoelectronic nanodiode volume at the center of the sample. Conveniently, no additional contacts are necessary and the same setup can be used that is mandatory for the detection of device currents in the course of studies of surface dynamics. All parameter changes are performed using the regular measurement setup and the measurement itself is performed in place by using the nanodiode. Thus, it

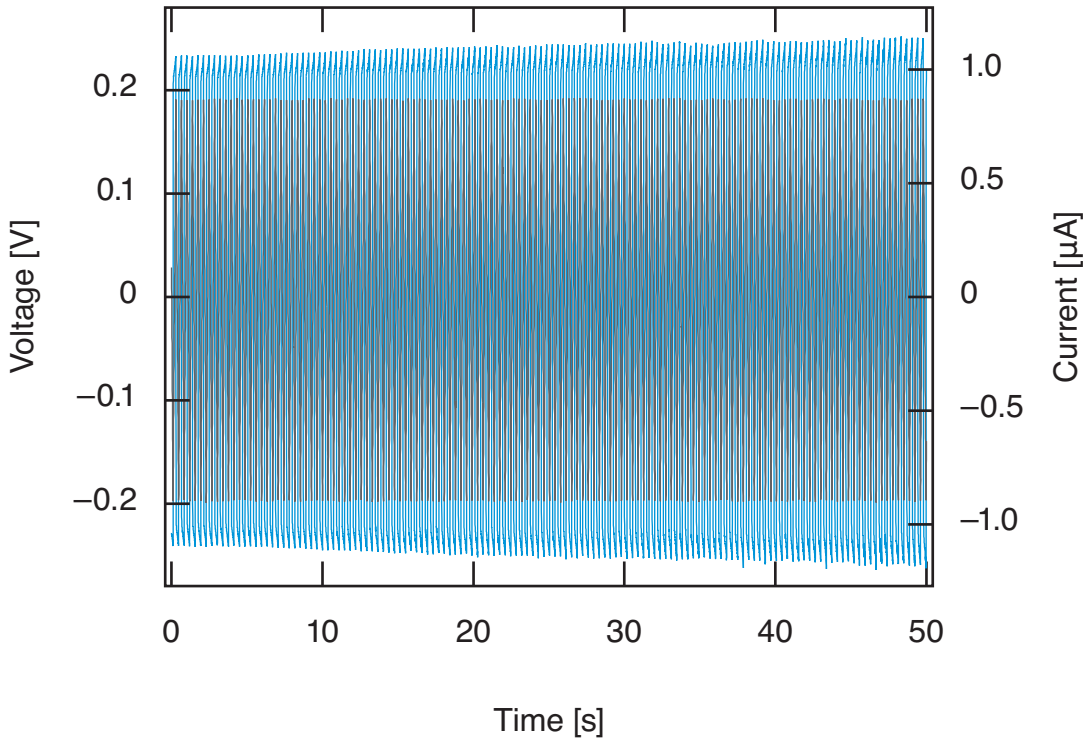

Figure 3.18: Sample heating: monitored voltage variation (gray) between $-0.2\,\mathrm{V}$ and $0.2\,\mathrm{V}$ and an increasing device current (blue) due to backside heating by applying $8.5\,\mathrm{V}$ across the ITO film after $t = 5\,\mathrm{s}$.

can be referred to as an *in-situ* temperature measurement.

However, for different samples different temperature dependencies of the device current were observed. Furthermore, the I–T dependence of one sample changed occasionally in the course of the experiments. Typically, after a cycle of temperature desorption experiments, switching off the He cooling system, and initiating the cooling again the baseline currents and the current values at the higher absolute voltage values changed. Therefore, the calibration procedure had to be repeated several times using the same sample (here: JPM 3.02).

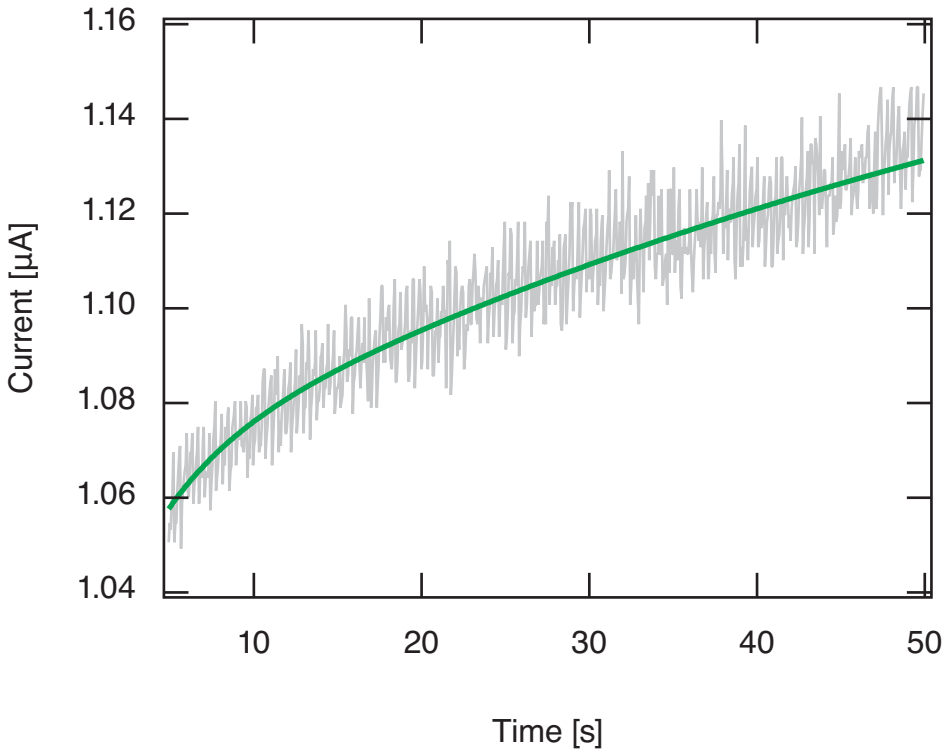

Figure 3.19: Sample heating: current values (light gray) of the positive current branch extracted at voltages between 0.15 V and 0.19 V and a fit of these current values (green) during heating by applying 8.5 V across the ITO film after $t = 5\,\mathrm{s}$.

3.4 MIM device current measurement

After calibrating the temperature measurement and assigning the correct temperature to heating experiments in the range of $\approx$ 60–400 K for different voltages across the ITO film in order to heat the sample, the potential between the platinum top electrode and the tantalum back electrode was no longer varied dynamically and held constant. Surface dynamics were studied, while similar heating experiments with determined temperature ramps were performed repetitively or while keeping the sample at constant temperatures. Simultaneously, the device current I was monitored. In a temperature range of $\approx$ 60–400 K and without backside ITO heating or ongoing surface dynamics on top of the platinum film the unbiased ($U_{\mathrm{bias}} = 0\,\mathrm{V}$) metal–insulator–metal system

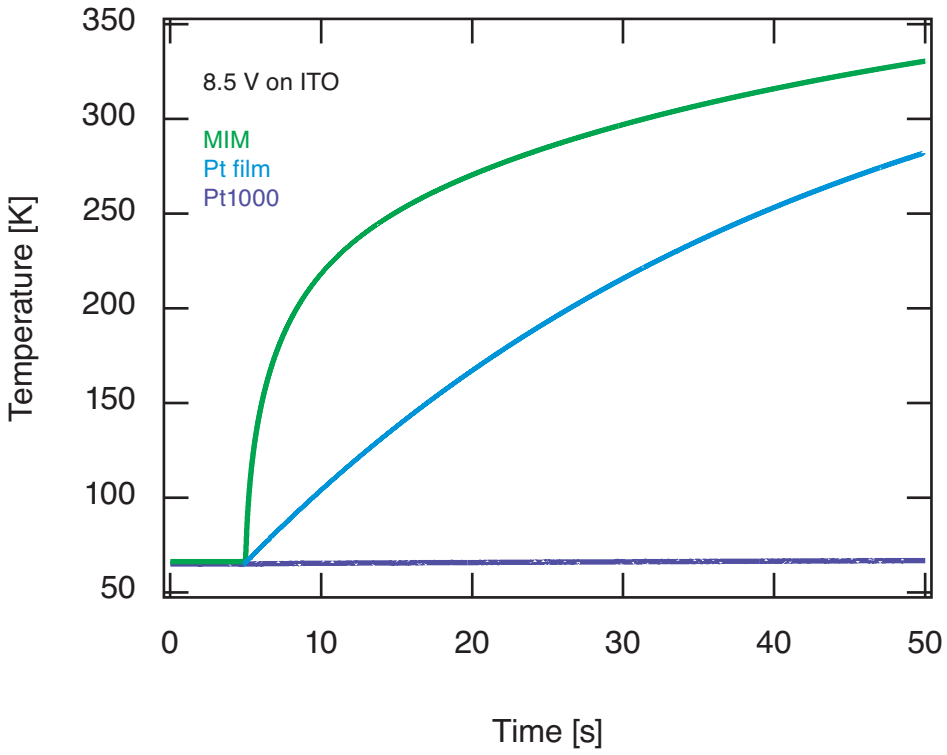

Figure 3.20: Measured temperatures during sample heating: temperature measurement using the device current (green), resistance–temperature measurement using the Pt film resistance (blue), and Pt1000 resistance–temperature detection (purple).

usually exhibited baseline currents I_0 between $-0.25\,\mathrm{nA}$ and $-0.05\,\mathrm{nA}$. This slight offset of the baseline to negative values was interpreted as a result of the signal processing—most likely due to the A/D conversion.

If the applied bias voltage was changed the current baseline shifted to more negative values for negative bias voltages and to more positive values for positive bias voltages (see figure 3.21). In measurements at equilibrated temperatures the device currents exhibited spikes to positive currents as a result of increased bias voltages and spikes to negative currents as a result of decreased bias voltages. These spikes (attributed to capacitive charging) decayed exponentially and a new baseline was established. The mean current value of each plateau was plotted against the applied bias voltage and linear isotherms were obtained that showed the non-linear temperature dependence of the voltage as-

sisted baseline current (see figure 3.22): the slopes of the isotherms increased exponentially with temperature. A leakage current through the oxide—driven by the applied bias voltage and facilitated by the increased temperature—could explain this behavior.

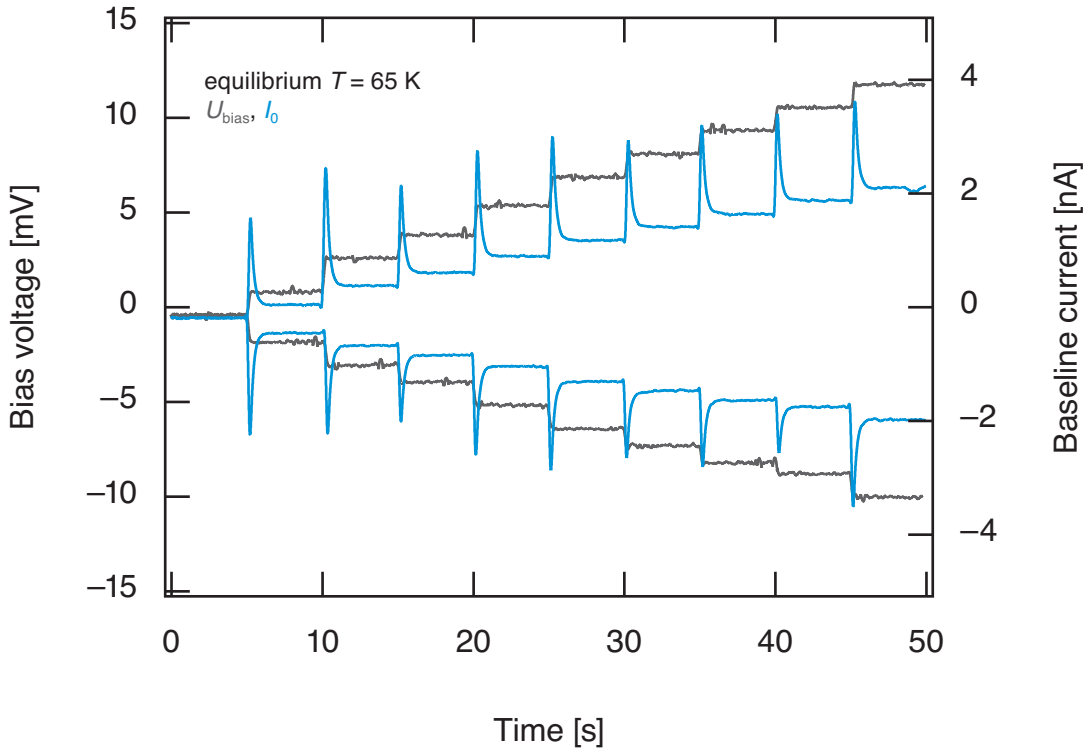

Figure 3.21: Baseline current shifts due to changing applied bias voltages at $T = 65\,\mathrm{K}$: spikes toward positive currents resulted with increasing bias voltages and spikes toward negative currents resulted with decreasing bias voltages. The current baseline shifted to more negative values for negative bias voltages and to more positive values for positive bias voltages.

Initiating the backside heating of the MIM system caused spikes in the detected baseline currents as well. These reproducible spikes were attributed to capacitive charging of a parallel-plate capacitor with the contacted MIM system (most likely the Pt top electrode) and the backside ITO film as separated capacitor plates. By applying a voltage across the ITO film the capacitor was charged and de-charged after switching off the voltage, respectively. As a result, spikes to negative current values for switching on and spikes toward positive current

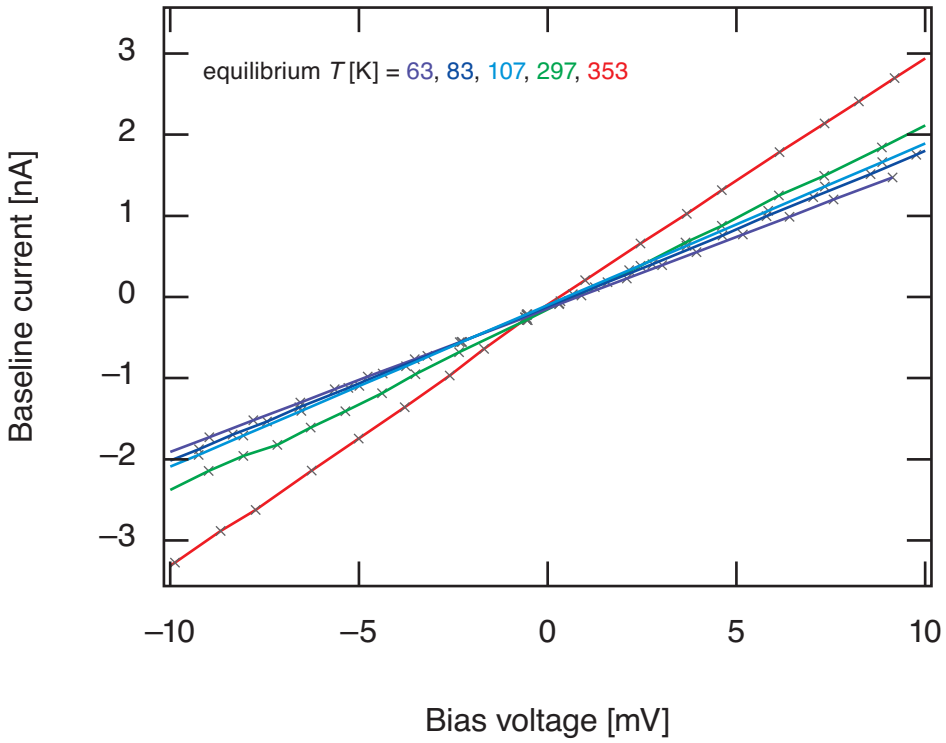

Figure 3.22: Baseline current isotherms measured for changed bias voltages U_{bias} between the MIM metal electrodes at different equilibrium temperatures

values for switching off the voltage across the ITO were observed. The magnitude of the spikes did not only scale with the applied voltage but also with the time between switching on and off. It was assumed that this increase of current signal was a result of the elevated temperature, because a more noisy current signal and a much slower relaxation of the current increase were observable as well for longer heating periods (see figure 3.23). It could be assumed that the potentiostat provided an electron flow toward the Pt top electrode in order to compensate for the positive charge in respect to the negatively charged ITO film. When the applied voltage across the ITO was switched off, electrons from the Pt electrode flowed back to the potentiostat—and additionally through the Ta_2O_5 as long as a certain temperature was exceeded. This could explain the temperature dependence of this charge/de-charge effect.

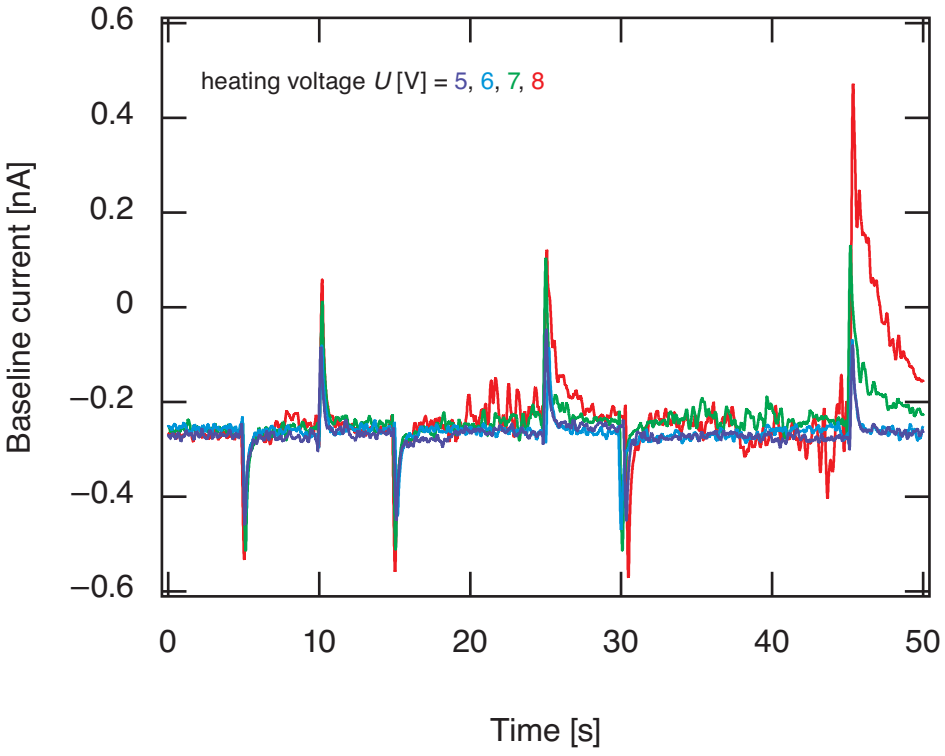

Figure 3.23: Effect of switching ITO heating on/off using different voltages

4 Results

In the course of adsorption and desorption experiments on the platinum surface of the MIM chemoelectronic nanodiodes positive and negative device currents were detected. Positive currents resulted either from hot charge carriers (predominantly hot electrons) tunneling through the Ta_2O_5 potential barrier or from surface potential changes of the platinum film (in this case a decrease in electron density) due to surface dynamics (bond formations and/or bond cleavages). The potentiostat compensated the decrease in electron density by providing an electron flow toward the platinum electrode in order to keep the bias voltage constantly at $U_{\text{bias}} = 0\,\text{V}$. Negative currents were detected if surface dynamics on the platinum film caused an increase of the electron density in the platinum film and the potentiostat provided an electron flow away from the platinum film in order to compensate for the resulting bias charge.

4.1 Adsorption and desorption experiments

Various gases and vapors of liquids were dosed onto the MIM system in order to investigate surface dynamics in the course of adsorption, dissociation, recombination, and/or desorption processes on the catalytically active platinum film. The device current was monitored while the voltage between the top platinum electrode and the bottom tantalum electrode of the MIM system was held constantly at $U_{\text{bias}} = 0\,\text{V}$. The temperature of the sample holder was monitored using the Pt1000 resistance–temperature sensor glued next to the sample onto the sample holder. The dosing pressures inside the main chamber were measured using the AML Bayard-Alpert ionization gauge.

4.1.1 TPD experiments

In order to conduct TPD experiments the sample was pre-cooled to adsorption temperatures of $\approx 65\,\mathrm{K}$ and cleaned subsequently by executing a first temperature ramp by applying favorably 0.5 V more across the ITO than in the following TPD experiments. Therewith, also molecules adsorbed on areas adjacent to the MIM surface were removed. Usually, a TPD experiment without dosing species ($D = 0\,\mathrm{L}$) was performed at first. Then, TPD experiments with increasing dosages were performed. In order to rule out effects of the sequence of dosage variations, also cycles with similar dosages were occasionally repeated to gain reliable results.

4.1.1.1 H_2O

At $\approx 65\,\mathrm{K}$ the vapor of ultra-pure water (purified using a Merck Millipore Simplicity water purification system) was dosed from a glass vial through a leak valve into the UHV chamber where it adsorbed on the Pt top electrode of the used MIM device. Simultaneously, the device current was monitored. Dosages between 10–35 L caused rapid increases of the device current up to $\approx 2\,\mathrm{nA}$ that decreased exponentially again (exponential decay), while the pressure inside the chamber was held constant (see figure 4.1). For small dosages below 2 L a small current increase was observed that was nearly constant until the first monolayer was established. Therefore, it could be assumed that the exponential decrease was related to the increasing surface coverage. Pressures up to $5 \times 10^{-6}\,\mathrm{mbar}$ were reached during dosing. It was observed that closing the leak valve in order to stop dosing resulted in an increase of the device current. This increase scaled with the dosage as well. For small dosages below 2 L this increase with closing the valve was not observable. Also the current peaks due to closing the valve decreased exponentially.

By applying a voltage of 8.5 V across the ITO backside film the sample was heated locally and temperature desorption spectra were recorded. For this purpose, the cooled sample covered with adsorbed H_2O was rotated such that its surface was close (2–3 cm) to the ionization region of the quadrupole mass analyzer prior to the heating. Desorbing molecules or fragments of molecules

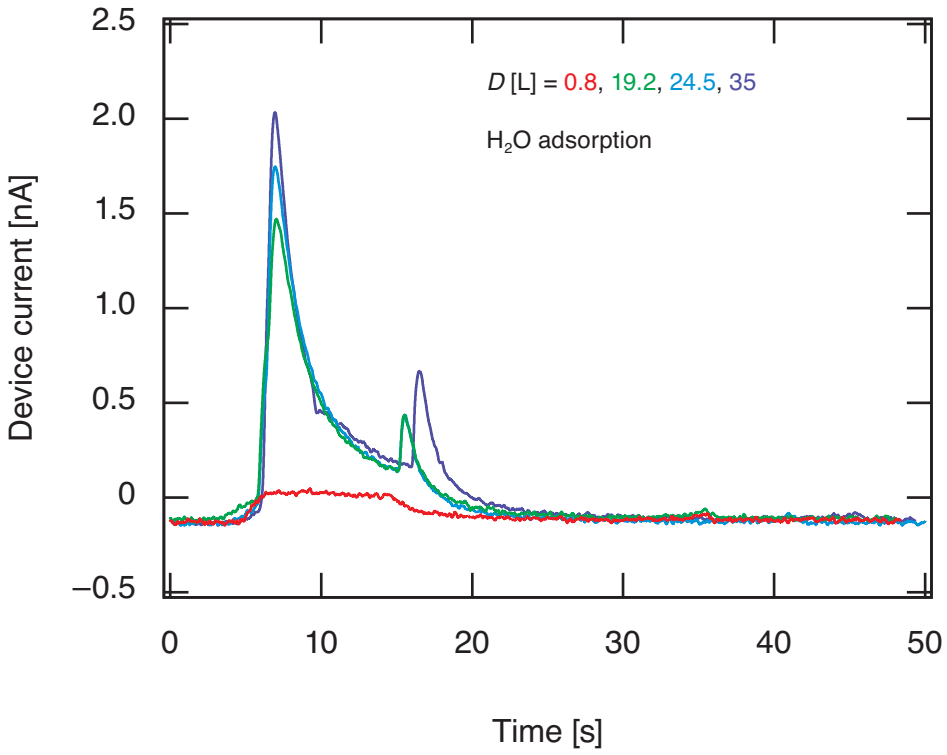

Figure 4.1: Response of the MIM device current to H_2O adsorption onto the Pt top electrode: at $t \approx 5\,s$ the leak valve was opened, at $t \approx 14$–$16\,s$ the valve was closed again.

were ionized using an ion source voltage of 68.7 V and mass 18 u was detected. A multiplier voltage of 1.4 kV was used. Between each TPD experiment and the next dosing of H_2O vapor, the sample was allowed to cool for 5 min. The sample holder, that was constantly cooled by the He cryostat, served as heat sink. Another 5 min were spent after each adsorption cycle and to pump not adsorbed H_2O vapor and in order to reach pressures of $\approx 2 \times 10^{-10}$ mbar again. A non-linear heating rate of $\approx 44\,K\,s^{-1}$ in the first 5 s and $\approx 1.5\,K\,s^{-1}$ over the last 20 s was used for the thermal desorption experiments according to to the performed temperature measurement. In good agreement with TPD spectra for H_2O desorbing from crystalline platinum surfaces, desorption peaks (α and β) at temperatures of $\approx 155\,K$ and $\approx 190\,K$ were observed. Whereas the low temperature peak associated with multilayer desorption was more dominant in

the obtained spectra, the monolayer peak (or peaks for different surface sites) was much more extended but identifiable (see figure 4.2). The fact that the features were less defined and chronologically dissolved was not unexpected due to the polycrystalline property of the Pt film and due to temperature gradients on the entire Pt film.

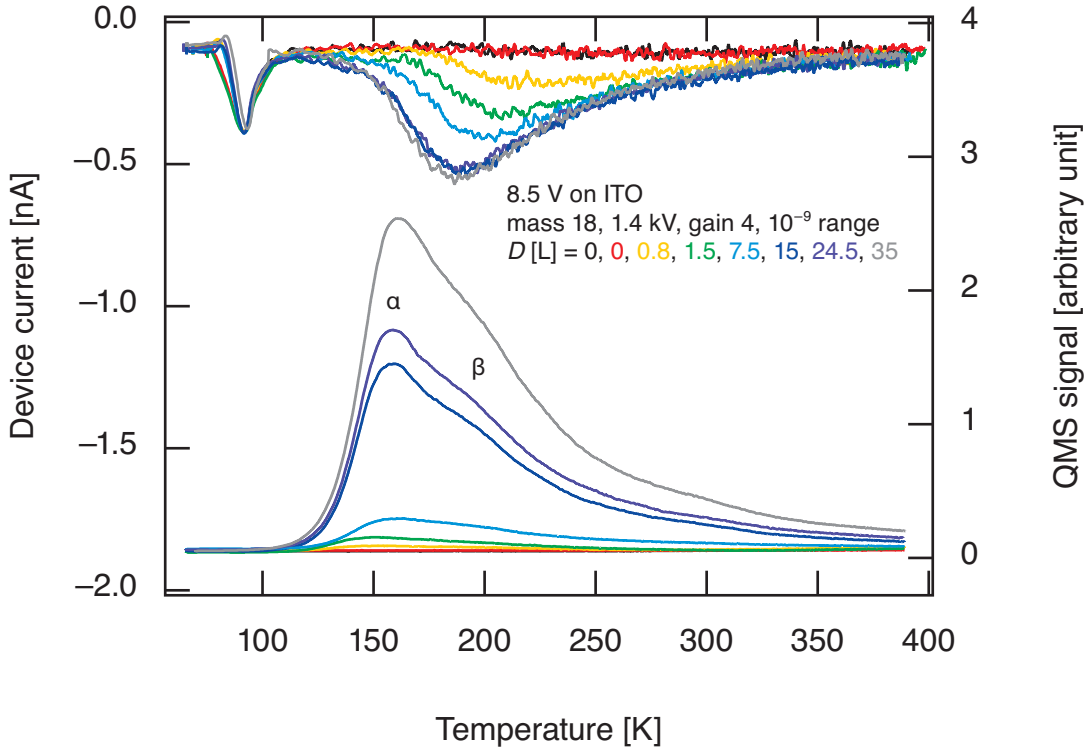

Figure 4.2: TPD spectra of H_2O from the Pt top electrode of the MIM device recorded at mass 18 u (bottom) and the simultaneously monitored device currents (top)

During the thermal desorption experiments the device current was monitored. The typical switching-on-spike was observed after initiating the ITO heating at $t = 5\,\mathrm{s}$. For TPD experiments without desorption of H_2O molecules ($D = 0\,\mathrm{L}$) the device current remained constant on the baseline, but with increasing dosage a dip in the device current was observed that scaled with dosage up to certain limit. After increasing dosages above that limit the dip remained constant. Furthermore, it was observed that the minimum of the resulting dip shifted with increasing dosage to lower temperatures (or earlier

time). The spectra with the deepest dip exhibits this at $\approx 180\,\mathrm{K}$. This result suggests that the dips were related to the H_2O monolayer desorption from the Pt surface.

In order to substantiate this assumption the recorded device currents were integrated over time from $t = 0\,\mathrm{s}$ to $t = 50\,\mathrm{s}$ (corresponding to $T = 66\,\mathrm{K}$ to $T = 390\,\mathrm{K}$ in the TPD spectra) to obtain the charges Q_{des} that had flown during these desorption processes. The baseline current was subtracted and the calculated charges were multiplied with -1 in order to obtain positive charges. Also the positive device currents observed during adsorption were integrated over the time of adsorption from opening the leak valve to closing the leak valve again, in order to obtain the adsorption charges Q_{ads}. Again, the baseline current was subtracted. As already recognized by studying the device currents during desorption, the absolute values of the charges for both sorption processes scaled with dosage up to a certain limit and reached a saturation plateau. This was clearly recognizable by plotting the calculated charges against the corresponding dosages (see figure 4.3).
In contrast, the integrated QMS signals scaled linearly with dosage and followed a line fit (green). Furthermore, desorption charges and adsorption charges could be fitted with the same double negative exponential function (purple). This underlined the reversibility of the measured sorption charges. A saturation in resulting charges for $D \approx 3$–$4\,\mathrm{L}$ was observed. This effect could be interpreted as a result of the formation of water–hydroxy mixed phases on the Pt surface. Especially, because the observed desorption peak temperatures for submonolayer and monolayer H_2O were slightly higher compared to TPD experiments from bare platinum crystals, and because the TPD curves were in good agreement with H_2O TPD spectra from platinum surfaces with preadsorbed oxygen. As already discussed, the presence of atomic oxygen on the Pt surface enabled the formation of more stable water–hydroxy mixed phases. Due to the fact that the used MIM samples were exposed to air during preparation and mounting, oxygen adsorbed and dissociated on the Pt surface. These atomic oxygen species remained adsorbed in the course of all UHV experiments because desorption would have required temperatures above $\approx 600\,\mathrm{K}$ and the maximum temperature of the platinum electrode that was reached

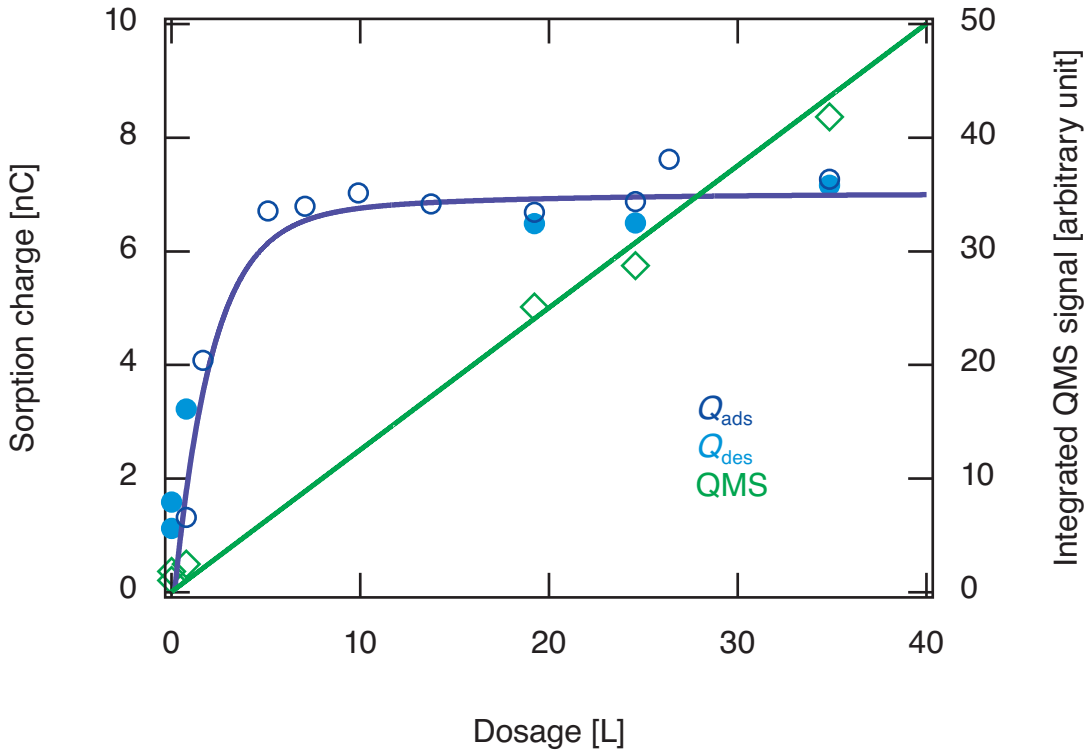

Figure 4.3: Absolute values of the H_2O adsorption charges Q_{ads} (dark blue) and the H_2O desorption charges Q_{des} (light blue) and the integrated QMS signals (green) plotted against the corresponding dosages D: the reversible charges due to adsorption and desorption processes reached a saturation at $D \approx 4\,\mathrm{L}$ whereas the integrated QMS signals scaled linearly with the dosage.

(even by intense heating), was still below $\approx 500\,\mathrm{K}$. In addition, temperatures above 500 K would have risked irreversible damages of the prepared thin-film devices.

It could be noted that besides temperature and voltage an additional driving force for charge transfer detected by the used MIM chemoelectronic nanodiodes was caused by surface dynamics—namely adsorption and desorption of water on the polycrystalline platinum top electrode. A slight shift of the desorption peaks to higher temperatures was also expected due to the huge initial heating rate (comparable to flash desorption experiments with rapid temperature ramps). In that case, the desorption rate was expected to be higher than the pumping speed of the vacuum system over a short period of time. Closer

to the end of the performed temperature ramp regular thermal desorption was expected and (re-)adsorption from the gas phase could be neglected as the pumping speed of the vacuum system was much higher than the desorption rate.

4.1.1.2 D_2O

The same adsorption and desorption experiments were carried out with D_2O as well. Again at $\approx 65\,K$, the vapor of D_2O (99.9 %, AR grade) was dosed from a glass vial through a leak valve into the UHV chamber where it adsorbed on the Pt top electrode of the used MIM device. Simultaneously, the device current was monitored. Dosages up to 54.7 L caused positive device current peaks analogous to the H_2O adsorption. Again, rapid increases of the device current up to $\approx 2.2\,nA$ occurred for high dosages and decreased exponentially (negative exponent) while the pressure inside the chamber was held constant (see figure 4.4). Small dosages below 2 L caused small current increases that were nearly constant until the first monolayer was established. Again, pressures up to 5×10^{-6} mbar were reached during dosing. In the process of dosing D_2O it was also observed that closing the leak valve caused an increase of the device current that scaled with the dosage and decreased exponentially (negative exponent). For small dosages up to 2 L this increase with closing the valve was not observable.

The D_2O thermal desorption experiments were performed analogously to the TPD experiments with H_2O. A voltage of 8.5 V was applied across the ITO backside film of the sample in order to heat the sample and temperature desorption spectra were recorded using the quadrupole mass analyzer. Desorbing molecules or fragments of molecules were ionized using an ion source voltage of 68.7 V and mass 20 u was detected. Between each TPD experiment and the next dosing of D_2O vapor the sample was cooled for 5 min and another 5 min were spent after each adsorption cycle in order to reach a base pressure of $\approx 2 \times 10^{-10}$ mbar again. The same non-linear temperature ramp was carried out as during the H_2O TPD experiments. The obtained thermal desorption spectra matched the obtained H_2O spectra (see figure 4.5). Mul-

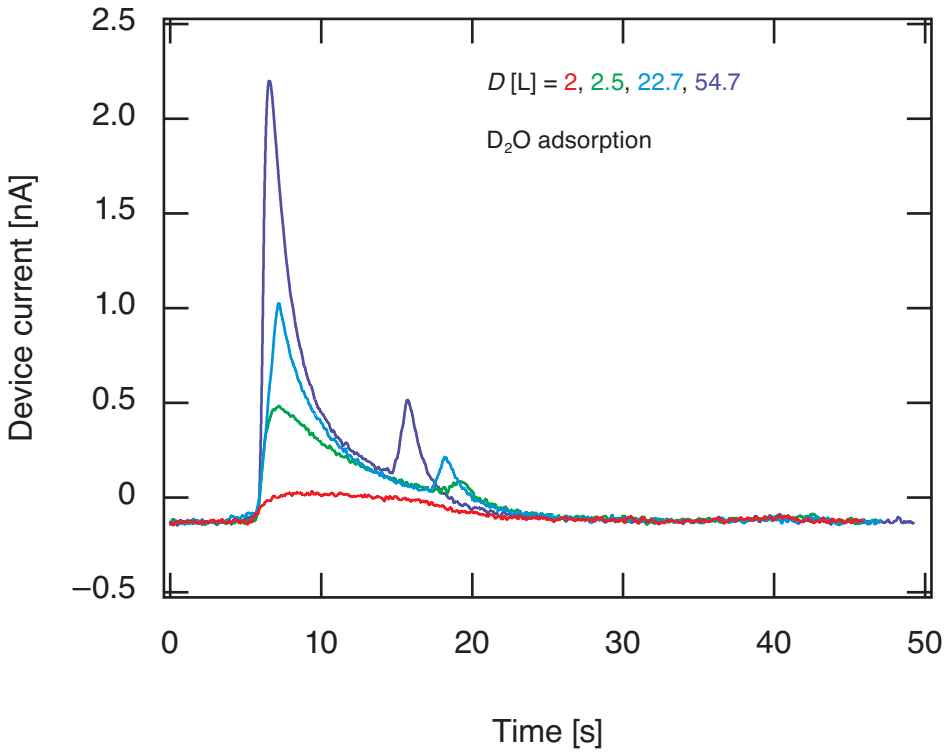

Figure 4.4: Response of the MIM device current to D_2O adsorption on the Pt top electrode: at $t \approx 5\,s$ the leak valve was opened, at $t \approx 14$–$18\,s$ the valve was closed again.

tilayer desorption (α) was attributed to desorption temperatures at $\approx 155\,K$ with a zero-order desorption kinetic. Various monolayer and submonolayer desorption peaks culminated in one desorption peak (β) at $\approx 190\,K$. The flux of desorbing fragments of mass 20 u decreased over a wide range and reached almost the initial at $\approx 380\,K$ even for high dosages. It could be assumed that an additional amount of dosed molecules desorbed later from surrounding areas and the edges of the Pt film that reached desorption temperatures delayed due to temperature gradients on the Pt film.

During the thermal desorption experiments the device current was monitored and the discussed spikes to negative current values with switching on the ITO heating after 5 s were observed again. For blank TPD experiments without dosages ($D = 0\,L$) the device current remained constantly on the base-

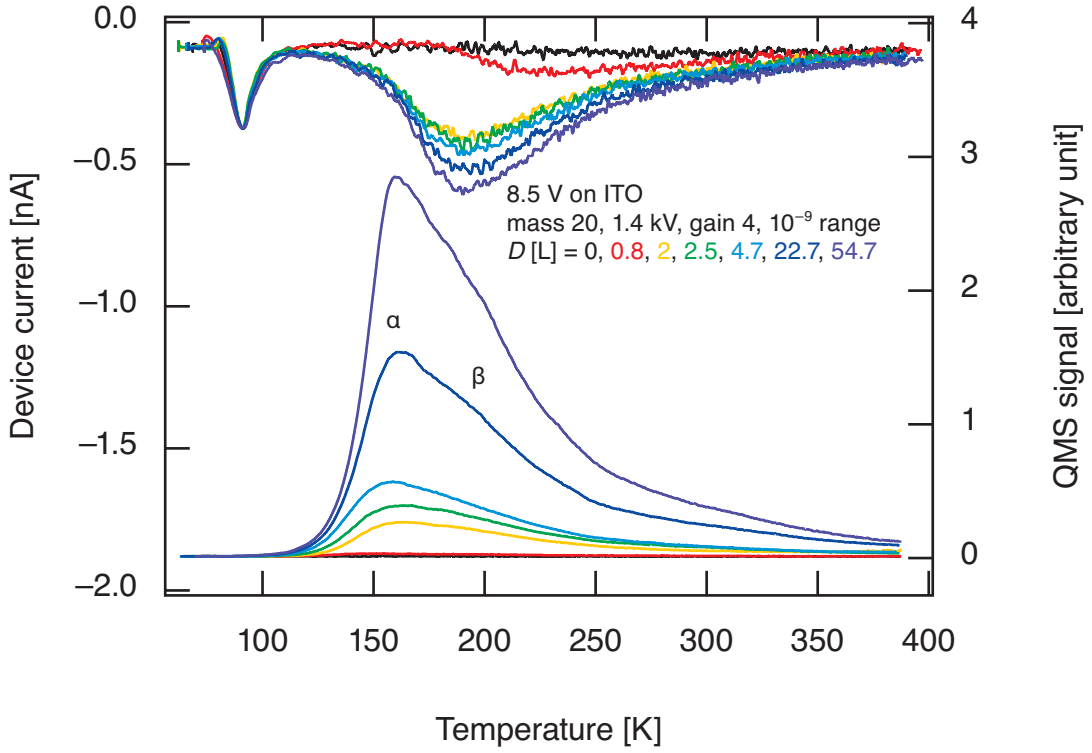

Figure 4.5: TPD spectra of D_2O from the Pt top electrode of the MIM device recorded at mass 20 u (bottom) and the simultaneously monitored device currents (top)

line. Increasing D_2O dosages caused dips in the device current that exhibited minima at $\approx 235\,K$ for submonolayer dosages and shifted to lower temperatures for higher dosages. For dosages around $D \approx 2$–$3\,L$ this shift stopped and constant minima temperatures of $\approx 180\,K$ were observed for higher exposures. A further increase of the dosages caused the device current dips to decrease, but also for D_2O a saturation plateau seemed to be established for dosages above 4 L.

The recorded desorption device currents were integrated over time from $t = 0\,s$ to $t = 50\,s$ (corresponding to $T = 66\,K$ to $T = 390\,K$ in the TPD spectra) to obtain the charges Q_{des} during these desorption processes. The baseline current was subtracted and the calculated charges were multiplied with -1 in order to obtain positive charges. Also the positive device currents observed during adsorption of D_2O were integrated over the time of adsorption in or-

der to obtain the adsorption charges Q_{ads}. Both sorption charges scaled with dosage up to a certain limit and reached a saturation plateau that is visualized in figure 4.6 by plotting the calculated charges against dosage. The same fit function as for the analysis of H_2O was suitable for the D_2O desorption and adsorption experiments as well: a double exponential function (purple). In contrast, the integrated QMS signals scaled linearly (green) with dosage. As expected, the sorption charges increased with dosage up to 4 L and reached a saturation for higher dosages.

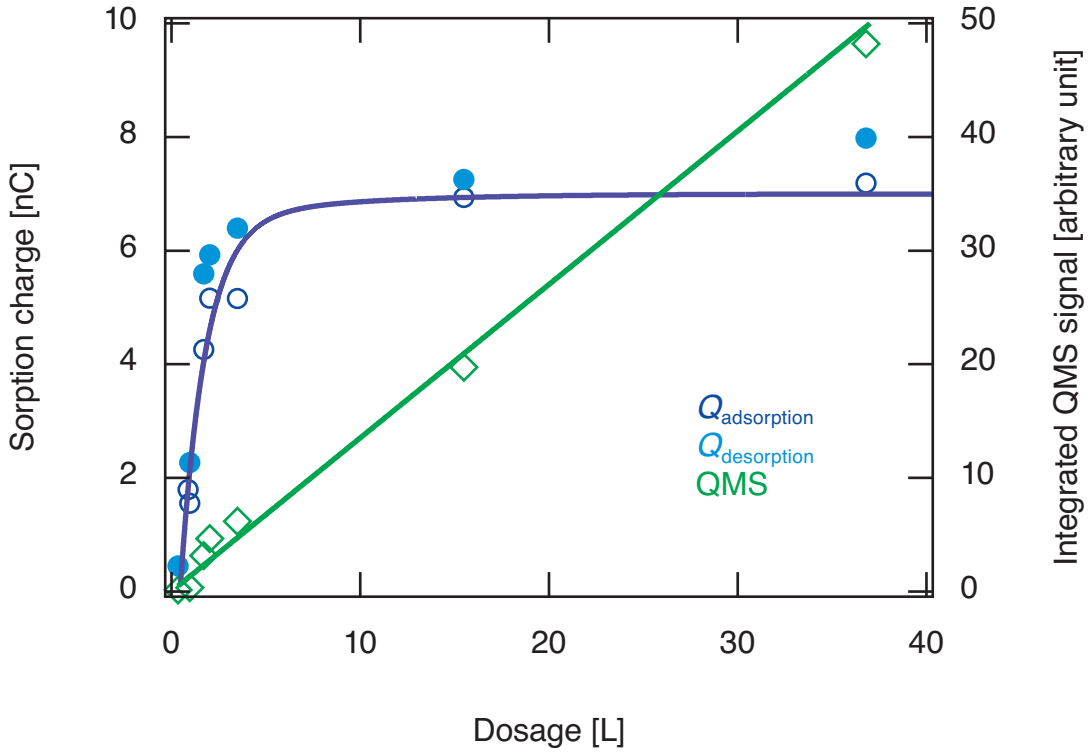

Figure 4.6: Absolute values of the D_2O adsorption charges Q_{ads} (dark blue) and the D_2O desorption charges Q_{des} (light blue) and the integrated QMS signals (green) plotted against the corresponding dosages D: the reversible charges due to adsorption and desorption processes reached a saturation at $D \approx 4$ L while the integrated QMS signals scaled linearly with the dosage.

Apart from proving the reversibility of the charging, the surface processes could be assigned to adiabatic effects because the observed charging processes for the H_2O and the D_2O experiments matched. In case of non-adiabatic ef-

fects, charge transfer processes involving H species would have been significantly enhanced compared to D species. Although the adsorption energies of the two isotopes are equal, the velocities during the single steps of the whole adsorption processes are different due to the mass difference. The faster H atom causes more likely non-adiabatic excitation processes than the slower D atom as the interaction (or friction) of the involved electronic structures is decisive to the non-adiabatic energy dissipation. [103] Furthermore, in case of tunnel currents no reversibility would be expected as the tunnel probability depends on the direction through the Ta_2O_5 potential barrier.

For further studies it could be interesting to dose also water with different oxygen isotopes (for instance ^{18}O) in order to prove the exchange of oxygen atoms within the water–hydroxy mixed phases on the platinum surface.

4.1.1.3 CH_3OH

Further TPD experiments were performed with alcohols in order to study the chemical specificity of the observed charging processes, because alcohols also form bonds with the Pt surface via the oxygen lone-pair of the hydroxy group and might contribute to hydrogen bonding networks.

At $\approx$ 65 K vapor of methanol (AR grade) was dosed from a glass vial through a leak valve into the UHV chamber where it adsorbed on the Pt top electrode of the used MIM device. Simultaneously, the device current was monitored. Analogous to H_2O and D_2O, the adsorption of CH_3OH caused positive device current peaks. Again, rapid increases of the device current were detected but even for huge dosages up to 85 L the current did not increase above $\approx$ 0.8 nA. Also these current peaks decreased exponentially (negative exponent) while the pressure inside the chamber was held constant and small dosages below 1 L caused small current increases that were nearly constant until the first monolayer was established. Even at pressures up to 1×10^{-5} mbar much smaller current peaks were observed for methanol adsorption compared to experiments with H_2O or D_2O. Again, a small increase in current with closing the leak valve was measured. Overall, the detected current signal changes were comparable to the adsorption experiments with H_2O and D_2O but much

smaller.

Analogously to the TPD experiments with H_2O and D_2O a voltage of 8.5 V was applied across the ITO backside film in order to heat the sample. Temperature desorption spectra were recorded using the quadrupole mass analyzer. Desorbing methanol or fragments of methanol were ionized using an ion source voltage of 68.7 V and mass 31 u was detected. Again, the sample was cooled for 5 min between each TPD experiment and the next dosing of CH_3OH vapor. Another 5 min were spent after each adsorption cycle in order to pump the vacuum system down to the base pressure of $\approx 2 \times 10^{-10}$ mbar. In good agreement with TPD spectra from crystalline platinum surfaces, two desorption peaks at temperatures of $\approx$ 155 K and $\approx$ 185 K were observed (see figure 4.7): a low temperature peak (α) associated with multilayer desorption and a high temperature peak (β) associated with desorption of chemisorbed methanol. Two additional broad features (γ and δ) for high dosages above 50 L were observed in the temperature range of $\approx$ 240–250 K and $\approx$ 280–320 K.

Again, the device current was monitored during the TPD experiments. With increasing dosages also for methanol desorption dips in the device current were observed. However, the device current decreases were much weaker than for comparable dosages in H_2O and D_2O desorption experiments. The observed dips exhibited minima at $\approx$ 250 K for submonolayer dosages that shifted to lower temperatures for higher dosages but stagnated at $\approx$ 220 K for dosages above $\approx$ 20 L.

Again, the recorded desorption device currents were integrated over time from $t = 0$ s to $t = 50$ s in order to obtain the desorption charges Q_{des}. Therefore, the baseline current was subtracted and the calculated charges were multiplied with -1 to obtain positive charges. Also the positive device currents observed during CH_3OH adsorption were integrated over the time of adsorption in order to obtain the adsorption charges Q_{ads}. Again a double negative-exponential fit function (purple) could describe the increase of the sorption charges with dosage and reaching the saturation plateau (see figure 4.8). As expected, the integrated QMS signals scaled linearly (green) with dosage. In the case of methanol the observed sorption charges increased moderately with dosage and the saturation plateau was reached at much higher

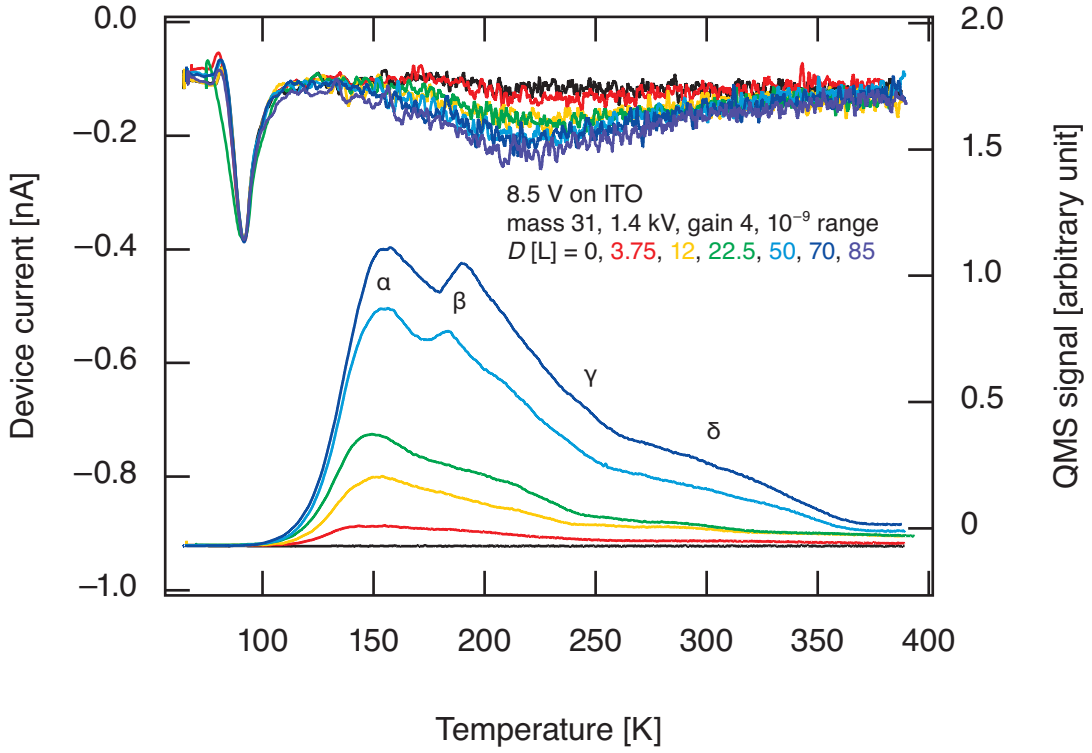

Figure 4.7: TPD spectra of CH_3OH from the Pt top electrode of the MIM device recorded at mass 31 u (bottom) and the simultaneously monitored device currents (top)

dosages ($D \approx 20$ L) compared to H_2O and D_2O.

Therewith, also the reversibility of adsorption and desorption processes for methanol on the Pt top electrode was proven. However, due to the faint device current changes in the course of adsorption and desorption the analysis in the case of methanol entailed a certain inaccuracy.

4.1.1.4 CH_3CH_2OH

Also vapor of ethanol (AR grade) was dosed from a glass vial into the UHV chamber onto the platinum top electrode at ≈ 65 K while the device current was monitored. Again, the device current increased due to the adsorption process—but much smaller in magnitude compared to methanol even at higher dosages. Furthermore, it was observed that the increased currents also de-

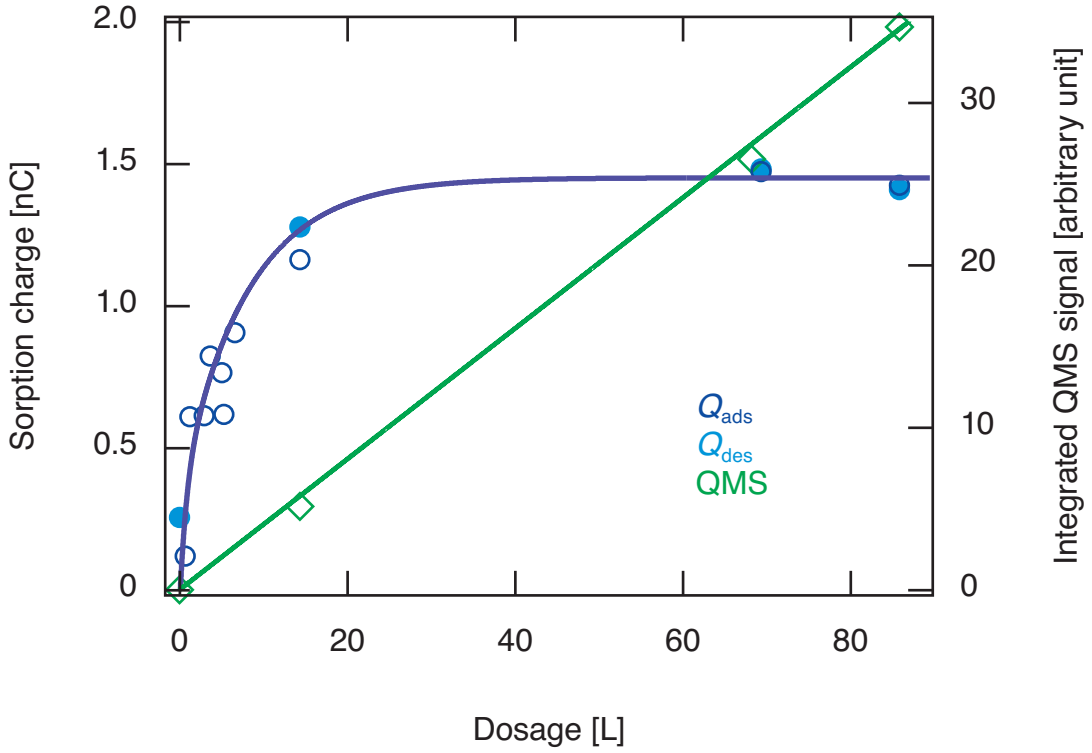

Figure 4.8: Absolute values of the CH_3OH adsorption charges Q_{ads} (dark blue) and the CH_3OH desorption charges Q_{des} (light blue) and the integrated QMS signals (green) plotted against the corresponding dosages D: the reversible charges due to adsorption and desorption processes reached a saturation at $D \approx 20\,\mathrm{L}$ while the integrated QMS signals scaled linearly with the dosage.

creased below the initial current baseline. Again, the current increased as a result of closing the leak valve and terminating the dosing process. After dosing, the initial baseline of the device current was established again.

TPD experiments were carried out by applying a voltage of 8.5 V across the ITO film in order to heat the sample. Desorbing ethanol or fragments of ethanol were ionized in the QMS ion source using a voltage of 68.7 V and mass 31 u was detected, because for ethanol the most dominant signal is expected for that mass.

Again, the sample was cooled 5 min before and 5 min after each TPD experiment in order to cool down for adsorption and reach the base pressure of $\approx 2 \times 10^{-10}$ mbar to start the next TPD cycle. In good agreement with ethanol

TPD spectra from crystalline platinum surfaces, two desorption peaks were observed: a low temperature peak (α) associated with multilayer desorption at ≈ 160 K and a high temperature peak (β) associated with monolayer desorption at ≈ 188 K (see figure 4.9). Two additional broad features (γ and δ) for high dosages above $D = 100$ L were observed in the temperature range of ≈ 240–250 K and ≈ 300–320 K.

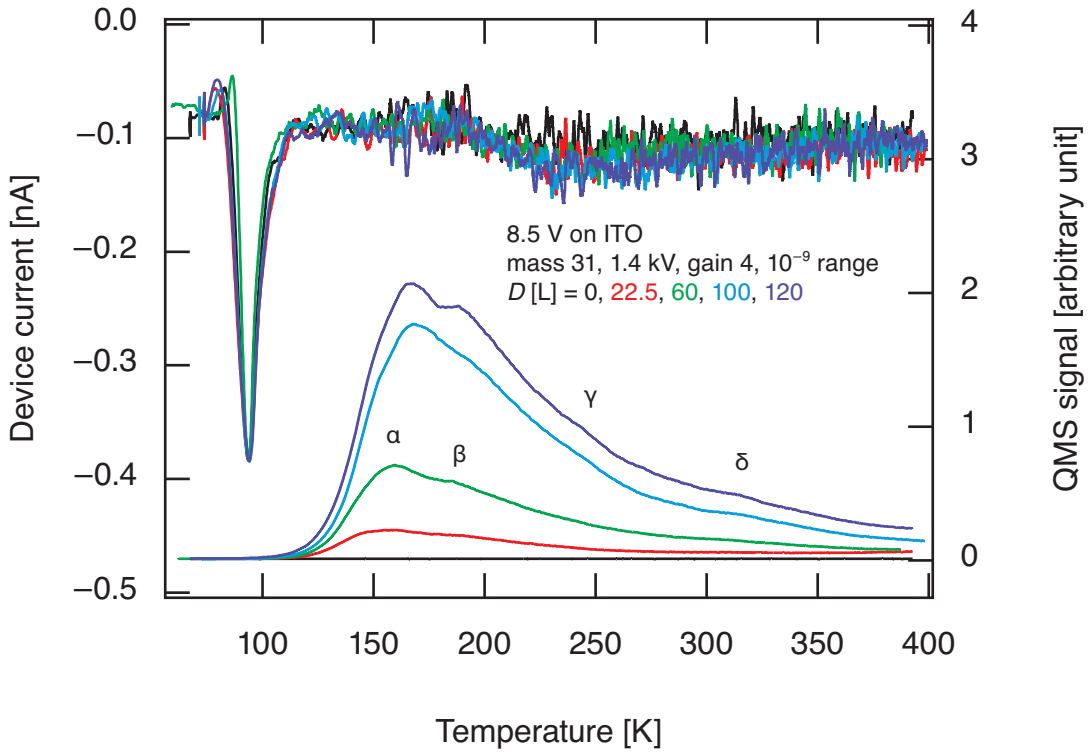

Figure 4.9: TPD spectra of CH_3CH_2OH from the Pt top electrode of the MIM device recorded at mass 31 u (bottom) and the simultaneously monitored device currents (top)

Only faint dips in the monitored device currents were observed for ethanol desorbing from the platinum top electrode at temperatures between ≈ 220–270 K (weak even for dosages up to 120 L). Steric effects could explain the weaker dips in the device currents for ethanol compared to methanol. Here, the increased size of the participating molecules (the longer carbon chain) possibly hampered the interaction of the hydroxy group with the platinum surface.

4.1.1.5 $(CH_3)_2CHOH$

In order to prove the assumption that steric effects hamper the O−Pt interaction in the course of desorption and adsorption of alcohols, also vapor of isopropyl alcohol (AR grade) was dosed onto the platinum top electrode at $\approx 65\,\mathrm{K}$. The device current increased slightly due to the adsorption process, but again much smaller in magnitude compared to the other studied alcohols. Not even dosages of $D = 225\,\mathrm{L}$ caused clear device current peaks. Also the peaks that resulted from closing the leak valve and terminating the dosing process could not be observed here.

TPD experiments were carried out by applying a voltage of 8.5 V across the ITO film in order to heat the sample. Desorbing molecules or fragments of isopropyl alcohol were ionized using an ion source voltage of 68.7 V and mass 45 u was detected. Again two peaks were observed in the TPD spectra that represent physisorbed multilayers and a chemisorbed monolayer on the Pt surface. In good agreement with TPD spectra of isopropyl alcohol desorbing from crystalline platinum surfaces, a low temperature desorption peak (α) at $\approx 155\,\mathrm{K}$ and a high temperature desorption peak (β) at $\approx 190\,\mathrm{K}$ were observed (see figure 4.10). An additional peak (γ) for high dosages of $D = 225\,\mathrm{L}$ was observed at $\approx 290\,\mathrm{K}$.

The late (or high temperature) desorption features (γ and δ) were also observed in the thermal desorption spectra carried out for methanol and ethanol by detecting mass 31 u (see figures 4.7 and 4.9). These TPD experiments and the performed isopropyl alcohol TPD experiment had in common that the masses used for detection (31 u and 45 u) correspond to molecule fragments that include H. By design these TPD measurements were blind to produced CO_2, CO, or any other species lighter than the detected masses. Thus, the γ and δ desorption features were attributed to the desorption of more strongly bound alcoholates.

Nearly no dips were observed in the monitored device currents during the desorption of isopropyl alcohol from the platinum top electrode (not even for huge dosages up to $D = 225\,\mathrm{L}$). Thus, the assumption that steric effects hamper the interaction of the hydroxy group with the platinum surface is highly

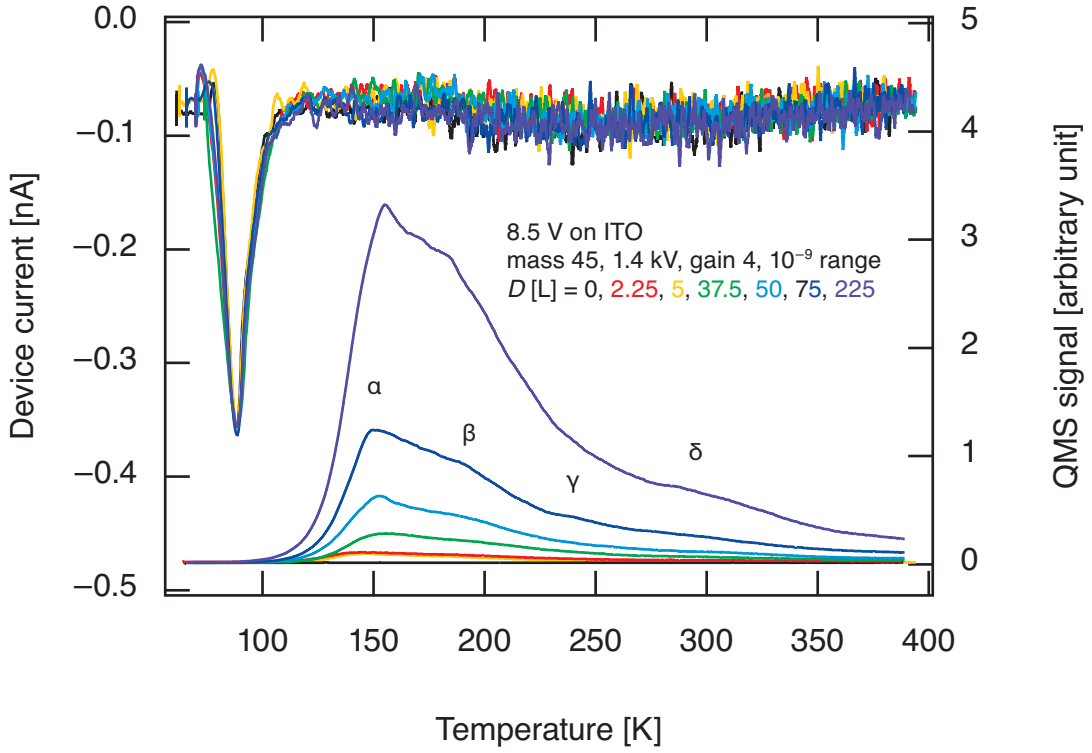

Figure 4.10: TPD spectra of $(CH_3)_2CHOH$ from the Pt top electrode of the MIM device recorded at mass 45 u (bottom) and the simultaneously monitored device currents (top)

plausible.

4.1.1.6 NH_3

As another small molecule that might participate in hydrogen bonding networks on platinum surfaces, ammonia was studied in adsorption and desorption experiments. For this purpose, ammonia (3.8, 99.98 %) was dosed from a steel gas cylinder through a leak valve into the UHV chamber where it adsorbed on the Pt top electrode of the nanodevice. Simultaneously, the device current was monitored.

As a result of the adsorption process peaks to positive currents were detected (see figure 4.11). Sharp peaks up to ≈ 0.35 nA were caused by dosages of $D = 80$ L and decreased exponentially (negative exponent) also below the

initial baseline of the device current. For smaller dosages below 7.5 L this current compensation was not observed. After closing the leak valve again the device current returned to the initial baseline. Here, no peaks to positive current values were observed due to closing the valve.

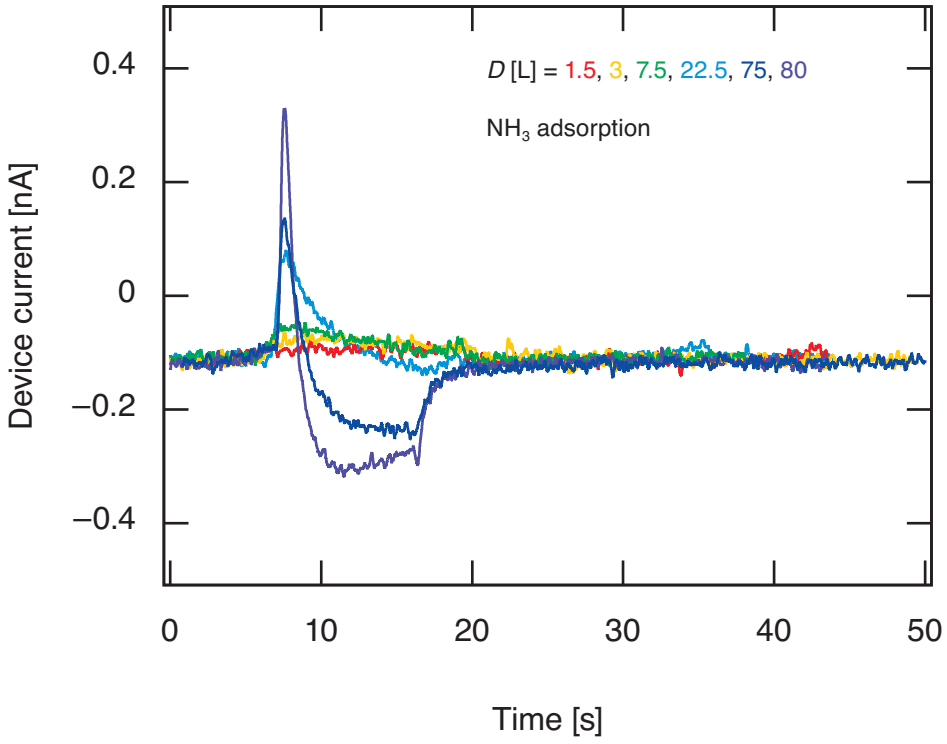

Figure 4.11: Response of the MIM device current to NH_3 adsorption on the Pt top electrode: at $t \approx 5$ s the leak valve was opened, at $t \approx 17$–20 s the valve was closed again.

TPD experiments were performed by applying a voltage of 9.5 V across the ITO backside film. Desorbing ammonia was ionized using an ion source voltage of 68.7 V and mass 16 u was detected. The thermal desorption spectra showed a broad culmination of various desorption peaks (see figure 4.12). In fairly good agreement with studies of NH_3 desorbing from Pt(111) surfaces the most dominant features in the spectra were observed at $\approx$ 160–190 K (α), $\approx$ 200–240 K (β), and $\approx$ 280–310 K (γ) for dosages of $D = 200$ L. For higher dosages up to $D = 375$ L these peaks shifted slightly, broadened up, and especially the α desorption feature increased. For lower dosages up to 75 L the α

desorption feature was not observed.

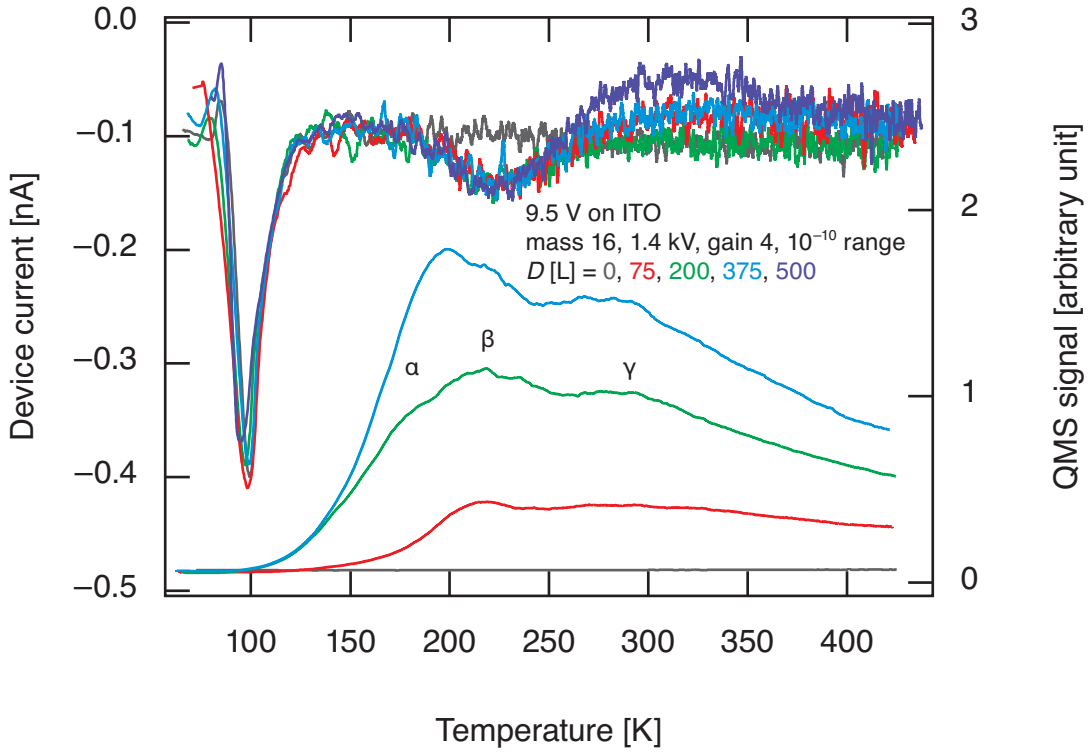

Figure 4.12: TPD spectra of NH_3 from the Pt top electrode of the MIM device recorded at mass 16 u (bottom) and the simultaneously monitored device currents (top)

The monitored device currents decreased directly after surface temperatures of 100 K were reached with increasing desorption fluxes. These observed dips seemed already saturated with dosages around 75 L. However, after 200 K was reached the device currents increased above the initial baseline in case of high dosages and peaks were observed that shifted to lower temperatures with increasing dosage. For $D = 500$ L a peak maximum at ≈ 260 K was observed. In a control experiment without NH_3 dosage the monitored device current remained on the initial baseline.

4.1.1.7 HCOOH

In order to clarify the role of proton donation and acceptance in the course of adsorption and desorption and due to the tendency to form extensive hydrogen bonding networks, the vapor of formic acid (98 %, AR grade) was dosed from a glass vial through a leak valve into the UHV chamber as well.

Compared to alcohols, the device current was very sensitive to the adsorption of formic acid and decreased rapidly with dosing (down to $\approx -0.8\,\mathrm{nA}$ for $D = 3.75\,\mathrm{L}$). While the pressure inside the chamber was held constant the current rose back exponentially (negative exponent, see figure 4.13). Dosages smaller than $\approx 1\,\mathrm{L}$ caused small current decreases. It was observed again that closing the leak valve caused an increase of the device current that scaled with the dosage and decreased exponentially (negative exponent). For small dosages up to $D = 1.5\,\mathrm{L}$ this increase with closing the valve was not observed.

Thermal desorption experiments were performed analogously to the previous TPD experiments. Voltages in the range of 8–9 V were applied across the ITO backside film in order to heat the sample and temperature desorption spectra were recorded using the quadrupole mass analyzer. Desorbing fragments of formic acid or intact formic acid molecules were ionized using an ion source voltage of 68.7 V and mass 28 u, mass 29 u, or mass 44 u (CO, HCO, or CO_2) were detected. Between each TPD experiment and the next dosing of formic acid vapor, the sample was cooled for 5 min. Another 5 min were spent after each adsorption cycle in order to pump the vacuum system back to a base pressure of $\approx 2 \times 10^{-10}\,\mathrm{mbar}$. Non-linear temperature ramps comparable to the previously discussed TPD experiments with water, alcohols, and ammonia were carried out. Thermal desorption spectra were obtained that are in good agreement with spectra of formic acid desorbing from platinum single crystal surfaces (see figures 4.14, 4.15, 4.16, and 4.17).

For high exposures multilayer desorption features (α) with zero-order desorption kinetics were observed at $\approx 155\,\mathrm{K}$ and attributed to the desorption of dimers and oligomers of formic acid. In a high-resolution TPD spectrum with a moderate heating rate (see figure 4.14) also an additional small shoulder was visible and α_1 and α_2 could be distinguished—possibly a distinction

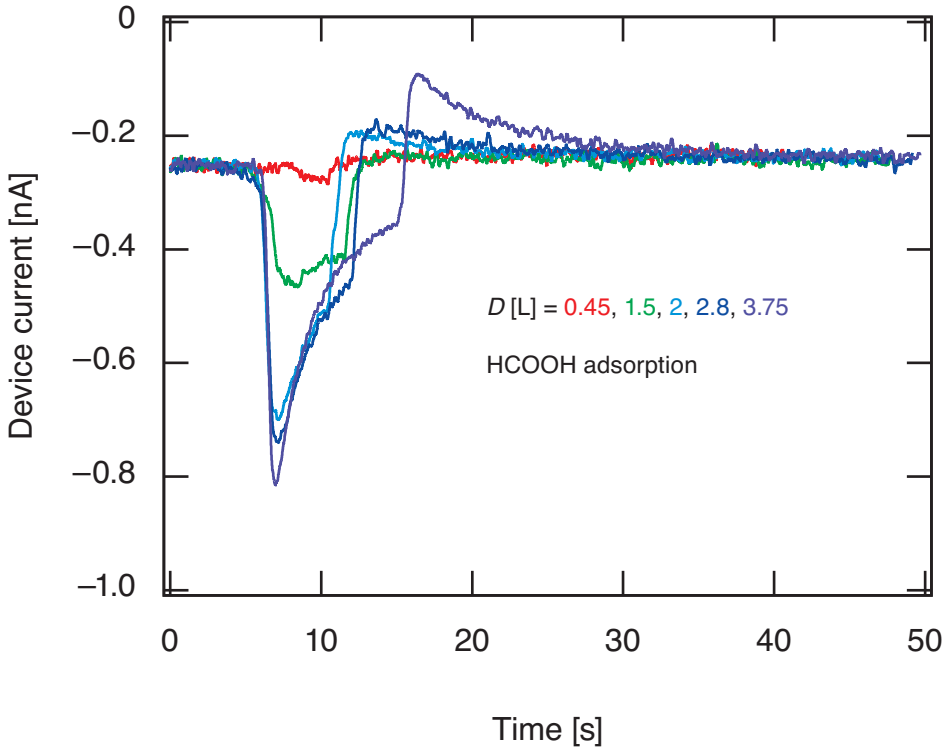

Figure 4.13: Response of the MIM device current to HCOOH adsorption on the Pt top electrode: at $t \approx 5\,\mathrm{s}$ the leak valve was opened, at $t \approx 11$–$16\,\mathrm{s}$ the valve was closed again.

between oligomers $(HCOOH)_n$ and dimers $(HCOOH)_2$. At $\approx 170\,\mathrm{K}$ another desorption feature (β) was observed that could be explained by dimer desorption of formic acid as well. A broader desorption feature (γ) at ≈ 180–$200\,\mathrm{K}$ was observed and attributed to the desorption of formic acid monomers. Dependent on the sensitivity of the mass analyzer, an additional desorption peak at $\approx 185\,\mathrm{K}$ was visible (see figure 4.14) and the monomer desorption feature could be distinguished by γ_1 and γ_2. Another broad desorption feature (δ) was observed in the temperature range of 220–260 K and was attributed to the desorption of HCOOH produced by the surface-catalyzed reaction of formate with adsorbed hydrogen atoms. At $\approx 315\,\mathrm{K}$ another small desorption peak (ε) was observed for the highest exposures. An increased heating ramp (using an increased voltage of 8.5 V across the ITO film) caused a more pronounced δ

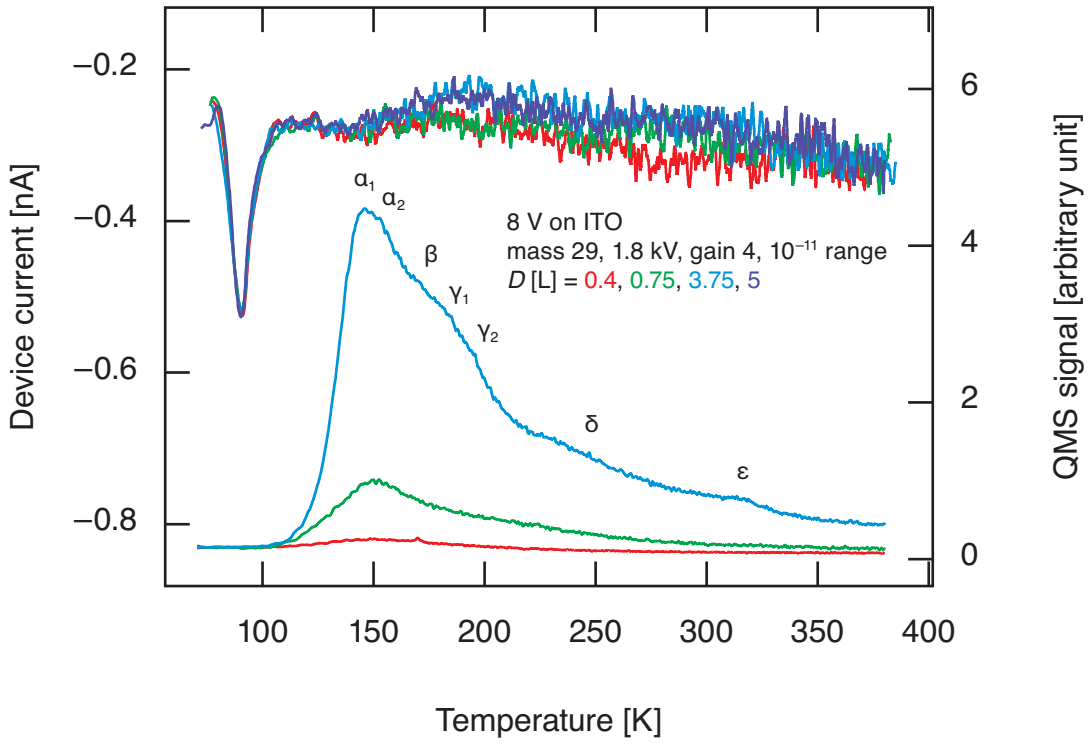

Figure 4.14: TPD spectra of HCOOH from the Pt top electrode of the MIM device recorded at mass 29 u (bottom) and the simultaneously monitored device currents (top)

desorption feature and a further increase of the QMS signal above 350 K even for an exposure of $D = 0.4$ L (see figure 4.15). An immediate repetition of the experiment revealed that the desorption features seen above 300 K were not observable anymore. Thus, it was assumed that surrounding adsorbates that had not been desorbed already in the previous experiment contributed to the detected QMS signals here. In addition, residual oxygen possibly contributed and was consumed in the course of further experiments.

In order to study the decomposition of formic acid over platinum, additional TPD experiments were performed by detecting masses of possible decomposition products: CO at mass 28 u and CO_2 at mass 44 u (see figures 4.16 and 4.17). For all obtained spectra the desorption features α–δ could be assigned. The ε desorption feature was more pronounced in the mass 44 u signal—but also here difficult to identify. Therefore, it can safely be assumed

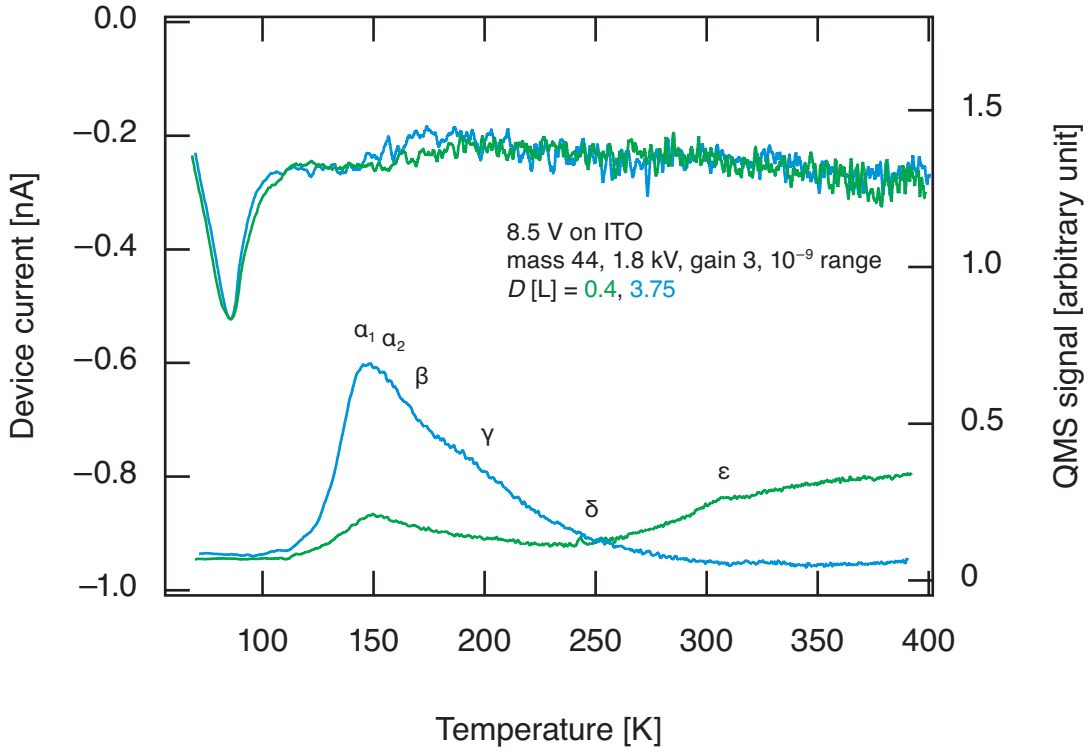

Figure 4.15: TPD spectra of HCOOH from the Pt top electrode of the MIM device recorded at mass 44 u (bottom) and the simultaneously monitored device currents (top): an increased voltage across the ITO film resulted in a pronounced desorption feature above 300 K in the first spectrum.

that the high temperature decomposition of formate to carbon dioxide is a minor reaction channel, especially at higher coverages in absence of adsorbed oxygen atoms. With increasing voltage across the ITO film from 8 V (figure 4.14), to 8.5 V (figure 4.15), to 9 V (figures 4.16 and 4.17) a slight shift of the γ desorption feature representing monomer desorption from $\approx$ 180 K up to 200 K was observed. This was attributed to the increased heating rate. No CO or CO_2 fragments contributed to the obtained spectra at mass 29 u due to the absence of an additional H atom and if isotopes of C and O are neglected. Thus, the detected QMS signal at mass 29 u was attributed to non-decomposed and intact molecules of HCOOH that were cracked by the QMS ion source. In turn, non-decomposed formic acid was expected to contribute to the spectra obtained for 28 u and 44 u. The presence of dominant oligomer and dimer

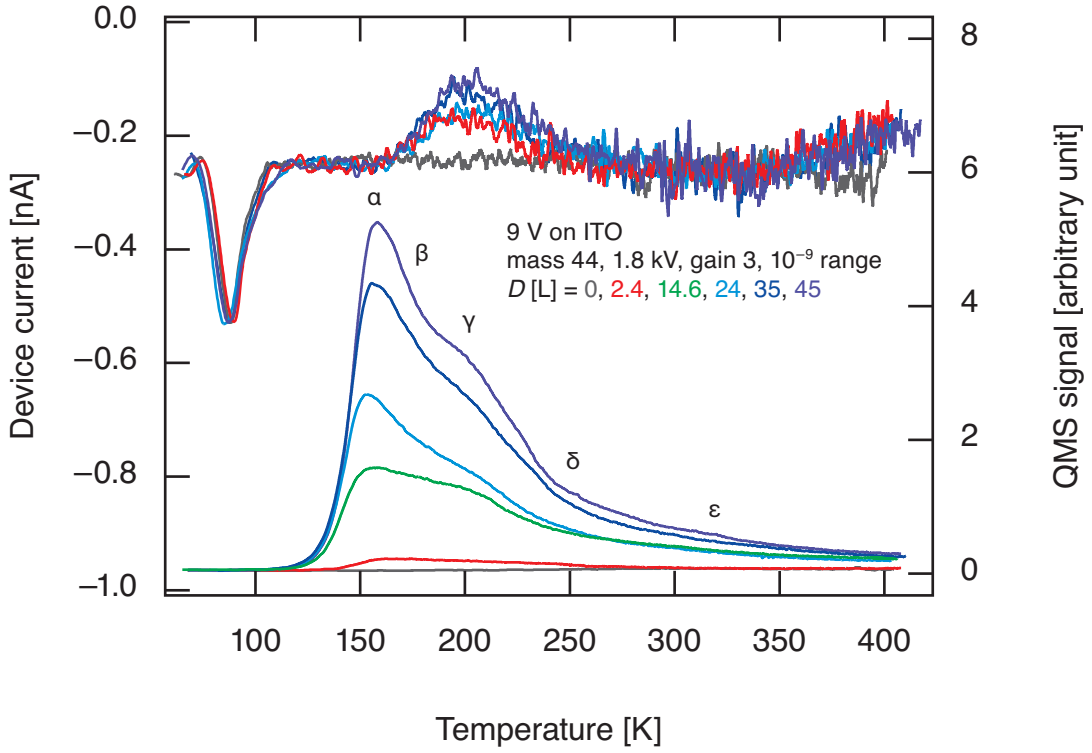

Figure 4.16: TPD spectra of HCOOH from the Pt top electrode of the MIM device recorded at mass 44 u (bottom) and the simultaneously monitored device currents (top)

peaks (α and β) in all spectra suggests that.

T [K]	Reactants	Desorbing product(s)	Desorption feature
140–150	α-$HCOOH_{(a)}$	$(HCOOH)_{n(g)}$	α_1
150–160	β-$HCOOH_{(a)}$	$(HCOOH)_{2(g)}$	α_2
170–180	β-$HCOOH_{(a)}$	$(HCOOH)_{2(g)}$	β
165–185	$2\,HCOO_{(a)}$	$CO_{2(g)}$	β–γ for 44 u and 28 u
180–200	$HCOO_{(a)} + H_{(a)}$	$HCOOH_{(g)}$	γ
250	$2\,HCOO_{(a)}$	$HCOOH_{(g)} + CO_{2(g)}$	δ
315	$2\,HCOO_{(a)}$	$HCOOH_{(g)} + CO_{2(g)}$	ε

Table 4.1: HCOOH thermal desorption features and assigned surface reactions

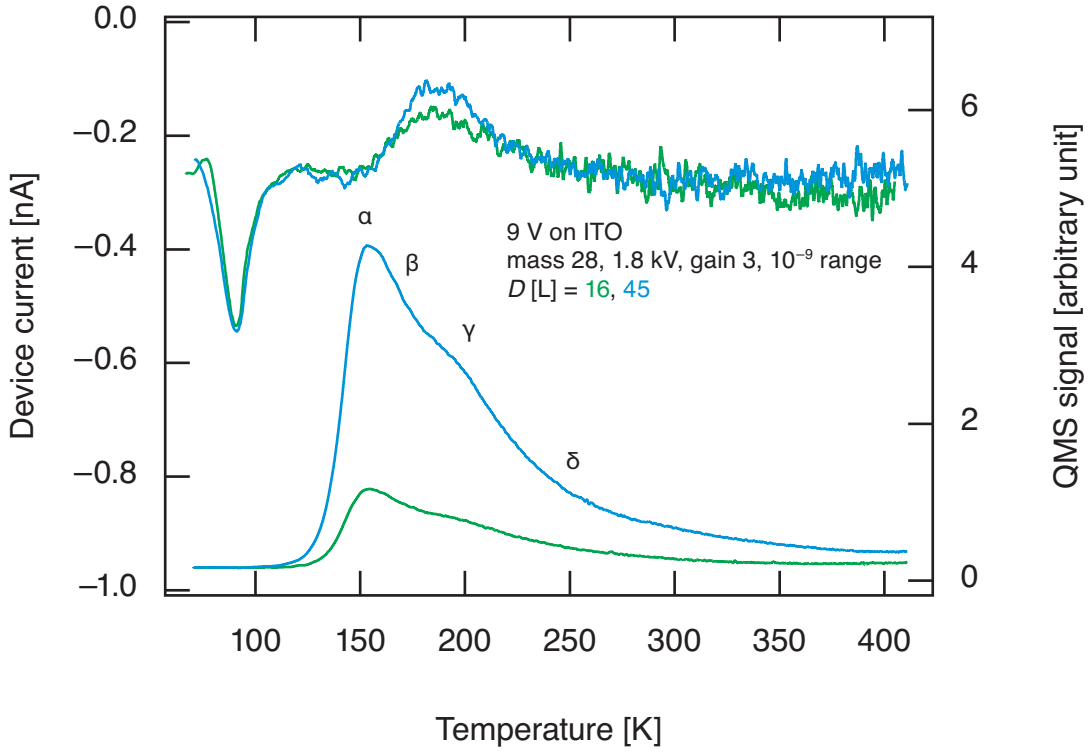

Figure 4.17: TPD spectra of HCOOH from the Pt top electrode of the MIM device recorded at mass 28 u (bottom) and the simultaneously monitored device currents (top)

CO_2 was expected to contribute to the spectra obtained at mass 44 u (and as a fragment from cracking also at mass 28 u) in small amounts in the temperature range of 165–185 K due to the minor decomposition pathways according to reaction 2.43 and more pronounced in the temperature range of 250–315 K due to the formate decomposition according to reaction 2.45. However, in all spectra at mass 44 u and mass 28 u the most dominant desorption features were observed below 250 K (even for small exposures). Thus, it could be assumed that either the decomposition of formic acid predominantly followed the low temperature reaction pathways or that the decomposition was a marginal process here. The observed desorption features and the assigned surface reactions are summarized in table 4.1. A comparison of TPD spectra of similar exposures (for instance $D = 3.75$ L) at mass 29 u and mass 44 u (see figures 4.14 and

4.15) revealed that the oligomer and dimer desorption features α–β were (apart from the different QMS sensitivity and the slightly lower heating rate) more pronounced at mass 29 u. In turn, it seemed that at mass 44 u the QMS signal intensity in the temperature range of 165–220 K was more dominant compared to the α desorption feature(s). This was attributed to desorbing CO_2 that was produced in low temperature decomposition reactions and contributed to the QMS signal exclusively at 44 u.

In contrast to TPD experiments with water and alcohols, the device currents monitored during the HCOOH thermal desorption experiments exhibited peaks to more positive current values. These device current variations scaled with dosage and the peak maxima shifted slightly to lower temperatures with increasing dosage. It seemed that the peak temperature shifted to higher values with increasing heating rate but after closer comparison and considering more experiment cycles it could be confirmed that the observed peak temperature somehow varied in the range of 185–200 K. In retrospect, a significant increase in the resistivity of the ITO was recognized that changed the heating rate slightly. Therewith, the peak shift to lower temperatures despite using the same voltages across the ITO for continuous experiments was understandable and the assumption remained that the observed peak temperatures scaled with the heating rate. Furthermore, it was observed that for higher dosages the device current decreased or increased at temperatures above 350 K and an increasing signal noise was noticeable. This effect seemed to scale with dosage as well but was attributed to instability of the device current signal and leakage currents as a result of the increasing temperature.

This effect was also recognized when changing the bias voltage between the MIM electrodes to $U_{\text{bias}} = 10\,\text{mV}$ for formic acid thermal desorption experiments, motivated to amplify the detected device current peaks in the course of formic acid desorption and/or decomposition (see figure 4.18). Indeed, besides starting from a much higher device current baseline of 1.3 nA the current increased up to 1.6 nA at a surface temperature of $T = 185\,\text{K}$. This temperature was observed for the device current peak maxima in previous desorption experiments with an applied voltage of 9 V across the ITO as well (see figure 4.17). However, after reaching the maximum the current did not de-

crease again but increased further—presumably due to leakage currents as a result of the increasing temperature. The saddle point at $\approx 200\,\mathrm{K}$ could be attributed to a compensation of the chemically induced device current by the leakage currents. For comparison, the monitored device current of a TPD experiment using the same parameter settings but without an applied bias voltage ($U_{\mathrm{bias}} = 0\,\mathrm{mV}$) was offset to the same current baseline and displayed in figure 4.18. Both devices currents reached a maximum at $T = 200\,\mathrm{K}$ but the voltage assisted device current increased earlier—more precisely: at a lower temperature. It could be noted, that a bias voltage of $U_{\mathrm{bias}} = 10\,\mathrm{mV}$ allowed for the amplification of the observed device current peaks due to the formic acid desorption/decomposition.

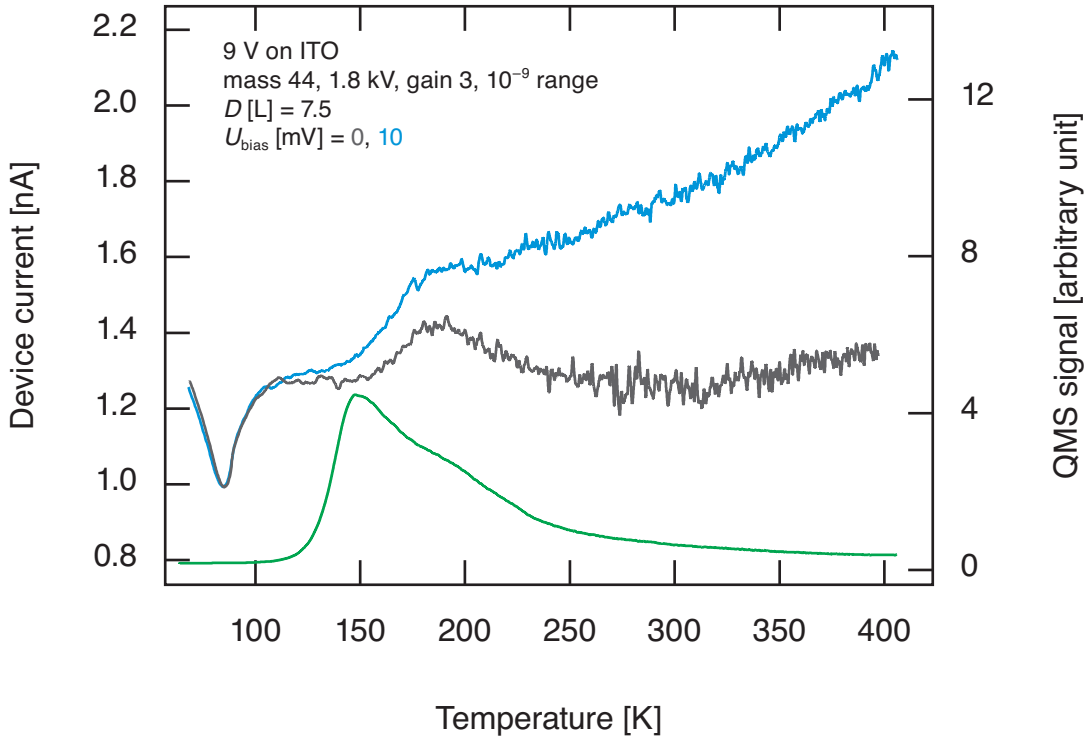

Figure 4.18: HCOOH thermal desorption spectrum (green) and simultaneously monitored device current with an applied bias voltage of $U_{\mathrm{bias}} = 10\,\mathrm{mV}$ (blue) and an applied bias voltage of $U_{\mathrm{bias}} = 0\,\mathrm{mV}$ (dark gray, offset for comparison)

Certainly, changes in the configuration of the adsorbed HCOOH modifications (for instance α-$\mathrm{HCOOH}_{(a)} \longrightarrow \beta$-$\mathrm{HCOOH}_{(a)}$ or deprotonation reac-

tions and changes from monodentate formate to bidentate formate and vice versa) occurred during each TPD experiment and caused different desorption features in the obtained spectra. Thus, changes in the surface potential of the platinum film due to bond formation and/or bond cleavage could be assumed. Here, device current increases were measured that could be assigned to a decreased electron density that was compensated by providing an electron flow toward the platinum electrode from the potentiostat in order to maintain the constant bias voltage. Due to the fact that the decomposition of formic acid over platinum is an exothermic reaction and produced carbon dioxide could desorb from the surface without establishing a vibrational equilibrium (comparable to reaction pathways in the carbon monoxide oxidation over platinum) non-adiabatic effects could neither be excluded here. In that case, also induced hot charge carriers could have tunneled through the Ta_2O_5 barrier and contributed to the detected device currents. Comparable to the detected device current changes due to H_2O ad- and desorption, signs of saturation with increasing coverage were observed here (see figure 4.19). In addition, the absolute values of the ad- and desorption charges were comparable for similar exposures

The fact that the device current increased at temperatures of $\approx 155\,\mathrm{K}$ and reached a maximum within the temperature range of the low temperature decomposition reaction of 180–200 K could suggest that the decomposition of monodentate formate into carbon dioxide and adsorbed atomic hydrogen or the decomposition of two monodentate species into carbon dioxide and adsorbed formic acid caused the device current increase. The reaction of adsorbed atomic hydrogen with formate to produce formic acid at 200 K should be considered as well.

4.1.2 Adsorption experiments at normal temperature

In addition, adsorption experiments at normal temperature and higher gas exposures were carried out in order to study the device current response to pure gases, vapors, and gas–vapor mixtures. For this purpose, gases were dosed from gas cans: H_2 (5.0), O_2 (5.0), Ar (5.0), and CO_2 (4.5); or steel gas

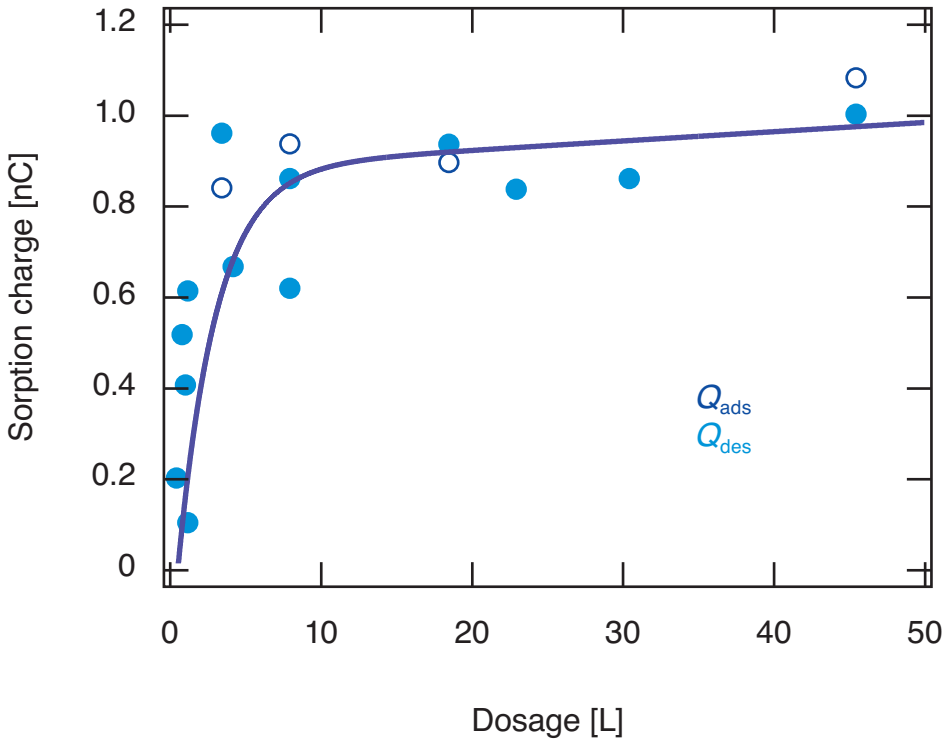

Figure 4.19: Absolute values of the HCOOH adsorption charges Q_{ads} (dark blue) and the HCOOH desorption charges Q_{des} (light blue) plotted against the corresponding dosages D: the reversible charges due to adsorption and desorption processes reached a saturation at $D \approx 4$–$6\,\mathrm{L}$.

cylinders: NH_3 (3.8) and CO (4.7). The vapor of H_2O (purified using a Merck Millipore Simplicity water purification system) was dosed from a glass vial through a leak valve into the UHV chamber. Simultaneously, the device current was monitored.

It was observed that the adsorption of gases or vapors caused negative device currents, regardless of the chemical properties of the dosed species if pressures above $p = 5 \times 10^{-5}\,\mathrm{mbar}$ were reached inside the UHV chamber and monitored using the AML Bayard–Alpert ionization gauge. This was attributed to the ionization of the dosed gases or vapors in the hot filament of the ionization gauge: adsorbing positive charged molecules caused an electron flow toward the platinum electrode from the potentiostat in order to keep the MIM device at a constant bias voltage. Therefore the AML Bayard–Alpert

ionization gauge was switched off during the high pressure adsorption experiments and the Leybold Vacuum IONIVAC ITR 90 combination gauge that was separated from the main chamber by a copper shield was used instead. The pressures measured with the ionization gauge were corrected using gas correction factors. At normal temperature no internal (vertical) or lateral temperature gradients were expected due to thermal bridges in the course of the gas/vapor exposures (that should be considered for gas/vapor–nanodevice interactions at pressures above 1×10^{-3} mbar according to [104]) and all device current changes were attributed to surface potential changes of the top platinum electrode in the course of adsorption, dissociation, and/or recombination of the dosed gases and vapors and/or reaction with pre-adsorbed species. In case of current increases toward more positive current values, possibly also non-adiabatic effects contributed.

Different device current responses were observed:

The device current decreased rapidly down to -5.5 nA due to the exposure to H_2 pressures up to 4.6×10^{-6} mbar and relaxed back to the initial baseline with decreasing pressure.

After a small increase to more positive current values the device current decreased rapidly by about 3 nA due to the exposure to NH_3 pressures up to 1.3×10^{-5} mbar and (even at constantly high pressures) increased exponentially (negative exponent) back to the current baseline (and slightly above for higher dosages as well for a limited time).

The device current increased rapidly by about 1.4 nA due to the exposure to H_2O pressures up to 5.5×10^{-8} mbar, decreased exponentially (negative exponent) back to the current baseline (even at still increasing pressures). Closing the leak valve in order to terminate the exposure caused a rapid decrease of the device current below the baseline that increased exponentially (negative exponent) back to the current baseline.

The device current increased moderately by about 0.5 nA due to the exposure to CO pressures up to 2×10^{-5} mbar and saturation effects were

observed as even increased CO pressures caused only faint increases in following experiments.

The device current increased by about 2.3 nA due to the exposure to O_2 pressures up to 8×10^{-6} mbar and relaxed back to the initial baseline (and slightly below as well for a limited time) with decreasing pressure.

The device current faintly increased by about 0.11 nA due to the exposure to Ar pressures up to 6.5×10^{-6} mbar and relaxed back to the initial baseline (and slightly below as well for a limited time) with decreasing pressure.

The device current faintly increased by about 0.13 nA due to the exposure to CO_2 pressures up to 4.2×10^{-6} mbar and relaxed back to the initial baseline (and slightly below as well for a limited time) with decreasing pressure.

Faint oscillation in the device current were observed even for Ar and CO_2 exposures that were attributed to rearrangements of the pre-adsorbed surface constellations due to the gas molecules impact. Furthermore, it was observed that closing the leak valve led to device current modifications. In the case of H_2O a rapid drop of the device current was observed due to closing the leak valve (see figure 4.20). In contrast, for H_2O adsorption experiments carried out at $T = 65$ K an increase in the device current resulted from closing the valve. Both current modifications relaxed back exponentially (negative exponent) to the initial current baseline. The different temperature in both cases should be considered in order to explain the opposite direction of the current response. At 65 K the vast majority of the H_2O molecules condensed on the Pt electrode. At normal temperature an equilibrium between desorption and adsorption was established and closing the leak valve shifted the equilibrium toward desorption. Therewith, the observed device current drop could validate the measured device current drops that were measured in the course of H_2O thermal desorption experiments. The current increase due to the termination of the H_2O exposure at 65 K could be explained by an equilibrium of molecule sticking on top of multilayers and the abrading of loosely bound molecules

from multilayers due to the impacts of approaching molecules: by terminating the H_2O feed abrading was canceled out and the equilibrium was shifted abruptly to adsorption. The observation of this current increase exclusively for high exposures and the scaling of the effect with exposure supported this assumption.

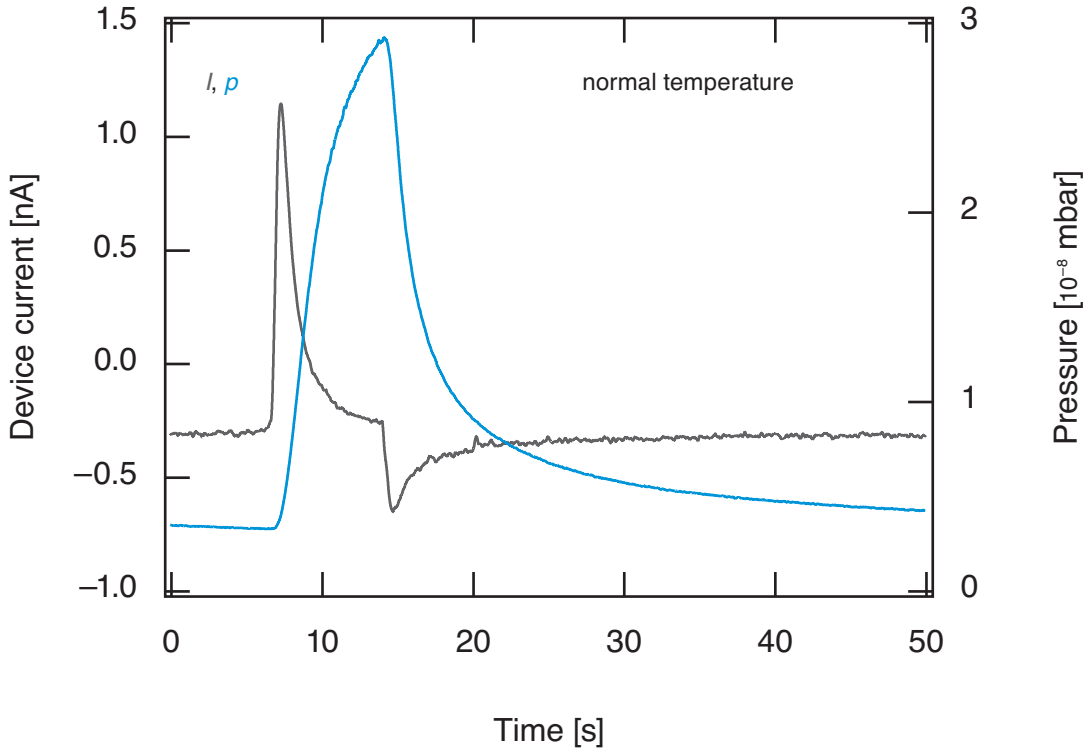

Figure 4.20: Increase of the MIM device current (dark gray) due to H_2O exposure: at $t \approx 6\,\mathrm{s}$ the leak valve was opened, at $t \approx 14\,\mathrm{s}$ the valve was closed again.

Furthermore, it was observed that pre-adsorbed oxygen intensified the device current decrease due to the exposure to H_2 (see figure 4.21). Here, a corrected pressure of $p = 1.1 \times 10^{-4}\,\mathrm{mbar}$ caused a temporary decrease of the device current of $\approx 2.9\,\mathrm{nA}$. In case of pre-adsorbed O_2 (saturation coverage) even a slightly lower corrected pressure of $p = 1 \times 10^{-4}\,\mathrm{mbar}$ caused a temporary decrease of $\approx 5.3\,\mathrm{nA}$. In both experiments the current minimum was observed at $t \approx 12\,\mathrm{s}$. For lower pressures the observed current minima appeared later. For all pressures the device current decreased shortly after the

leak valve was opened in order to initiate the exposure at $t \approx 7\,\mathrm{s}$ and relaxed back exponentially (negative exponent) to the initial baseline within 30–35 s. Faint increases above the current baseline were observed for higher exposures. Abstraction reactions possibly resulted after H_2 dissociated on the platinum surface and O–Pt bonds were cleaved. Electron density in the Pt electrode increased in this case and an electron flow from the potentiostat was provided in order to maintain the constant bias voltage between the two MIM electrodes.

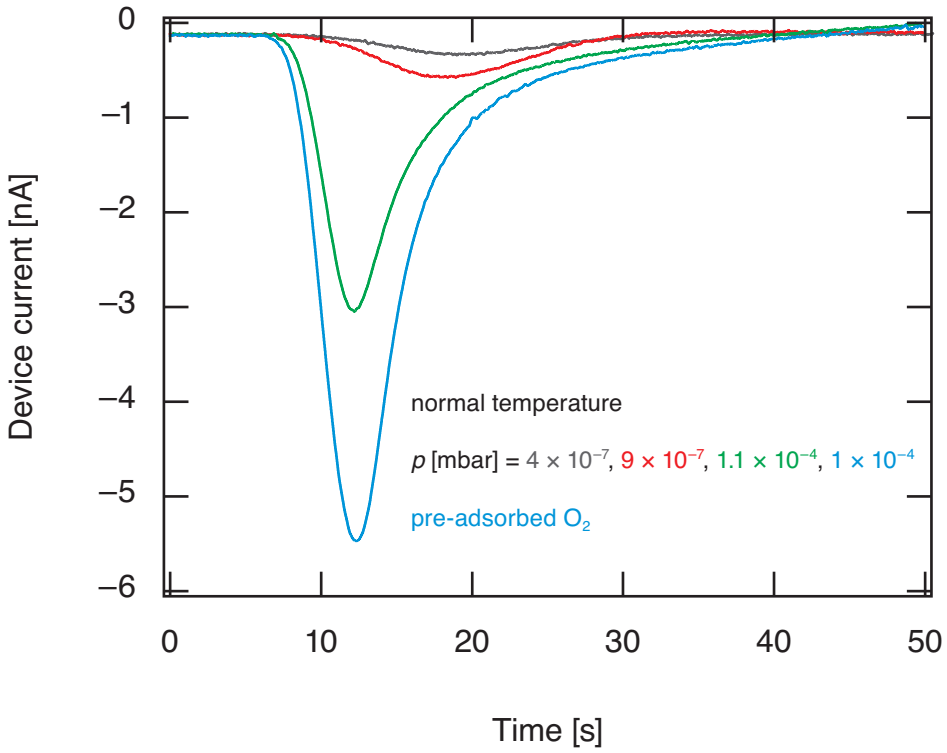

Figure 4.21: Decrease of the MIM device current due to H_2 exposure at normal temperature: at $t \approx 7\,\mathrm{s}$ the leak valve was opened, pre-adsorbing O_2 intensified the decrease.

It could be noted, that the exposure to H_2 caused the most drastic decrease of the monitored device currents and significant increases in the device currents were observed for the exposure to H_2O and O_2. In order to study possible surface-catalyzed reactions of these molecules (for instance the water formation reaction or the formation and modification of water–hydroxy mixed phases) different gas/vapor mixtures of $H_2 + O_2$ and $H_2O + H_2$ were prepared

in the steel vessel reservoir and dosed through the leak valve into the main vacuum chamber onto the Pt electrode. Simultaneously, the device current was monitored.

Dosing a mixture of $H_2 + O_2$ ($p_{H_2} \approx 25\,\text{mbar}$ and $p_{O_2} \approx 25\,\text{mbar}$ in the gas inlet system) resulted in a corrected pressure of $p = 3.7 \times 10^{-7}\,\text{mbar}$ in the main chamber (see figure 4.22). This exposure caused a broad device current drop of $\approx 0.2\,\text{nA}$ over a period of $\Delta t \approx 40\,\text{s}$ and a faintly discernible increase of the device current (rather a delay of the decrease) during the first 4 s after the leak valve was opened at $t \approx 5\,\text{s}$. Dosing a mixture of $H_2 + 3\,O_2$ ($p_{H_2} \approx 25\,\text{mbar}$ and $p_{O_2} \approx 75\,\text{mbar}$ in the gas inlet system) resulted in a corrected pressure of $p = 1 \times 10^{-6}\,\text{mbar}$ in the main chamber. This exposure caused a significant increase of the device current by 0.08 nA immediately after opening the leak valve with a peak maximum at $t \approx 6.5\,\text{s}$ and a decrease afterward down to 0.37 nA below the initial device current baseline. A current minimum was observed at $t \approx 22.2\,\text{s}$. Subsequently, the device current relaxed back to the initial baseline. Dosing a mixture of $H_2 + 4\,O_2$ ($p_{H_2} \approx 25\,\text{mbar}$ and $p_{O_2} \approx 100\,\text{mbar}$ in the gas inlet system) resulted in a corrected pressure of $p = 1.6 \times 10^{-6}\,\text{mbar}$ in the main chamber. This exposure caused a large initial increase of the device current ($\Delta I \approx 0.15\,\text{nA}$) at $t \approx 6.5\,\text{s}$, but a large decrease afterward as well: at $t \approx 20\,\text{s}$ a minimum of $\approx 0.82\,\text{nA}$ was observed that increased back to the initial current baseline.

It could be noted, that increasing the partial pressure of oxygen in the $H_2 + O_2$ mixture intensified the initial device current peak. The broad current drop afterward could be caused by the presence of H_2. Comparable pressures of pure H_2 caused similar drops (see figure 4.21). Also, the relaxation to the current baseline proceeded analogously to experiments with pure H_2.

Dosing a mixture of $H_2 + H_2O$ ($p_{H_2} \approx 25\,\text{mbar}$ and $p_{H_2O} \approx 25\,\text{mbar}$ in the gas inlet system) resulted in a corrected pressure of $p = 3 \times 10^{-7}\,\text{mbar}$ in the main chamber (see figure 4.23). This exposure caused a slight initial peak of the device current of 0.2 nA with a maximum at $t \approx 6.4\,\text{s}$ that exponentially decayed afterward over a long period and reached a current minimum of 0.2 nA below the current baseline at $t \approx 23.2\,\text{s}$. Subsequently, the device current increased slowly back to the initial current baseline. Dosing a mixture

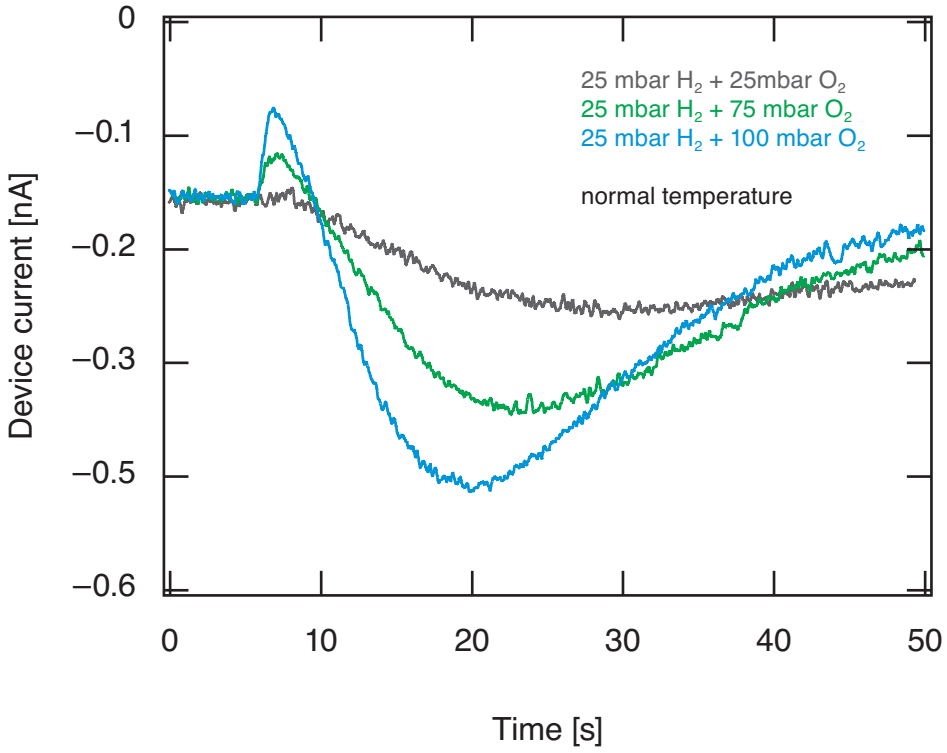

Figure 4.22: MIM device current response to H_2 + O_2 exposures: at $t \approx 5\,s$ the leak valve was opened.

of $H_2 + 2\,H_2O$ ($p_{H_2} \approx 25\,mbar$ and $p_{H_2O} \approx 50\,mbar$ in the gas inlet system) resulted in a corrected pressure of $p = 2.5 \times 10^{-6}\,mbar$ in the main chamber. This exposure caused more drastic current responses: an initial current maximum was observed at $t \approx 6.1\,s$ with an amplitude of $0.3\,nA$ and a current drop of $1.1\,nA$ below the current baseline at $t \approx 12.5\,s$. Dosing a mixture of $H_2 + 4\,H_2O$ ($p_{H_2} \approx 100\,mbar$ and $p_{H_2O} \approx 25\,mbar$ in the gas inlet system) resulted in a corrected pressure of $p = 2 \times 10^{-5}\,mbar$ in the main chamber. This exposure caused a sharp peak with an amplitude of $3.6\,nA$—rapidly increasing with opening the leak valve at $t \approx 5\,s$. An intense current drop of $2.6\,nA$ below the current baseline with a current minimum at $t \approx 11\,s$ was observed that increased exponentially (negative exponent) back to the current baseline afterward.

Again, the device current drops were attributed to the strong influence of

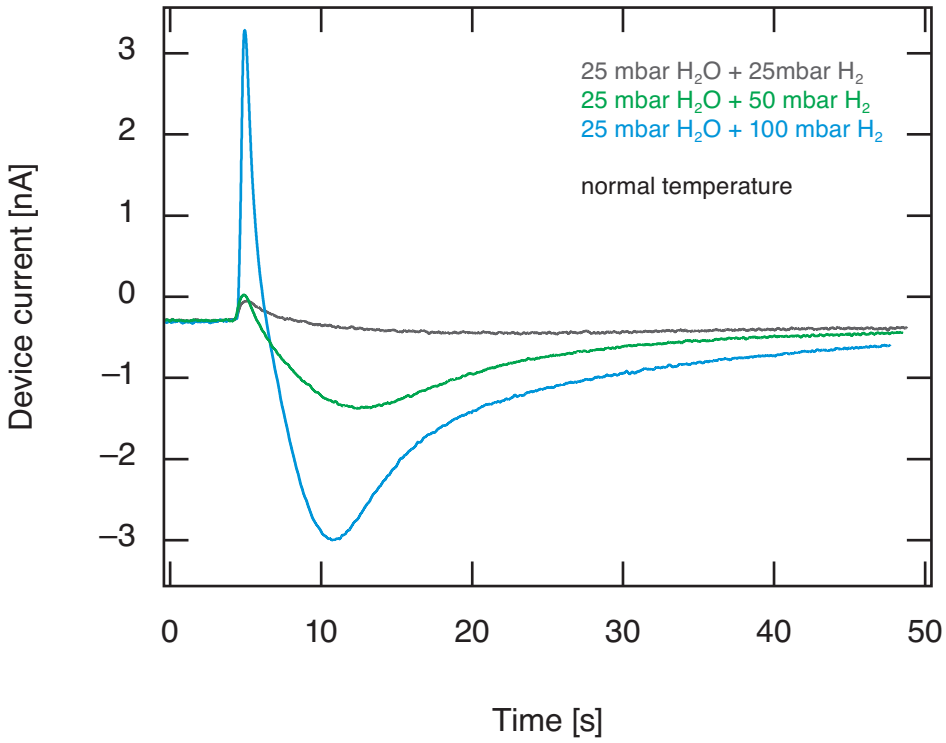

Figure 4.23: MIM device current response to H_2 + H_2O exposures: at $t \approx 5\,s$ the leak valve was opened.

H_2. The initial current peaks could be caused by the presence of H_2O and possibly increased with pressure during exposure and unlikely due to interactions of H_2 + H_2O. However, the device current responded faster to the exposure to H_2O and O_2, respectively. Apart from the observed initial current peaks the overall appearance of the obtained device current responses were dominated by H_2. Possibly dissociated H_2 caused surface reconstructions and migrated into the platinum to occupy sub-surface sites. Also sub-surface diffusion of migrated hydrogen could have occurred. [105] Solely surface potential changes were attributed to the measured negative currents. Here, an increase of the electron density of the platinum top electrode could be assumed and an electron flow toward the potentiostat resulted in order to maintain the constant bias voltage between the MIM electrodes. Changes of the electric charge distribution or the polarization of the platinum film due to the incorporation

of hydrogen into the platinum could explain the decrease of the device current. [63] Considering the huge pressures during the exposure experiments, relatively small device current increases were detected due to the exposure to O_2 or H_2O. Comparable peak amplitudes were observed as a result of the decomposition/desorption of formic acid.

In the course of H_2 adsorption experiments it was observed that the resistance of the used ITO films increased reversibly as a result of H_2 exposure. The reversal of this increase of resistance was monitored over a period of $\approx 300\,\mathrm{h}$ (see figure 4.24).

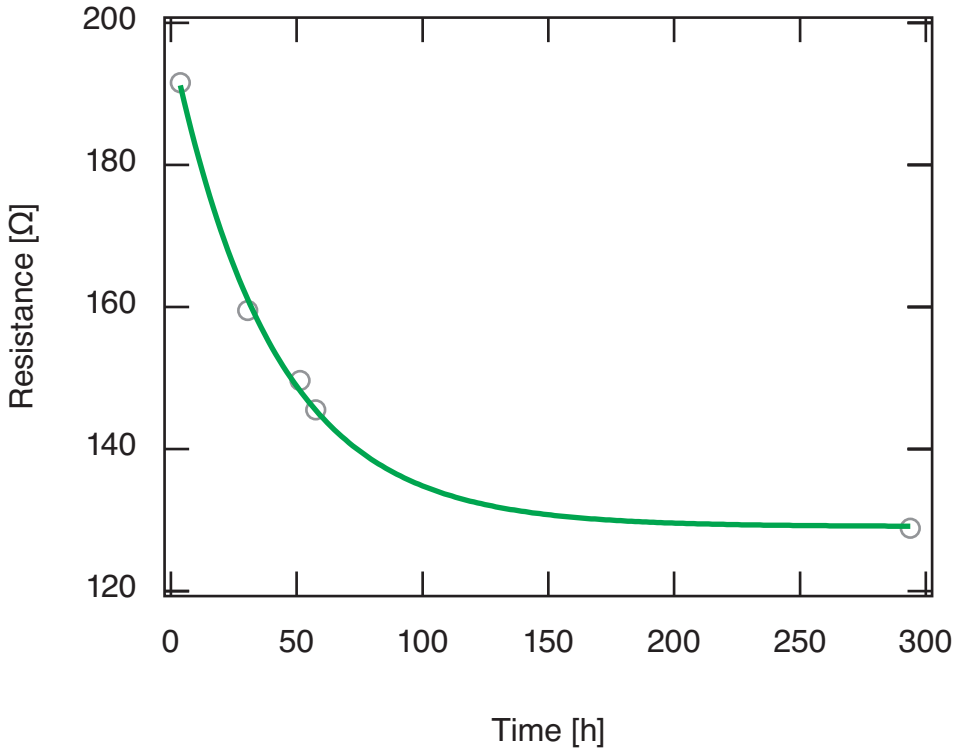

Figure 4.24: Reversal of the ITO resistance increase caused by H_2 exposure

During sputter deposition ITO is known for changing its electrical resistivity due to the gradual reduction of the oxygen content with changing hydrogen concentrations and due to hydrogen incorporation. Here, a lower resistivity of the ITO film represents oxygen vacancies while a higher resistivity represents the migration of interstitial hydrogen. In the course of performed H_2 adsorp-

tion experiments, hydrogen atoms were incorporated into the solid ITO film and occupied interstitial sites in the crystalline structure. Theses residing hydrogen atoms formed hydroxy bonds that acted as scattering centers for charge carriers—and caused the ITO film resistance to increase. [106, 107]

Also the dosing of formic acid possibly damaged the ITO film: it was observed, that after a cycle of HCOOH adsorbing and desorbing experiments the ITO film resistance increased irreversible. It was assumed that HCOOH removed partly the deposited ITO film according to the discussed susceptibility of ITO toward acids.

5 Discussion

The aim of this research was to identify non-adiabatic contributions in the course of surface-catalyzed reactions on platinum. Temperature programmed desorption experiments were carried out in the temperature range of 60–400 K in order to study the adsorption, the recombination, the decomposition, and the desorption of various species on the Pt top electrode of MIM chemoelectronic nanodiodes. A suitable method of temperature measurement was developed, calibrated, and applied that allowed for an *in-situ* temperature measurement with the MIM nanodiode. Therewith, exclusively the temperature of the MIM sandwich structure was measured. For the first time, temperature programmed desorption experiments from chemoelectronic nanodiodes were performed while simultaneously the device current was monitored. Significant MIM device current responses were detected due to sorption processes of H_2O, D_2O, methanol and formic acid: the monitored device current responded with drops to more negative current values or rises to more positive current values.

In the case of H_2O and D_2O adsorption and desorption dynamics the device current responded with drops to more negative current values or rises to more positive current values (negative in case of desorption and positive in case of adsorption). These device current changes were identified as reversible processes that were significant up to the first four monolayers but reached a saturation above six monolayers. For alcohols this effect was much weaker and fainted for alcohols with longer carbon chains—or more precisely a smaller OH : C ratio. It was suggested that the formation and the decomposition of hydrogen bonding networks on the platinum surface and the incorporation of pre-adsorbed oxygen caused the observed charges.

The adsorption of H_2O leads to the protonation of pre-adsorbed oxygen

atoms according to reaction 2.23. The formed hydroxy species are subsequently stabilized in a hydrogen bonding network of water overlayers. With the most stable $H_2O : OH$ ratio of $2 : 1$ this proceeds as:

$$5\,H_2O_{(a)} + O_{(a)} \longrightarrow 2\,OH_{(a)} + 4\,H_2O_{(a)}\,. \tag{5.1}$$

As OH incorporated into the hydrogen bonding network is less strongly bound to the platinum surface than atomic oxygen, electron density is transferred from the Pt toward the overlayer structure in case of H_2O adsorption onto the oxygen covered surface. With increasing temperature the overlayer structure decomposes, water desorbs, and OH is deprotonated again. The reformation of strong O–Pt bonds results in an increase of the electron density of the platinum film. In case of desorption the potentiostat collects an electron flow from the platinum. In case of adsorption the potentiostat provides an electron flow toward the platinum (see figure 5.1).

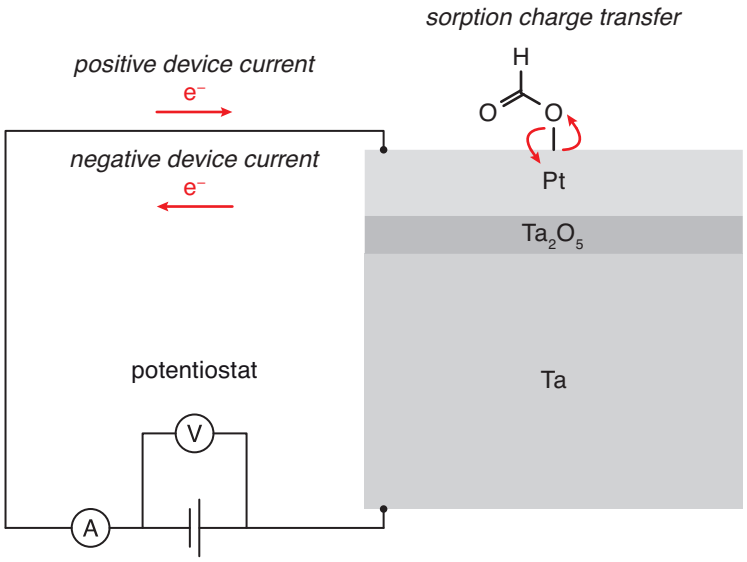

Figure 5.1: Measured device currents due to sorption charge transfer: positive device currents in case of an electron flow from the potentiostat toward the Pt film, negative device currents in case of an electron flow from the Pt film toward the potentiostat.

Corresponding to the saturation coverage ($\approx 0.25\,\mathrm{ML}$) of atomic oxygen on Pt(111) presumably one quarter of the participating surface sites were pre-

occupied with O. In order to protonate all pre-adsorbed atomic oxygen also 0.25 ML of H_2O was needed. In order to stabilize the formed 0.5 ML of OH species another monolayer of H_2O was required. The linear increase of the observed charges due to H_2O or D_2O desorption and adsorption (see figures 4.3, 4.3, 4.2, and also 4.5) up to exposures of $\approx$ 1–2 L supported this hypothesis. The polycrystalline nature of the platinum film could be responsible for the fact that the charges increased until exposures of $\approx$ 6 L. Presumably higher amounts of oxygen atoms were adsorbed on the surface due to a non-planar and rougher surface constitution with terraces of different crystal structures and more kinks and steps. A decreasing sticking probability or inaccuracies in the pressure measurement could be discussed here as well but the obtained TPD spectra confirm the assigned exposures.

The Pt(111) surface (thermodynamically the most stable face) exhibits a surface atom number density of $1.5 \times 10^{15}\,\mathrm{cm}^{-2}$. For a polycrystalline platinum surface this number is expected to be smaller and a reasonable approximation would be $1.25 \times 10^{15}\,\mathrm{cm}^{-2}$. As the prepared MIM cross junction had an area of $\approx 0.12\,\mathrm{cm}^2$ around 1.5×10^{14} Pt atoms participated in the surface dynamics. If each of these Pt atoms picked up or lost an electron a theoretical charge transfer of $Q \approx \pm 24\,\mu\mathrm{C}$ would have resulted. [108] Even higher charges could have resulted if the whole platinum film and not only the platinum of the MIM cross junction interacted with adsorbed species in adsorption and desorption processes. In the course of this work reversible charges of $\approx$ 1–10 nC (and therewith three orders of magnitude less than theoretically possible) due to desorption and adsorption processes were measured. Presumably, not all Pt surface atoms were involved and only fractions of charges were induced. Nevertheless, the used MIM devices enabled the detection of these process induced charges.

Despite the fact that the performed backside heating still resulted in temperature gradients on the MIM surface, the obtained TPD spectra were in excellent agreement with spectra from literature. Thus, the developed temperature measurement in combination with the developed localized heating method was not only applicable and reproducible but also accurate—and certainly suitable for nanodevices.

In the case of HCOOH TPD experiments an oxygen-free platinum surface was prepared by each initial HCOOH exposure. Pre-adsorbed oxygen was irretrievably consumed by the HCOOH decomposition reactions—and presumably was consumed within each initial formic acid TPD. The fact that the obtained TPD spectra were in good agreement with TPD spectra reported for clean Pt(111) surfaces supported this assumption as well. As condensed formic acid was expected to form an almost endless network of hydrogen-bonded formic acid molecules, similar device current charges to experiments with H_2O or D_2O could have resulted in the case of formation and decomposition of this network. However, the measured changes of the device current were different to the H_2O and D_2O experiments in sign and intensity. Thus, a different process in the course of formic acid desorption/decomposition was suggested.

As the observed device current changes in the case of HCOOH desorption/decomposition were positive, a non-adiabatic electron contribution was considered as possible. Such a non-adiabatic contribution to the device current increase could have resulted from the low temperature decomposition reaction according to:

$$2\,\mathrm{HCOO}_{\mathrm{M(a)}} \longrightarrow \mathrm{CO}_{2\mathrm{(g)}} + \mathrm{HCOOH}_{\mathrm{(a)}}\,. \tag{5.2}$$

Here, the formed carbon dioxide could leave the substrate with a significant amount of in-plane bending vibration (scissoring) as each CO_2 molecule needed to convert from the bent carbonyl configuration to a linear configuration (see figure 5.2). Analogous to observations in the course of the CO oxidation over platinum, the bent CO_2 could have either desorbed vibrational excited or dissipated the vibration energy to the substrate in order to equilibrate. In the second case, a rapid exchange of energy could have possibly induced hot charge carriers in the substrate. Nonetheless, adiabatic processes were more decisive here because the absolute values of the observed adsorption and desorption charges were of same size. Also, a tendency for saturation was visible for dosages above 4 L. Thus, non-adiabatic effects could have been a contribution but were not considered as the dominant source for the device

current changes.

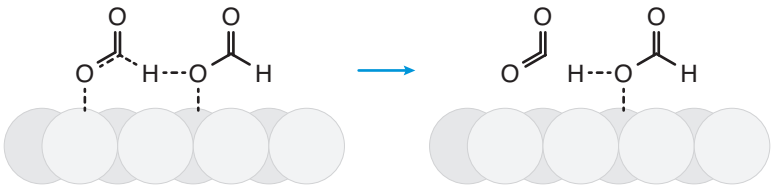

Figure 5.2: HCOOH decomposition reaction at low temperatures proposed according to reaction 5.2

One could argue that the presence (or absence) of oxygen on the platinum surface determined the sign of the detected charges. If pre-adsorbed oxygen was present, the adsorption caused positive charges and the desorption caused negative charges. This was observed for H_2O, D_2O, and CH_3OH. In the case of formic acid an oxygen-free platinum surface was prepared and the adsorption caused negative charges whereas the desorption caused positive charges. In the course of HCOOH adsorption electron density was transferred from the carboxylic acid toward the platinum and collected by the potentiostat as negative current. In return, electron density was transferred from the platinum toward the desorbing formic acid. Thus, pre-adsorbed oxygen acted as an electron donor to the adsorbate whereas the adsorbate itself acted as an electron donor to the platinum in case of an oxygen-free surface.

In addition, it should be considered that changes in the platinum work function could have contributed to the charging as well. Technically, adsorbate–substrate interactions like the discussed surface dynamics can change the work function of the platinum film. The deposition of electron acceptor species with electronegative character causes an electron transfer that creates a surface dipole and increases the work function of the substrate. In Turn, the work function decreases as a result of the deposition of electropositive species. [109] The magnitude of this processes depends on the amount of created surface dipoles. Essentially, these work function changes of a metal substrate (platinum, for instance) are composed of two contributions:

> a volume part, which is understood as the energy that is necessary to bring the electron with the highest energy in electronic equilibrium (the

Fermi energy) with an energy level within the metal which is equivalent to the vacuum level (this is a hypothetical electron at rest outside the metal in the vacuum chamber)

and a surface part, which is understood as the energy that is necessary to cross the platinum–vacuum interface.

The adsorption of oxygen or OH species modifies the surface part of the the work function. The adsorption of oxygen species on platinum was identified to increase the external work function W_{ext} by about 0.3 V. [110] The term external is used here in order to underline the fact that the top metal of the metal–insulator–metal structure has an internal work function as well. This is the energy that is necessary to transfer an electron from the Fermi level to the conduction band of the insulator on the opposite site of the top metal film. This energy does not directly depend on the external work function, but depends clearly on the bulk properties of the metal film. If the electron density n_e does not change in the course of an adsorption process the internal work function W_{int} remains constant (see figure 5.3).

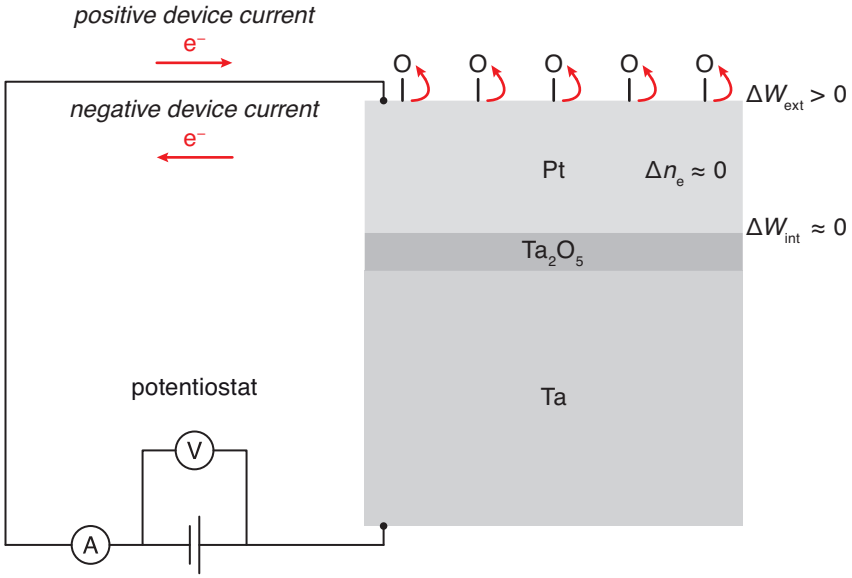

Figure 5.3: Adsorption of electronegative species (oxygen, for instance) on a thick ($d > 20$ nm) platinum top electrode of an MIM nanodiode

If the top platinum film is thin ($d < 10\,\mathrm{nm}$) the adsorption of an electronegative species can modify the electron density of the thin platinum film (see figure 5.4). This was experimentally found during the adsorption of oxonium ions on thin platinum films [111] and confirmed later [35]. For instance, due to the adsorption of electronegative species the electron density in the top platinum electrode decreases and therewith the Fermi level of the top electrode because $E_\mathrm{F} \propto (n_\mathrm{e})^{2/3}$. As a result, the device voltage changes and the potentiostat counterbalances this by supplying electrons to the platinum electrode.

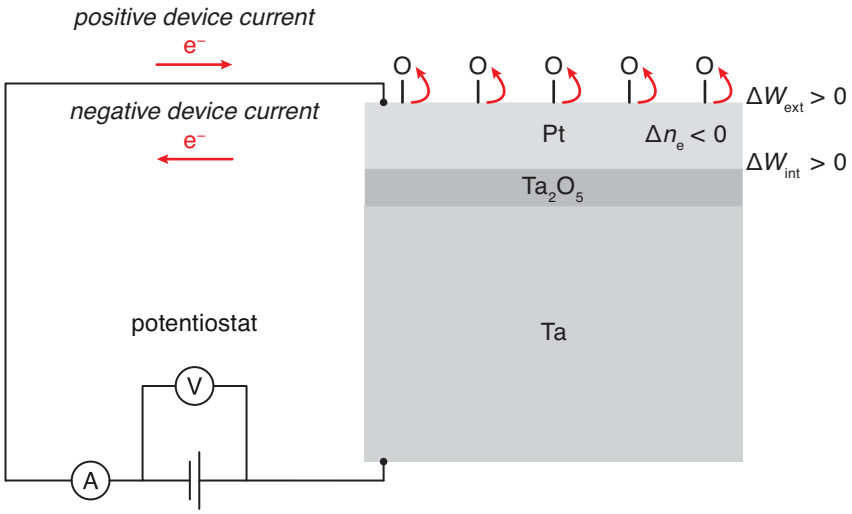

Figure 5.4: Adsorption of electronegative species (oxygen, for instance) on a thin ($d < 10\,\mathrm{nm}$) platinum top electrode of an MIM nanodiode

One should underline that the external work function is changed in both cases. Accordingly, work function changes due to sorption processes are more prominent if the surface/volume ratio of the substrate material is larger so that a large fraction of its electronic structure is affected. Thus, especially thin films (and thin film nanodevices) are sensitive to these processes.

As far as the surface dipole creation is reversible, the resulting work function changes are reversible as well. In order to determine the contribution of work function changes to the discussed charging, the same sorption experiments should be studied using devices with platinum films of different thicknesses. If the magnitude of the charging changes with film thickness, work

function changes should be considered.

5.1 Conclusion

The main conclusions of this research were:

A method of *in-situ* temperature measurement was developed, calibrated, and applied that allowed for the temperature measurement of a nanoscopic volume.

Various temperature programmed desorption experiments were reproducibly performed from MIM chemoelectronic nanodiodes.

For the first time, the device current of an MIM chemoelectronic nanodiode was monitored while performing temperature programmed desorption experiments.

Significant MIM device current responses to sorption processes of H_2O, D_2O, methanol, and formic acid were observed.

These MIM device current responses were identified as the result of reversible processes.

These reversible processes were identified as surface effects.

Possible non-adiabatic contributions to the detected MIM device currents were identified for the decomposition of formic acid on platinum but were considered as marginal—if present at all.

Atomic oxygen, pre-adsorbed on the platinum top electrode of the used MIM devices, was identified to influence the observed processes.

5.2 Outlook

Further research is required in order to confirm the conclusions. Future experimental designs should consider the influences on the ITO resistance in the

course of adsorption experiments and less susceptible ITO compositions (obtained by modifications in the preparation method) or alternative materials could be tested for improvements. In addition, an improved thermal stability of the devices would be desirable. Such devices could also be used to study surface-catalyzed reactions at temperatures above 600 K where the reaction rates are typically increased. Such devices could be cleaned more effectively as well and certain TPD experiments that demand for higher temperatures would become feasible.

5.3 Final remarks

For a given object of any substance at thermal equilibrium its temperature is an intensive property. This implies that the temperature is independent of the amount of substance or the size of the object. Nevertheless, if the size of the object is nanoscopic the temperature measurement itself can influence the thermal equilibrium. Non-invasive optical methods of temperature measurement are also not suitable if the object dimensions are smaller than the penetration depth of the measurement. Thus, it is not trivial to determine the temperature of a nanoscale object. The method of *in-situ* temperature measurement that was developed and applied in the course of this study allowed for the temperature measurement of nanodevices. It was observed that the temperature of the nanodevice was significantly different from the temperature of the surroundings—even in the immediate vicinity. In general, it should be considered that the temperature of nanoscale catalytic materials could be higher than expected and temperature (apart from the increased surface/volume ratio) is a reason for the increased catalytic properties of nanomaterials as well. One could note that nanoscopic temperature measurement is still an underestimated topic.

6 Appendices

6.1 Publications

Results of this thesis were published as:

> Jan Philipp Meyburg, Ievgen I. Nedrygailov, Eckart Hasselbrink, and Detlef Diesing
> Thermal desorption spectroscopy from the surfaces of metal–oxide-semiconductor nanostructures
> *Review of Scientific Instruments* 85, 104102 (2014)

Another publication about the *in-situ* temperature measurement is in preparation and should preferably be published in *ACS Applied Materials & Interfaces*. The effort in designing a new physical chemistry laboratory course for chemistry students was summarized and published in the *ASC Journal of Chemical Education* as:

> Jan Philipp Meyburg and Detlef Diesing
> Teaching the growth, ripening, and agglomeration of nanostructures in computer experiments
> *Journal of Chemical Education* 94, 1225–1231 (2017)

In the course of a DFG funded collaboration with Alexandr Alekhin, Alexey Melnikov, and Ilya Razdolski from the Fritz Haber Institute of the Max Planck Society in Berlin, Vladimir Roddatis from the University of Göttingen, and Uwe Bovensiepen from the Faculty of Physics in Duisburg three-layer monocrystalline sandwich structures were prepared by the author. The experience in preparation of three-layer metal–insulator–metal sandwich systems and the

results from the presented chemical experiments on those sandwich systems facilitated the preparation of the desired epitaxially grown three-layer magnet–non-magnet–magnet (MNM) systems. The prepared MNM samples were further investigated in Göttingen and fundamental experiments were performed in Berlin. Results from this collaboration were published as:

> Alexandr Alekhin, Ilya Razdolski, Nikita Ilin, Jan P. Meyburg, Detlef Diesing, Vladimir Roddatis, Ivan Rungger, Maria Stamenova, Stefano Sanvito, Uwe Bovensiepen, and Alexey Melnikov
> Femtosecond spin current pulses generated by the nonthermal spin-dependent Seebeck effect and interacting with ferromagnets in spin valves
> *Physical Review Letters* 119, 017202 (2017)

> Ilya Razdolski, Alexandr Alekhin, Nikita Ilin, Jan P. Meyburg, Vladimir Roddatis, Detlef Diesing, Uwe Bovensiepen, and Alexey Melnikov
> Nanoscale interface confinement of ultrafast spin transfer torque driving non-uniform spin dynamics
> *Nature Communications* 8, 15007 (2017)

> Alexey Melnikov, Ilya Razdolski, Alexandr Alekhin, Nikita Ilin, Jan Meyburg, Detlef Diesing, Vladimir Roddatis, Ivan Rungger, Maria Stamenova, Stefano Sanvito, and Uwe Bovensiepen
> Ultrafast spintronics roadmap: from femtosecond spin current pulses to terahertz non-uniform spin dynamics via nano-confined spin transfer torques
> *Proceedings of SPIE* 9931, 99311A (2016)

6.2 Presentations

Results of this thesis were presented by the author as:

Temperature dependence and lateral distribution of bias voltage driven charge transport through thin tantalum oxide films,
Spring Meeting of the German Physical Society, Dresden, 3/2017

Molecular dynamics monitored using chemoelectronic nanodiodes,
Dalian Institute of Chemical Physics, Dalian, 7/2016

In-situ temperature measurement using chemoelectronic nanodiodes,
Spring Meeting of the German Physical Society, Regensburg, 3/2015

Temperature programmed desorption from chemoelectronic nanodiodes,
Spring Meeting of the German Physical Society, Dresden, 4/2014

6.3 Used samples

Label	Type	Remarks
JPM 1.01–JPM 1.04	$Pt/Ag-Ta_2O_5-Ta$	Ag was deposited on the oxidized Ta and the MIM functionality was checked in order to avoid an unnecessary Pt consumption in advance.
JPM 2.01–JPM 2.04	$Pt-Ta_2O_5-Ta$	50 % yield: two samples were faultless.
JPM 3.01–JPM 3.04	$Pt-Ta_2O_5-Ta$	Perfect yield: all four samples were faultless.

6.4 Used Igor Pro procedure

```
Function peak_currents()
Wave I_317K,U_317K
Variable i,counter=0,ii=-1
Variable maximum_potential=190,minimum_potential=150
for(i=0;i<=numpnts(I_317K)-2;i+=1)
if(U_317K[i]>minimum_potential && U_317K[i+1]>U_317K[i])
counter+=1
endif
endfor
Make/o/N=(counter) peak_values
for(i=0;i<=numpnts(I_317K)-2;i+=1)
if(U_317K[i]>minimum_potential && U_317K[i+1]>U_317K[i])
ii+=1;
peak_values[ii]=I_317K[i]
endif
endfor

End
```

Bibliography

[1] K. W. Kolasinski. *Surface Science: Foundations of Catalysis and Nanoscience*. John Wiley and Sons, Chichester, 2012.

[2] A. F. Holleman, E. Wiberg, and N. Wiberg. *Lehrbuch der Anorganischen Chemie*. Walter de Gruyter, Berlin, 2007.

[3] E. Riedel. *Allgemeine und Anorganische Chemie*. Walter de Gruyter, Berlin, 2010.

[4] K. Christmann, G. Ertl, and T. Pignet. Adsorption of hydrogen on a Pt(111) surface. *Surface Science*, 54(2):365–392, 1976.

[5] G. Binnig, H. Rohrer, C. Gerber, and E. Weibel. Surface studies by scanning tunneling microscopy. *Physical Review Letters*, 49(1):57–61, 1982.

[6] D. M. Eigler and E. K. Schweizer. Positioning single atoms with a scanning tunnelling microscope. *Nature*, 344(6266):524–526, 1990.

[7] E. Hasselbrink. Capturing the complexities of molecule–surface interactions. *Science*, 326(5954):809–810, 2009.

[8] E. Hasselbrink. Non-adiabaticity in surface chemical reactions. *Surface Science*, 603(10–12):1564–1570, 2009.

[9] M. Born and R. Oppenheimer. Zur Quantentheorie der Molekeln. *Annalen der Physik*, 84(20):457–484, 1927.

[10] T. Yonehara, K. Hanasaki, and K. Takatsuka. Fundamental approaches to nonadiabaticity: toward a chemical theory beyond the Born–Oppenheimer paradigm. *Chemical Reviews*, 112(1):499–542, 2012.

[11] H. Haken and H. C. Wolf. *Molekülphysik und Quantenchemie: Einführung in die experimentellen und theoretischen Grundlagen*. Springer, Berlin, 2006.

[12] J. C. A. Boeyens. *Chemistry from First Principles*. Springer, Berlin, 2008.

[13] A. W. Jasper, C. Zhu, S. Nangia, and D. G. Truhlar. Introductory lecture: nonadiabatic effects in chemical dynamics. *Faraday Discussions*, 127:1–22, 2004.

[14] A. W. Jasper, S. Nangia, C. Zhu, and D. G. Truhlar. Non-Born–Oppenheimer molecular dynamics. *Accounts of Chemical Research*, 39(2):101–108, 2006.

[15] E. G. Lewars. *Computational Chemistry: Introduction to the Theory and Applications of Molecular and Quantum Mechanics*. Springer, Berlin, 2016.

[16] T. Greber. Charge-transfer induced particle emission in gas surface reactions. *Surface Science Reports*, 28(1–2):1–64, 1997.

[17] H. Nienhaus. Electronic excitations by chemical reactions on metal surfaces. *Surface Science Reports*, 45(1–2):1–78, 2002.

[18] J. J. Thomson. On the emission of negative corpuscles by the alkali metals. *Philosophical Magazine Series 6*, 10(59):584–590, 1905.

[19] E. Hasselbrink. How non-adiabatic are surface dynamical processes? *Current Opinion in Solid State and Materials Science*, 10(3–4):192–204, 2006.

[20] X. Ji, A. Zuppero, J. M. Gidwani, and G. A. Somorjai. The catalytic nanodiode: gas phase catalytic reaction generated electron flow using nanoscale platinum titanium oxide Schottky diodes. *Nano Letters*, 5(4):753–756, 2005.

[21] B. Gergen, H. Nienhaus, W. H. Weinberg, and E. W. McFarland. Chemically induced electronic excitations at metal surfaces. *Science*, 294(5551):2521–2523, 2001.

[22] B. Mildner, E. Hasselbrink, and D. Diesing. Electronic excitations induced by surface reactions of H and D on gold. *Chemical Physics Letters*, 432(1–3):133–138, 2006.

[23] B. Schindler, D. Diesing, and E. Hasselbrink. Electronically nonadiabatic processes in the interaction of H with a Au surface revealed using MIM junctions: the temperature dependence. *The Journal of Physical Chemistry C*, 117(12):6337–6345, 2013.

[24] D. Diesing, D. A. Kovacs, K. Stella, and C. Heuser. Characterization of atom and ion-induced "internal" electron emission by thin film tunnel junctions. *Nuclear Instruments and Methods in Physics Research Section B: Beam Interactions with Materials and Atoms*, 269(11):1185–1189, 2011.

[25] D. A. Kovacs, J. Winter, S. Meyer, A. Wucher, and D. Diesing. Photo and particle induced transport of excited carriers in thin film tunnel junctions. *Nuclear Instruments and Methods in Physics Research Section B: Beam Interactions with Materials and Atoms*, 76(23):235408, 2007.

[26] H. Nienhaus, B. Gergen, W. H. Weinberg, and E. W. McFarland. Detection of chemically induced hot charge carriers with ultra-thin metal film schottky contacts. *Surface Science*, 514(1–3):172–181, 2002.

[27] A. Amirav, W. R. Lambert, M. J. Cardillo, P. L. Trevor, N. Luke, and E. E. Haller. Electron-hole pair creation at a Ge(100) surface by ground-state neutral Xe atoms. *Journal of Applied Physics*, 59(6):2213–2215, 1986.

[28] H. Nienhaus, H. Bergh, B. Gergen, A. Majumdar, W. H. Weinberg, and E. W. McFarland. Electron-hole pair creation at Ag and Cu surfaces by adsorption of atomic hydrogen and deuterium. *Physical Review Letters*, 82(2):446–449, 1999.

[29] T. J. Seebeck. Über die magnetische Polarisation der Metalle und Erze durch Temperatur-Differenz. *Annalen der Physik*, 82(2):133–160, 1826.

[30] H. Ibach and H. Lüth. *Solid-State Physics: An Introduction to Principles of Materials Science*. Springer, Berlin, 2009.

[31] H. J. Goldsmid. *Introduction to Thermoelectricity*. Springer, Berlin, 2016.

[32] J. R. Creighton and M. E. Coltrin. Origin of reaction-induced current in Pt/GaN catalytic nanodiodes. *The Journal of Physical Chemistry C*, 116(1):1139–1144, 2012.

[33] X. Ji, A. Zuppero, J. M. Gidwani, and G. A. Somorjai. Electron flow generated by gas phase exothermic catalytic reactions using a platinum–gallium nitride nanodiode. *Journal of the American Chemical Society*, 127(16):5792–5793, 2005.

[34] X. Ji and G. A. Somorjai. Continuous hot electron generation in Pt/TiO_2, Pd/TiO_2, and Pt/GaN catalytic nanodiodes from oxidation of carbon monoxide. *The Journal of Physical Chemistry B*, 109(47):22530–22535, 2005.

[35] B. Schindler, D. Diesing, and E. Hasselbrink. Electronic excitations in the course of the reaction of H with coinage and noble metal surfaces: a comparison. *Zeitschrift für Physikalische Chemie*, 227(9–11):1381–1395, 2013.

[36] D. Diesing and E. Hasselbrink. Chemical energy dissipation at surfaces under UHV and high pressure conditions studied using metal–insulator–metal and similar devices. *Chemical Society Reviews*, 45(13):3747–3755, 2016.

[37] B. Schindler, D. Diesing, and E. Hasselbrink. Electronic excitations induced by hydrogen surface chemical reactions on gold. *The Journal of Chemical Physics*, 134(3):034705, 2011.

[38] P. A. Redhead. The birth of electronics: thermionic emission and vacuum. *Journal of Vacuum Science & Technology A: Vacuum, Surfaces, and Films*, 16(3):1394–1401, 1998.

[39] E. L. Murphy and R. H. Good, Jr. Thermionic emission, field emission, and the transition region. *Physical Review*, 102(6):1464–1473, 1956.

[40] P. Thissen, B. Schindler, Diesing. D, and E. Hasselbrink. Thermionic emission, field emission, and the transition region. *New Journal of Physics*, 12(11):113014, 2010.

[41] K. Stella, D. A. Kovacs, D. Diesing, W. Brezna, and J. Smoliner. Charge transport through thin amorphous titanium and tantalum oxide layers. *Journal of The Electrochemical Society*, 158(5):P65–P74, 2011.

[42] T. Michely and J. Krug. *Islands, Mounds and Atoms: Patterns and Processes in Crystal Growth far from Equilibrium*. Springer, Berlin, 2004.

[43] G. Antczak and G. Ehrlich. *Surface Diffusion: Metals, Metal Atoms, and Clusters*. Cambridge University Press, Cambridge, 2010.

[44] R. Gomer. Diffusion of adsorbates on metal surfaces. *Reports on Progress in Physics*, 53(7):917–1002, 1990.

[45] J. P. Meyburg and D. Diesing. Teaching the growth, ripening, and agglomeration of nanostructures in computer experiments. *Journal of Chemical Education*, 94(9):1225–1231, 2017.

[46] J. K. Nørskov, A. Houmøller, P. K. Johansson, and B. I. Lundqvist. Adsorption and dissociation of H_2 on Mg surfaces. *Physical Review Letters*, 46(4):257–260, 1981.

[47] W. D. Mieher and W. Ho. Bimolecular surface photochemistry: mechanisms of CO oxidation on Pt(111) at 85 K. *The Journal of Chemical Physics*, 99(11):257–260, 1993.

[48] B. C. Stipe, M. A. Rezaei, and W. Ho. Atomistic studies of O_2 dissociation on Pt(111) induced by photons, electrons, and by heating. *The Journal of Chemical Physics*, 107(16):6443–6447, 1997.

[49] C. T. Campbell, G. Ertl, H. Kuipers, and J. Segner. A molecular beam study of the adsorption and desorption of oxygen from a Pt(111) surface. *Surface Science*, 107(1):220–236, 1981.

[50] J. L. Gland, B. A. Sexton, and G. B. Fisher. Oxygen interactions with the Pt(111) surface. *Surface Science*, 95(2–3):587–602, 1980.

[51] A. Groß. Ab initio molecular dynamics simulations of the O/Pt(111) interaction. *Catalysis Today*, 260:60–65, 2016.

[52] B. A. Sexton. Vibrational spectra of water chemisorbed on platinum (111). *Surface Science*, 94(2–3):435–445, 1980.

[53] A. Hodgson and S. Haq. Water adsorption and the wetting of metal surfaces. *Surface Science Reports*, 64(9):381–451, 2009.

[54] H. Ibach and S. Lehwald. The bonding of water molecules to platinum surfaces. *Surface Science*, 91(1):187–197, 1980.

[55] A. Shavorskiy, M. J. Gladys, and G. Held. Chemical composition and reactivity of water on hexagonal Pt-group metal surfaces. *Physical Chemistry Chemical Physics*, 10(40):6150–6159, 2008.

[56] T. Schiros, L.-Å. Näslund, K. Andersson, J. Gyllenpalm, G. S. Karlberg, M. Odelius, H. Ogasawara, L. G. M. Pettersson, and A. Nilsson. Structure and bonding of the water–hydroxyl mixed phase on Pt(111). *The Journal of Physical Chemistry C*, 111(41):15003–15012, 2007.

[57] J. R. Creighton and J. M. White. The decomposition of H_2O on oxygen-covered Pt(111): thermal and vibrational excitation effects. *The Journal of Physical Chemistry C*, 136(2):449–462, 1984.

[58] M. J. T. C. van der Niet, A. den Dunnen, L. B. F. Juurlink, and M. T. M. Koper. A detailed TPD study of H_2O and pre-adsorbed O on the stepped Pt(553) surface. *Physical Chemistry Chemical Physics*, 13(4):1629–1638, 2011.

[59] M. Wolf, S. Nettesheim, J. M. White, E. Hasselbrink, and G. Ertl. Ultraviolet-laser induced dissociation and desorption of water adsorbed on Pd(111). *The Journal of Chemical Physics*, 92(2):1509–1510, 1990.

[60] X. Y. Zhu, J. M. White, M. Wolf, E. Hasselbrink, and G. Ertl. Photochemical pathways of water on palladium (111) at 6.4 eV. *The Journal of Physical Chemistry*, 95(21):8393–8402, 1991.

[61] L.-Å. Näslund. Hydrogenation of O and OH on Pt(111): a comparison between the reaction rates of the first and the second hydrogen addition steps. *The Journal of Chemical Physics*, 140(10):104701–1638, 2014.

[62] M. Morgenstern, T. Michely, and G. Comsa. Anisotropy in the adsorption of H_2O at low coordination sites on Pt(111). *Physical Review Letters*, 77(4):703–706, 1996.

[63] R. Duś, E. Nowicka, and R. Nowakowski. The response of work function of thin metal films to interaction with hydrogen. *Acta Physica Polonica A*, 114(S):29–47, 2008.

[64] D. D. Eley and E. K. Rideal. Parahydrogen conversion on tungsten. *Nature*, 146(3699):401–402, 1940.

[65] G. Ehrlich. Kinetic and experimental basis of flash desorption. *Journal of Applied Physics*, 32(1):4–15, 1961.

[66] P. A. Redhead. Thermal desorption of gases. *Vacuum*, 12(4):203–211, 1962.

[67] D. A. King. Thermal desorption from metal surfaces: a review. *Surface Science*, 47(1):384–402, 1975.

[68] G. Comsa and R. David. Dynamical parameters of desorbing molecules. *Surface Science Reports*, 5(4):145–198, 1985.

[69] J. P. Meyburg. Temperature programmed desorption from chemoelectronic nanodiodes. Master's thesis, University of Duisburg–Essen, 2013.

[70] B. D. B. Aaronson, C.-H. Chen, H. Li, M. T. M. Koper, S. C. S. Lai, and P. R. Unwin. Pseudo-single-crystal electrochemistry on polycrystalline

electrodes: visualizing activity at grains and grain boundaries on platinum for the Fe^{2+}/Fe^{3+} redox reaction. *Journal of the American Chemical Society*, 135(10):3873–3880, 2013.

[71] G. B. Fisher and J. L. Gland. The interaction of water with the Pt(111) surface. *Surface Science*, 94(2–3):446–455, 1980.

[72] J. L. Daschbach, B. M. Peden, R. S. Smith, and B. D. Kaya. Adsorption, desorption, and clustering of H_2O on Pt(111). *The Journal of Chemical Physics*, 120(3):1516–1523, 2004.

[73] M. J. T. C. van der Niet, O. T. Berg, L. B. F. Juurlink, and M. T. M. Koper. The interaction between H_2O and preadsorbed O on the stepped Pt(533) surface. *The Journal of Physical Chemistry C*, 114(44):1629–1638, 2010.

[74] M. J. T. C. van der Niet, A. den Dunnen, L. B. F. Juurlink, and M. T. M. Koper. The influence of step geometry on the desorption characteristics of O_2, D_2, and H_2O from stepped Pt surfaces. *The Journal of Chemical Physics*, 132(17):174705, 2010.

[75] G. B. Fisher and B. A. Sexton. Identification of an adsorbed hydroxyl species on the Pt(111) surface. *Physical Review Letters*, 44(10):683–686, 1980.

[76] C. C. Clay, S. Haq, and A. Hodgson. Hydrogen bonding in mixed OH + H_2O overlayers on Pt(111). *Physical Review Letters*, 92(4):046102, 2004.

[77] M. L. Grecea, E. H. G. Backus, B. B. Riedmüller, A. Eichler, A. W. Kleyn, and M. Bonn. The interaction of water with the Pt(533) surface. *The Journal of Physical Chemistry B*, 108(33):12575–12582, 2004.

[78] A. den Dunnen, M. J. T. C. van der Niet, M. T. M. Koper, and L. B. F. Juurlink. Interaction between H_2O and preadsorbed D on the stepped Pt(553) surface. *The Journal of Physical Chemistry C*, 116(35):18706–18712, 2012.

[79] C. Panja, N. Saliba, and B. E. Koel. Adsorption of methanol, ethanol and water on well-characterized Pt−Sn surface alloys. *Surface Science*, 395(2):248–259, 1998.

[80] A. F. Lee, D. E. Gawthrope, N. J. Hart, and K. Wilson. A fast XPS study of the surface chemistry of ethanol over Pt(111). *Surface Science*, 548(1):200–208, 2004.

[81] J. L. Davis and M. A. Barteau. Decarbonylation and decomposition pathways of alcohols on Pd(111). *Surface Science*, 187(2–3):387–406, 1987.

[82] G. B. Fisher. The electronic structure of two forms of molecular ammonia adsorbed on Pt(111). *Chemical Physics Letters*, 79(3):452–458, 1981.

[83] T. Ohtani, J. Kubota, Kondo J. N. Wada, A., K. Domen, and C. Hirose. IRAS and TPD study of adsorbed formic acid on Pt(110)-(1 $\times$ 2) surface. *Surface Science*, 368(1–3):270–274, 1996.

[84] M. R. Columbia, A. M. Crabtree, and P. A. Thiel. The temperature and coverage dependences of adsorbed formic acid and its conversion to formate on platinum(111). *Journal of the American Chemical Society*, 114(4):1231–1237, 1992.

[85] N. R. Avery. Adsorption of formic acid on clean and oxygen covered Pt(111). *Applications of Surface Science*, 11–12:774–783, 1982.

[86] M. R. Columbia, A. M. Crabtree, and P. A. Thiel. Chemical reactions between atomic oxygen and formic acid on Pt(111). *Journal of Electroanalytical Chemistry*, 351(1–2):207–226, 1993.

[87] T. L. Silbaugh, E. M. Karp, and C. T. Campbell. Energetics of methanol and formic acid oxidation on Pt(111): mechanistic insights from adsorption calorimetry. *Surface Science*, 650:140–143, 2016.

[88] P. A. Thiel and T. E. Madey. The interaction of water with solid surfaces: fundamental aspects. *Surface Science Reports*, 7(6–8):211–385, 1987.

[89] K. Stella, D. Bürstel, S. Franzka, O. Posth, and D. Diesing. Preparation and properties of thin amorphous tantalum films formed by small e-beam evaporators. *Journal of Physics D: Applied Physics*, 42(13):135417, 2009.

[90] K. Stella, S. Franzka, D. Bürstel, D. Diesing, D. Mayer, and V. Roddatis. Electrochemical oxidation as vertical structuring tool for ultrathin ($d <$ 10 nm) metal films. *IEEE Journal of Nanotechnology*, 3(5):P143–P148, 2014.

[91] A. W. Hassel and M. M. Lohrengel. The scanning droplet cell and its application to structured nanometer oxide films on aluminium. *Electrochimica Acta*, 42(20–22):3327–3333, 1997.

[92] W. Schmickler and E. Santos. *Interfacial Electrochemistry*. Springer, Berlin, 2010.

[93] T. A. Delchar. *Vacuum Physics and Techniques*. Chapman and Hall, London, 1993.

[94] P. A. Redhead, J. P. Hobson, and E. V. Kornelsen. *The Physical Basis of Ultrahigh Vacuum*. Chapman and Hall, London, 1968.

[95] S. Dushman. *Scientific Foundations of Vacuum Technique*. John Wiley and Sons, New York, 1962.

[96] J. P. Meyburg, I. I. Nedrygailov, E. Hasselbrink, and D. Diesing. Temperature programmed desorption from the surface of metal–oxide–semiconductor nanostructures. *Review of Scientific Instruments*, 85(104102):1–5, 2014.

[97] L. Michalski, K. Eckersdorf, and J. McGhee. *Temperature Measurement*. John Wiley and Sons, Chichester, 2001.

[98] N. P. Moiseeva. Individual calibration of resistance thermometers for measuring temperature difference. *Measurement Techniques*, 53(9):1042–1046, 2010.

[99] H. Preston-Thomas. The international temperature scale of 1990. *Metrologia*, 27(1):3–10, 1990.

[100] M. S. van Dusen. Platinum–resistance thermometry at low temperatures. *Journal of the American Chemical Society*, 47(2):326–332, 1925.

[101] Comité International des Poids et Mesures. The international practical temperature scale of 1968. *Metrologia*, 5(2):35–44, 1968.

[102] I. I. Nedrygailov, I. I. Nedrygailov, E. Hasselbrink, D. Diesing, S. K. Dasari, M. A. Hashemian, and E. G. Karpov. Noninvasive measurement and control of the temperature of Pt nanofilms on Si supports. *Journal of Vacuum Science & Technology A: Vacuum, Surfaces, and Films*, 30(3):030601, 2012.

[103] J. R. Trail, D. M. Bird, M. Persson, and S. Holloway. Electron–hole pair creation by atoms incident on a metal surface. *Journal of Chemical Physics*, 119(8):4539–4549, 2003.

[104] M. Scheele, I. I. Nedrygailov, E. Hasselbrink, and D. Diesing. Energy transfer in argon atom–surface interactions studied by $Pt-SiO_2-Si$ thin film chemoelectronic devices. *Vacuum*, 111:137–141, 2015.

[105] K. Christmann. Some general aspects of hydrogen chemisorption on metal surfaces. *Progress in Surface Science*, 48(1):15–26, 1995.

[106] D.-G. Kim, S. Lee, G.-H. Lee, and S.-C. Kwon. Effects of hydrogen gas on properties of tin-doped indium oxide films deposited by radio frequency magnetron sputtering method. *Thin Solid Films*, 515(17):6949–6952, 2007.

[107] K. Okada, S. Kohiki, S. Luo, D. Sekiba, S. Ishii, M. Mitome, A. Kohno, T. Tajiri, and F. Shoji. Correlation between resistivity and oxygen vacancy of hydrogen-doped indium tin oxide thin films. *Thin Solid Films*, 519(11):3557–3561, 2011.

[108] N. M. Marković, T. J. Schmidt, B. N. Grgur, H. A. Gasteiger, R. J. Behm, and P. N. Ross. Effect of temperature on surface processes at the Pt(111)-

liquid interface: hydrogen adsorption, oxide formation, and CO oxidation. *The Journal of Physical Chemistry B*, 103(40):8568–8577, 1999.

[109] A. Kahn. Fermi level, work function and vacuum level. *Materials Horizons*, 3(1):7–10, 2016.

[110] G. N. Derry and P. N. Ross. A work function change study of oxygen adsorption on Pt(111) and Pt(100). *The Journal of Chemical Physics*, 82(6):2772–2778, 1985.

[111] D. Bürstel and D. Diesing. Electrochemically induced charge transfer in platinum–silicon heterosystems. *physica status solidi (a)*, 209(5):805–812, 2012.